Measuring the Absolute Concentration of Particles in Suspension using High Frequency B-mode Ultrasound Imaging

by

John Haeseon Lee

B.S., Electrical and Computer Engineering, Cornell University (2006)
S.M., Electrical Engineering and Computer Science, MIT (2011)

Submitted to the Department of Electrical Engineering and Computer Science
in Partial Fulfillment of the Requirements for the Degree of

Doctor of Philosophy

at the

MASSACHUSETTS INSTITUTE OF TECHNOLOGY

June, 2016

Author_____
Department of Electrical Engineering and Computer Science
May 20, 2016

Certified by_____
Duane S. Boning
Professor of Electrical Engineering and Computer Science
Thesis Supervisor

Certified by_____
Brian W. Anthony
Principle Research Scientist, Department of Mechanical Engineering and
Institute for Medical Engineering and Science
Thesis Supervisor

Accepted by_____
Leslie Kolodziejski
Chair, Department Committee on Graduate Theses

THIS PAGE IS INTENTIONALLY LEFT BLANK

Measuring the Absolute Concentration of Particles in Suspension using
High Frequency B-mode Ultrasound Imaging

by

John Haeseon Lee

Submitted to the Department of Electrical Engineering and Computer Science on
May 20, 2016 in Partial Fulfillment of the Requirements for
the Degree of Doctor of Philosophy in
Electrical Engineering and Computer Science

ABSTRACT

Concentration measurement of particles in suspension is an important procedure performed in biological and clinical laboratories. Existing methods based on instruments such as hemocytometers, coulter counters, and flow cytometers are often laborious, destructive, and incapable of *in vivo* measurements. An ultrasound-based method has several unique advantages. It can be nondestructive and noninvasive, which allows a much larger portion of the sample to be analyzed, improving the accuracy and decreasing required sample volume. Also, ultrasound methods have the potential for *in vivo* measurement in the clinical setting, where cell concentration in liquids such as cerebrospinal fluid can be measured noninvasively without requiring a lumbar puncture. In this work, a new method is presented that estimates absolute particle concentration from high frequency B-mode ultrasound images. The method is based on the detection and characterization of the echoes from individual particles to estimate the effective slice thickness of the image. Prior characterization of the sample is not required because the estimation relies only on parameters that are measured directly from the image. The particle type differential is also performed by using the backscatter coefficient. The method is demonstrated by measuring microsphere suspensions as well as human T cell suspensions using a mechanically scanned single element transducer imaging system and a VisualSonics Vevo 2100. The proposed method has a wide range of potential clinical applications including noninvasive measurement of cell concentration in biological fluids.

Thesis Supervisor: Duane S. Boning
Title: Professor of Electrical Engineering and Computer Science

Thesis Supervisor: Brian W. Anthony
Title: Principle Research Scientist, Department of Mechanical Engineering and Institute for Medical Engineering and Science

THIS PAGE IS INTENTIONALLY LEFT BLANK

Acknowledgments

First of all, I would like to thank my advisor Prof. Duane Boning for his guidance and support during my time here at MIT. Over the last seven years, I was able to grow into not only a better engineer and a researcher, but also a more passionate and mature human being. I am especially grateful that he allowed me and supported me through my unique journey of finding life's passion. My life would have been very different had I not met Prof. Boning. I would not want it any other way.

I would also like to thank my advisor Dr. Brian Anthony for introducing me to the amazing field of ultrasound. Dr. Anthony not only took me in without hesitation when I had no experience in medical device or medical imaging, but also allowed me and encouraged me to explore and find my interest. Working on ultrasound is what ultimately led me to find my passion in medicine and pursue a career in it. I owe a huge part of that to Dr. Anthony.

I had the fortune of having two advisors who put their students' interest and success before anything else. They truly have been the best advisors one could ask for. It is my sincere hope that I get to know them further even after I leave MIT.

I would like to thank my committee member, Prof. Elfar Adalsteinsson for his advice during this work. I was fortunate that I was able to work with him on various fronts and get valuable advice from him on different aspects of this work.

I would like to thank all my colleagues and friends in the Statistical Metrology Group and the Device Realization Group for being a part of my life and allowing me to be part of their lives at MIT. I am grateful not only for all the discussion we had over our work and research, but also for the conversation we had about our lives and about successes and struggles that we faced at that

moment. The countless hours we spent in our labs and the comradery we had as graduate students made our relationships that much more special. I cherish our relationship as labmates, colleagues, and most importantly, as friends, and I hope for it to continue outside of MIT.

I would like to thank my all my colleagues and friends I met over the years in Boston. I will not attempt to name them all for fear of leaving some out, but each person I met here during the last seven years, working or playing, has shaped me to become who I am today.

I would like to thank my dad and my mom, Sukhoon Lee and Youngsuk Lee, and my sister Hane Lee, for their unconditional love and support that taught me to become courageous and fearless in pursuit of my dream. Thank you for loving me the way you did. Thank you for teaching me to seek the truth and pursue true happiness in life and not settle for anything less than that. I am who I am because of you.

Last but not least, I would like to thank my wife, Youbean Oak, whom I love more strongly and deeply every day. Thank you for being my best friend, my counselor, and my biggest supporter. I am grateful that we've shared so much of our lives together already that we don't have to explain but we just know. Thank you for being there through all my ups and downs. Thank you for having me by your side through yours. Thank you for having my back no matter what. Thank you for your thorough reading of this manuscript. I am no longer capable of writing anything without you reviewing it. I love you.

The last seven years at MIT as a graduate student has truly been a roller coaster, sometimes a bit too more exciting than what I felt I could handle. The ride is near its end, but it seems more surreal than real. I will always cherish all of its ups and downs, and the twist and turns. It was a good ride.

Table of Contents

Acknowledgments 5
Table of Contents 7
List of Figures 9
List of Tables 13
1. Introduction 15
1.1 Existing Particle Concentration Measurement Methods 15
1.2 Quantitative Ultrasound 18
1.3 The Proposed Method 21
1.4 *In Vivo* Clinical Application 23
1.5 Organization of Thesis 28
2. Method Description 29
2.1 Overview 29
2.2 Particle Detection 34
2.3 Effective Slice Thickness Calculation 39
2.4 Effective Slice Thickness Calculation – Generalization 42
2.5 Algorithm Implementation 43
2.6 Estimation of Measurement Uncertainty 47
2.7 Summary 49
3. Experimental Work 53
3.1 Imaging systems 53
3.2 Samples 57
3.3 Overview of the Experiments 59
3.4 Reference Measurement 59
3.5 Statistical Analysis 60
4. Results 63
4.1 Experiments 1 and 2 63
4.1.1 Experiment 1 63
4.1.2 Experiment 2 68
4.2 Experiment 3 and 4 73
4.2.1 Experiment 3: 15 μm PS microspheres 73
4.2.2 Experiment 4: 10 μm silica microspheres 78
4.3 Experiment 5 83

4.4 Experiment 6 87
5. Discussion 93
5.1 Image Volume Dependencies 93
5.2 Maximum Measurable Concentration 96
5.3 Tradeoff between Accuracy and Number of Detections 101
6. Contributions and Future Work 105
6.1 Contributions 105
6.2 Particle Detection Algorithm 106
6.3 Transducer Model Based Estimation 107
6.4 Non-spherical Particles 108
6.5 Variability in Cell Size and Shape 108
6.6 Library of BSCs 109
6.7 Application: Clinical Study for Neonatal Meningitis 109
6.8 Application: *In vitro* Cell Analysis 111
6.9 Application: Transducer Characterization 112
Bibliography 115

List of Figures

FIGURE 1-1. (A) IMPROVED NEUBAUER HEMOCYTOMETER. (B) GRID FOR IMPROVED NEUBAUER HEMOCYTOMETER (IMAGE SOURCE: HTTP://WWW.MARIENFELD-SUPERIOR.COM). (C) COULTER COUNTER, BECKMAN COULTER Z2 (IMAGE SOURCE: WWW.BCKMANCOULTER.COM) (D) FLOW CYTOMETER BD FACSVERSE (IMAGE SOURCE: WWW.BDBIOSCIENCE.COM).....17

FIGURE 1-2. A COMPARISON BETWEEN NORMAL AND INFECTED CSF [39]. (A) NORMAL CSF SHOULD BE CLEAR AND WATER-LIKE IN APPEARANCE. (B) INFECTED CSF CAN BECOME YELLOW AND TURBID DUE TO INCREASED CELLULARITY AND PROTEIN.....24

FIGURE 1-3. ULTRASOUND IMAGES FROM [29] SHOWING DIFFERENT CONCENTRATION OF AML CELL SOLUTIONS (A) 0.0025%, (B) 0.05%, (C) 0.1% AND (D) 0.8%. WHEN CONCENTRATION IS LOW, THE ECHOES FROM INDIVIDUAL CELLS CAN BE CLEARLY DISTINGUISHED IN THE IMAGE. HOWEVER, WHEN THE CONCENTRATION IS HIGH, INDIVIDUAL ECHOES CAN NO LONGER BE DISTINGUISHED. THIS OCCURS DUE TO HAVING MORE THAN ONE CELL IN THE RESOLUTION CELL OF THE BEAM.....27

FIGURE 2-1. COORDINATE SYSTEM USED IN THIS WORK. IT IS ASSUMED THAT THE TRANSDUCER IS AT THE TOP OF THE IMAGE AND THE DIRECTION OF THE TRANSMITTED ULTRASOUND BEAM IS DOWNWARD. THE AXIAL DIRECTION (Z-AXIS) IS ALONG THE DEPTH OF THE IMAGE. THE LATERAL DIRECTION (X-AXIS) IS ALONG THE WIDTH OF THE IMAGE. THE ELEVATIONAL DIRECTION (Y-AXIS) IS PERPENDICULAR TO THE IMAGE PLANE (OUT-OF-PLANE).....30

FIGURE 2-2. B-MODE IMAGES OF 15 MM PS MICROSPHERES SUSPENDED IN DISTILLED WATER ACQUIRED WITH MECHANICALLY SCANNED SINGLE ELEMENT TRANSDUCER. FOUR CONCENTRATIONS ARE SHOWN: (A) 0.9 PARTICLES/ML, (B) 1.7 PARTICLES/ML, (C) 3.4 PARTICLES/ML, AND (D) 6.9 PARTICLES/ML. INDIVIDUAL PARTICLES CAN BE DISTINGUISHED IN THE IMAGES BECAUSE THE PARTICLE CONCENTRATION IS LOW. 31

FIGURE 2-3. DESCRIPTION OF EFFECTIVE BEAM WIDTH. (A) CONVENTIONAL -6 DB BEAM WIDTH DEFINED IN REFERENCE TO THE PEAK INTENSITY OF THE BEAM. (B) EFFECTIVE BEAM WIDTH WHEN THE MAXIMUM ECHO INTENSITY IS 10 DB ABOVE THE DETECTION THRESHOLD, AND (C) 2 DB ABOVE THE DETECTION THRESHOLD. 32

FIGURE 2-4. (A) A B-MODE IMAGE OF 15 MM PS MICROSPHERE SUSPENSION. THE DETECTED PARTICLES ARE MARKED BY RED CIRCLES. (B) THE CORRESPONDING 2D RF DATA FOR THE ECHO MARKED BY THE YELLOW CIRCLE. (C) 2D GAUSSIAN FITTING OF THE CORRESPONDING ECHO TO EXTRACT ITS AMPLITUDE, POSITION, AND LATERAL STANDARD DEVIATION. (D) NORMALIZED BSC FOR THE ECHO COMPARED TO THE FARAN MODEL FOR A 15 MM DIAMETER PS MICROSPHERE.....36

FIGURE 2-5. RESULTS FROM RUNNING THE PARTICLE DETECTION ALGORITHM ON THE ENTIRE SET OF FRAMES. (A) ECHO AMPLITUDES VS. LATERAL POSITIONS. (B) ECHO AMPLITUDES VS. AXIAL POSITIONS. (C) ECHO LATERAL STANDARD DEVIATION VS. AXIAL POSITIONS. (D) HISTOGRAM OF THE PEAK FREQUENCY IN BSC. 38

FIGURE 2-6. DIAGRAM DESCRIBING THE PRINCIPLE BEHIND THE PROPOSED METHOD. (A) POSITION OF THE TWO IDEAL SCATTERERS A AND B WHO HAVE AN EQUAL AXIAL POSITIONS. (B) RESULTING IDEALIZED B-MODE IMAGE FROM THE TWO SCATTERERS IN (A). A PRODUCES A MAXIMUM ECHO AND B PRODUCES A MINIMUM ECHO. (C) THE CROSS-SECTION OF THE B-MODE IMAGE AT THE POSITION MARKED BY THE RED DOTTED LINE. (D) THE POSSIBLE ELEVATIONAL POSITIONS OF A AND B DEDUCED FROM THE AMPLITUDE OF THEIR ECHOES. 40

FIGURE 2-7. RESULTS FROM THE PARTICLE DETECTION SLICED ALONG THE AXIAL DIRECTION: (A) ECHO AMPLITUDES VS. AXIAL POSITIONS AND (B) ECHO LATERAL STANDARD DEVIATION VS. AXIAL POSITIONS. CALCULATED PARAMETERS: (C) NUMBER OF DETECTED ECHOES PER FRAME VS. AXIAL SLICES, (D) EFFECTIVE SLICE THICKNESS VS. AXIAL SLICES, AND (E) SLICE CONCENTRATION VS. AXIAL SLICES. THE BLACK DOTTED LINES IN THE PLOTS (C) – (E) REPRESENT THE ESTIMATED MEASUREMENT UNCERTAINTY. 46

FIGURE 2-8. SUMMARY OF THE PROPOSED METHOD. THE SAMPLE IS IMAGED WITH AN IMAGING SYSTEM. THE PARTICLE DETECTION ALGORITHM IS RUN ON THE DATA FROM THE MEASUREMENT, WHICH PROVIDES THE LOCATION, AMPLITUDE, SSF, AND BSC OF EACH DETECTED ECHO. USING THE BSC, THE PARTICLES ARE CLASSIFIED INTO DIFFERENT TYPES, AND CONCENTRATION IS CALCULATED FOR EACH PARTICLE TYPE. 51

FIGURE 3-1. (A) MECHANICALLY SCANNED SINGLE ELEMENT TRANSDUCER IMAGING SYSTEM. (B) V3320, A 75 MHZ SPHERICALLY FOCUSED SINGLE ELEMENT TRANSDUCER. (C) PICOSOPE 5444B USED TO DIGITIZE THE OUTPUT SIGNAL FROM THE P/R. (D) 3-AXIS SCANNING STAGE BUILT FROM AN OPEN SOURCE CNC MILL KIT. (E) CLD, A LOW-NOISE LINEAR STEPPER MOTOR DRIVER. 55
FIGURE 3-2. (A) VISUALSONICS VEVO 2100 HIGH FREQUENCY ARRAY-BASED IMAGING SYSTEM. (B) MS550D, A SOLID-STATE LINEAR ARRAY PROBE WITH CENTER FREQUENCY OF 40 MHZ. (C) IMAGING SETUP WITH THE TRANSDUCER IN DIRECT CONTACT WITH THE SAMPLE. THE SAMPLE IS CONTAINED IN A POLYPROPYLENE CRYOGENIC VIAL. 56
FIGURE 3-3. VIALS USED FOR MANIPULATING SAMPLES. (A) DISPOSABLE BOROSILICATE GLASS CULTURE TUBE, 16 × 100 MM, 14 ML. (B) POLYPROPYLENE ROUND BOTTOM CRYOGENIC VIAL, 2 ML. 58
FIGURE 3-4. (A) DHC-F01 DISPOSABLE FUCHS-ROSENTHAL HEMOCYTOMETER. THERE ARE TWO CHAMBERS OF 3.2 ML PER SLIDE. 20 ML OF SAMPLE IS PIPETTED INTO THE CHAMBER AND EXAMINED UNDER AN OPTICAL MICROSCOPE AFTER SOME TIME TO LET THE PARTICLES SETTLE DOWN. (B) PHOTOGRAPH OF MICROSCOPE VIEW OF A 1 MM^2 REGION OF THE DHC-F01 HEMOCYTOMETER WITH 10 MM PS MICROSPHERE SAMPLE (450 PARTICLES/ML). 60
FIGURE 4-1. B-MODE IMAGES OF 10 MM PS MICROSPHERES SUSPENDED IN DISTILLED WATER ACQUIRED WITH MS (EXPERIMENT 1). FOUR CONCENTRATIONS ARE SHOWN: (A) SAMPLE 4, 5 PARTICLES/ML, (B) SAMPLE 5, 10 PARTICLES/ML, (C) SAMPLE 6, 20 PARTICLES/ML, AND (D) SAMPLE 7, 50 PARTICLES/ML. 65
FIGURE 4-2. RESULTS FROM PARTICLE DETECTION FOR 10 MM PS MICROSPHERE SAMPLES IMAGED WITH MS (SAMPLE 6, 20 PARTICLES/ML). (A) ECHO AMPLITUDES VS. LATERAL POSITIONS. (B) ECHO AMPLITUDES VS. AXIAL POSITIONS. (C) ECHO LATERAL STANDARD DEVIATIONS VS. AXIAL POSITIONS. (D) HISTOGRAM OF THE PEAK FREQUENCY IN BSC. 66
FIGURE 4-3. RESULTS FROM THE PARTICLE DETECTION SLICED ALONG THE AXIAL DIRECTION FOR 10 MM PS MICROSPHERE SAMPLES IMAGED WITH MS (SAMPLE 6, 20 PARTICLES/ML): (A) ECHO AMPLITUDES VS. AXIAL POSITIONS AND (B) ECHO LATERAL STANDARD DEVIATIONS VS. AXIAL POSITIONS. CALCULATED PARAMETERS: (C) NUMBER OF DETECTED ECHOES PER FRAME VS. AXIAL SLICES, (D) EFFECTIVE SLICE THICKNESS VS. AXIAL SLICES, AND (E) SLICE CONCENTRATION VS. AXIAL SLICES. THE BLACK DOTTED LINES IN THE PLOTS (C) – (E) REPRESENT THE ESTIMATED MEASUREMENT UNCERTAINTY AND THE RED DOTTED LINES REPRESENT THE DOF. 67
FIGURE 4-4. B-MODE IMAGES OF 10 MM PS MICROSPHERES SUSPENDED IN DISTILLED WATER ACQUIRED WITH VEVO (EXPERIMENT 2). FOUR CONCENTRATIONS ARE SHOWN: (A) 5 PARTICLES/ML, (B) 10 PARTICLES/ML, (C) 20 PARTICLES/ML, AND (D) 50 PARTICLES/ML. THE DIFFERENCE IN THE CONCENTRATION CAN BE CLEARLY SEEN FROM THE IMAGES. 69
FIGURE 4-5. RESULTS FROM PARTICLE DETECTION FOR 10 MM PS MICROSPHERE SAMPLES IMAGED WITH VEVO (SAMPLE 6, 20 PARTICLES/ML). (A) ECHO AMPLITUDES VS. LATERAL POSITIONS. (B) ECHO AMPLITUDES VS. AXIAL POSITIONS. (C) ECHO LATERAL STANDARD DEVIATION VS. AXIAL POSITIONS. (D) HISTOGRAM OF THE PEAK FREQUENCY IN THE RAW FREQUENCY SPECTRUM OF THE ECHO. 70
FIGURE 4-6. RESULTS FROM THE PARTICLE DETECTION SLICED ALONG THE AXIAL DIRECTION FOR 10 MM PS MICROSPHERE SAMPLES IMAGED WITH THE VEVO (SAMPLE 6, 20 PARTICLES/ML): (A) ECHO AMPLITUDES VS. AXIAL POSITIONS AND (B) ECHO LATERAL STANDARD DEVIATIONS VS. AXIAL POSITIONS. CALCULATED PARAMETERS: (C) NUMBER OF DETECTED ECHOES PER FRAME VS. AXIAL SLICES, (D) EFFECTIVE SLICE THICKNESS VS. AXIAL SLICES, AND (E) SLICE CONCENTRATION VS. AXIAL SLICES. THE BLACK DOTTED LINES IN THE PLOTS (C) – (E) REPRESENT THE ESTIMATED MEASUREMENT UNCERTAINTY AND THE RED DOTTED LINES REPRESENT THE DOF. 71
FIGURE 4-7. CONCENTRATION MEASUREMENT RESULTS FOR EXPERIMENT 1 AND 2. THE MEASUREMENTS MADE WITH MS SHOW GOOD AGREEMENT WITH THE HEMOCYTOMETER UP TO 200 PARTICLES/ML WHILE THE MEASUREMENTS MADE WITH VEVO SHOW GOOD AGREEMENT UP TO 50 PARTICLES/ML. THE VEVO STARTS TO FAIL AT LOWER CONCENTRATION BECAUSE ITS EFFECTIVE SLICE THICKNESS IS LARGER, AND THUS, THERE ARE MORE ECHOES VISIBLE IN THE IMAGE. 72

FIGURE 4-8. B-MODE IMAGES OF 15 MM PS MICROSPHERES SUSPENDED IN DISTILLED WATER ACQUIRED WITH MS (EXPERIMENT 3). FOUR CONCENTRATIONS ARE SHOWN: (A) 0.9 PARTICLES/ML, (B) 1.7 PARTICLES/ML, (C) 3.4 PARTICLES/ML, AND (D) 6.9 PARTICLES/ML. 74
FIGURE 4-9. RESULTS FROM PARTICLE DETECTION FOR 15 MM PS MICROSPHERE SAMPLES IMAGED WITH MS (SAMPLE 5, 13.7 PARTICLES/ML). (A) ECHO AMPLITUDES VS. LATERAL POSITIONS. (B) ECHO AMPLITUDES VS. AXIAL POSITIONS. (C) ECHO LATERAL STANDARD DEVIATION VS. AXIAL POSITIONS. (D) HISTOGRAM OF THE PEAK FREQUENCY IN THE BSC. 75
FIGURE 4-10. RESULTS FROM THE PARTICLE DETECTION SLICED ALONG THE AXIAL DIRECTION FOR 15 MM PS MICROSPHERE SAMPLES IMAGED WITH MS (SAMPLE 5, 13.7 PARTICLES/ML): (A) ECHO AMPLITUDES VS. AXIAL POSITIONS AND (B) ECHO LATERAL STANDARD DEVIATION VS. AXIAL POSITIONS. CALCULATED PARAMETERS: (C) NUMBER OF DETECTED ECHOES PER FRAME VS. AXIAL SLICES, (D) EFFECTIVE SLICE THICKNESS VS. AXIAL SLICES, AND (E) SLICE CONCENTRATION VS. AXIAL SLICES. THE BLACK DOTTED LINES IN THE PLOTS (C) – (E) REPRESENT THE ESTIMATED MEASUREMENT UNCERTAINTY AND THE RED DOTTED LINES REPRESENT THE DOF. 76
FIGURE 4-11. CONCENTRATION MEASUREMENT RESULTS FOR EXPERIMENT 3, 15 MM PS MICROSPHERES MEASURED WITH MS. THE ULTRASOUND METHOD SHOW GOOD AGREEMENT WITH THE HEMOCYTOMETER UP TO ABOUT 60 PARTICLES/MM. 78
FIGURE 4-12. B-MODE IMAGES OF 10 MM SILICA MICROSPHERES SUSPENDED IN DISTILLED WATER ACQUIRED WITH MS (EXPERIMENT 4). FOUR CONCENTRATIONS ARE SHOWN: (A) 3.8 PARTICLES/ML, (B) 7.5 PARTICLES/ML, (C) 15 PARTICLES/ML, AND (D) 30 PARTICLES/ML. 80
FIGURE 4-13. RESULTS FROM PARTICLE DETECTION FOR 10 MM SILICA MICROSPHERE SAMPLES IMAGED WITH MS (SAMPLE 8, 60 PARTICLES/ML). (A) ECHO AMPLITUDES VS. LATERAL POSITIONS. (B) ECHO AMPLITUDES VS. AXIAL POSITIONS. (C) ECHO LATERAL STANDARD DEVIATIONS VS. AXIAL POSITIONS. (D) HISTOGRAM OF THE PEAK FREQUENCY IN THE BSC. 81
FIGURE 4-14. RESULTS FROM THE PARTICLE DETECTION SLICED ALONG THE AXIAL DIRECTION FOR 10 MM SILICA MICROSPHERE SAMPLES IMAGED WITH MS (SAMPLE 8, 60 PARTICLES/ML): (A) ECHO AMPLITUDES VS. AXIAL POSITIONS AND (B) ECHO LATERAL STANDARD DEVIATIONS VS. AXIAL POSITIONS. CALCULATED PARAMETERS: (C) NUMBER OF DETECTED ECHOES PER FRAME VS. AXIAL SLICES, (D) EFFECTIVE SLICE THICKNESS VS. AXIAL SLICES, AND (E) SLICE CONCENTRATION VS. AXIAL SLICES. THE BLACK DOTTED LINES IN THE PLOTS (C) – (E) REPRESENT THE ESTIMATED MEASUREMENT UNCERTAINTY AND THE RED DOTTED LINES REPRESENT THE DOF. 82
FIGURE 4-15. CONCENTRATION MEASUREMENT RESULTS FOR EXPERIMENT 4, 10 MM SILICA MICROSPHERES MEASURED WITH MS. THE ULTRASOUND METHOD SHOW GOOD AGREEMENT WITH THE HEMOCYTOMETER UP TO ABOUT 120 PARTICLES/MM. 83
FIGURE 4-16. B-MODE IMAGES OF POLYDISPERSED SAMPLES OF 10 MM AND 15 MM PS MICROSPHERES SUSPENDED IN DISTILLED WATER ACQUIRED WITH MS (EXPERIMENT 5). FOUR SETS OF CONCENTRATIONS ARE SHOWN (10 MM PS:15 MM PS): (A) 1.5:2.5 PARTICLES/ML, (B) 3:2.5 PARTICLES/ML, (C) 6:2.5 PARTICLES/ML, AND (D) 12:2.5 PARTICLES/ML. 85
FIGURE 4-17. RESULTS FROM PARTICLE DETECTION FOR POLYDISPERSED SAMPLES OF 10 MM AND 15 MM PS MICROSPHERES SUSPENDED IN DISTILLED WATER ACQUIRED WITH MS (EXPERIMENT 5) (SAMPLE 4, 12:2.5 PARTICLES/ML). (A) ECHO AMPLITUDES VS. LATERAL POSITIONS. (B) ECHO LATERAL STANDARD DEVIATION VS. AXIAL POSITIONS. (C) CALCULATED EFFECTIVE SLICE THICKNESS VS. AXIAL SLICES. (D) CALCULATED SLICE PARTICLE CONCENTRATION VS. AXIAL SLICES. 86
FIGURE 4-18. CONCENTRATION MEASUREMENT RESULTS FOR EXPERIMENT 5. FOUR POLYDISPERSED SAMPLES OF 10 MM AND 15 MM PS MICROSPHERES ARE MEASURED WITH MS. (A) CONCENTRATION OF 10 MM PS MICROSPHERES (TOP) AND 15 MM PS MICROSPHERES (BOTTOM) FOR EACH SAMPLES. (B) HISTOGRAM OF THE PEAK FREQUENCY IN BSC OF DETECTED ECHOES AFTER CLASSIFICATION FOR EACH SAMPLE. 87
FIGURE 4-19. B-MODE IMAGES OF HUMAN T CELLS SUSPENDED IN PBS ACQUIRED WITH THE VEVO (EXPERIMENT 6). FOUR CONCENTRATIONS ARE SHOWN: (A) 9.4 CELLS/ML, (B) 18.8 CELLS/ML, (C) 37.5 CELLS/ML, AND (D) 75 CELLS/ML. 89

FIGURE 4-20. RESULTS FROM PARTICLE DETECTION FOR HUMAN T CELL SAMPLES IMAGED WITH MS (SAMPLE 7, 37.5 PARTICLES/ML). (A) ECHO AMPLITUDES VS. LATERAL POSITIONS. (B) ECHO AMPLITUDES VS. AXIAL POSITIONS. (C) ECHO LATERAL STANDARD DEVIATION VS. AXIAL POSITIONS. (D) HISTOGRAM OF THE PEAK FREQUENCY IN THE RAW FREQUENCY SPECTRUM OF THE ECHO. 90
FIGURE 4-21. RESULTS FROM THE PARTICLE DETECTION SLICED ALONG THE AXIAL DIRECTION FOR HUMAN T CELL SAMPLES IMAGED WITH MS (SAMPLE 7, 9.4 PARTICLES/ML): (A) ECHO AMPLITUDES VS. AXIAL POSITIONS AND (B) ECHO LATERAL STANDARD DEVIATION VS. AXIAL POSITIONS. CALCULATED PARAMETERS: (C) NUMBER OF DETECTED ECHOES PER FRAME VS. AXIAL SLICES, (D) EFFECTIVE SLICE THICKNESS VS. AXIAL SLICES, AND (E) SLICE CONCENTRATION VS. AXIAL SLICES. THE BLACK DOTTED LINES IN THE PLOTS (C) – (E) REPRESENT THE ESTIMATED MEASUREMENT UNCERTAINTY. 91
FIGURE 4-22. CONCENTRATION MEASUREMENT RESULTS FOR EXPERIMENT 6. T CELLS SUSPENDED IN PBS ARE MEASURED WITH THE VEVO.....92
FIGURE 5-1. PLOT OF COUNTS PER AREA (COUNTS/MM^2) VS. SAMPLE CONCENTRATION FOR DIFFERENT MEASUREMENTS SHOWING THE POINTS WHERE THE PARTICLE DETECTION STARTS TO FAIL. (A) 10 MM PS MICROSPHERES MEASURED WITH MS. (B) 15 MM PS MICROSPHERE MEASURED WITH MS. (C) 10 MM SILICA MICROSPHERE MEASURED WITH MS. (D) 10 MM PS MICROSPHERE MEASURED WITH THE VEVO.....97
FIGURE 5-2. PLOT OF MAXIMUM MEASURABLE CONCENTRATION VS. EFFECTIVE SLICE THICKNESS FOR EXPERIMENTS 1 THROUGH 4 AND 6 AND THE EXPONENTIAL FIT TO THE DATA. R^2 OF THE FIT IS 0.857. THE MAXIMUM MEASURABLE CONCENTRATION DECREASES EXPONENTIALLY AS THE EFFECTIVE SLICE THICKNESS INCREASES. 100
FIGURE 5-3. MEAN DEVIATION AND COEFFICIENT OF VARIATION FOR 10 MM PS MICROSPHERE SAMPLES FOR VARYING NUMBERS OF DETECTIONS USED IN PARTICLE CONCENTRATION CALCULATION. MEAN DEVIATION IS CALCULATED IN REFERENCE TO THE MEASUREMENT THAT USES 10,000 DETECTIONS. 103
FIGURE 6-1. ULTRASOUND-BASED CYTOMETRY. THE FLUID SAMPLE UNDER ANALYSIS IS CONTAINED IN AN ULTRASOUND TRANSPARENT VIAL. THE SAMPLE VIAL IS INSERTED INTO A WATER BATH. A HIGH FREQUENCY ULTRASOUND TRANSDUCER IMAGES THE SAMPLE THROUGH THE WATER. THE IMAGES ARE PROCESSED TO PERFORM TYPE DIFFERENTIAL AND TYPE-SPECIFIC CONCENTRATION MEASUREMENT. 112
FIGURE 6-2. TRANSDUCER CHARACTERIZATION METHOD BASED ON PARTICLE SUSPENSION MEASUREMENT.....114

List of Tables

TABLE 1-1. WBC, PROTEIN, AND GLUCOSE CONCENTRATION THRESHOLD FOR HEALTHY AND INFECTED CSF. 25
TABLE 3-1. EXPERIMENTS PERFORMED TO DEMONSTRATE THE PROPOSED METHOD. 59
TABLE 5-1. CALCULATED EFFECTIVE SLICE THICKNESS AND MAXIMUM MEASURABLE CONCENTRATION FOR DIFFERENT MEASUREMENTS. 95

1. Introduction

Concentration measurement of particles in suspension is an important procedure performed in various industries including basic biology, pharmaceutics, and clinical medicine. In biological and biotechnological laboratories, cell concentration is routinely measured to monitor cell growth and the progression of experiments. In clinical laboratories, white blood cell (WBC) and red blood cell (RBC) concentrations are key parameters measured for blood and cerebrospinal fluid (CSF) samples.

In this chapter, we first describe existing methods for measuring the concentration of particles in suspension in Section 1.1. The characteristics of the methods are discussed as well as their key limitations. In Section 1.2, an overview of the framework developed in the field of quantitative ultrasound for analysis of fluid and particle suspension is provided. In addition, a literature review of some of the key publications in this field is provided including their key achievements and limitations. The overview of the proposed method is discussed in Section 1.3 followed by an introduction of the key clinical application of the proposed method in Section 1.4. Finally, the organization of the thesis is provided in Section 1.5.

1.1 Existing Particle Concentration Measurement Methods

Several existing instruments and methods for measuring particle concentration are available including hemocytometers, also known as counting chambers, coulter counters, and flow cytometers. Examples of these instruments are shown in Figure 1-1. The most often used method in the laboratory setting utilizes a hemocytometer, a microscope slide with a precisely manufactured chamber of a known volume. There are different types of hemocytometers depending on the size of the chamber, and their applications differ depending on the range of concentration of the sample being analyzed. An Improved Neubauer hemocytometer and its grid

are shown in Figure 1-1 (a) and (b), respectively. The sample is placed in the chamber and particles are counted under an optical microscope. The concentration is measured by dividing the number of particles counted by the volume of the chamber. Measurements are repeated in order to increase accuracy.

Another method involves the Coulter counter shown in Figure 1-1 (c), which is an automatic particle counting and sizing instrument. It employs a technique based on impedance measurement, referred to as the Coulter principle, and operates by passing individual particles through a small orifice and sensing the impedance change caused by the presence of the particle [1]–[3]. The impedance change can be also used to estimate the size of the particle.

A flow cytometer shown in Figure 1-1 (d) is another instrument that can automatically measure particle concentration, although it has additional capabilities. A flow cytometer can precisely align the particles in a single line using laminar fluid flow, and analyzes individual particles for their impedance using the Coulter principle, or for their optical response using lasers. Flow cytometers can also actively separate and sort the particles based on their response, resulting in the flow cytometer's status as an indispensable instrument for life science research. Although powerful instruments, absolute particle concentration measurement in flow cytometers is not straightforward; while they can precisely count the number of particles, they generally do not track the total volume that is analyzed. To solve this issue, reference particles, also known as absolute count beads, of a well-characterized concentration are added to the sample. By counting the reference particles, the volume analyzed can be calculated, from which concentration of the sample particles can be measured [4].

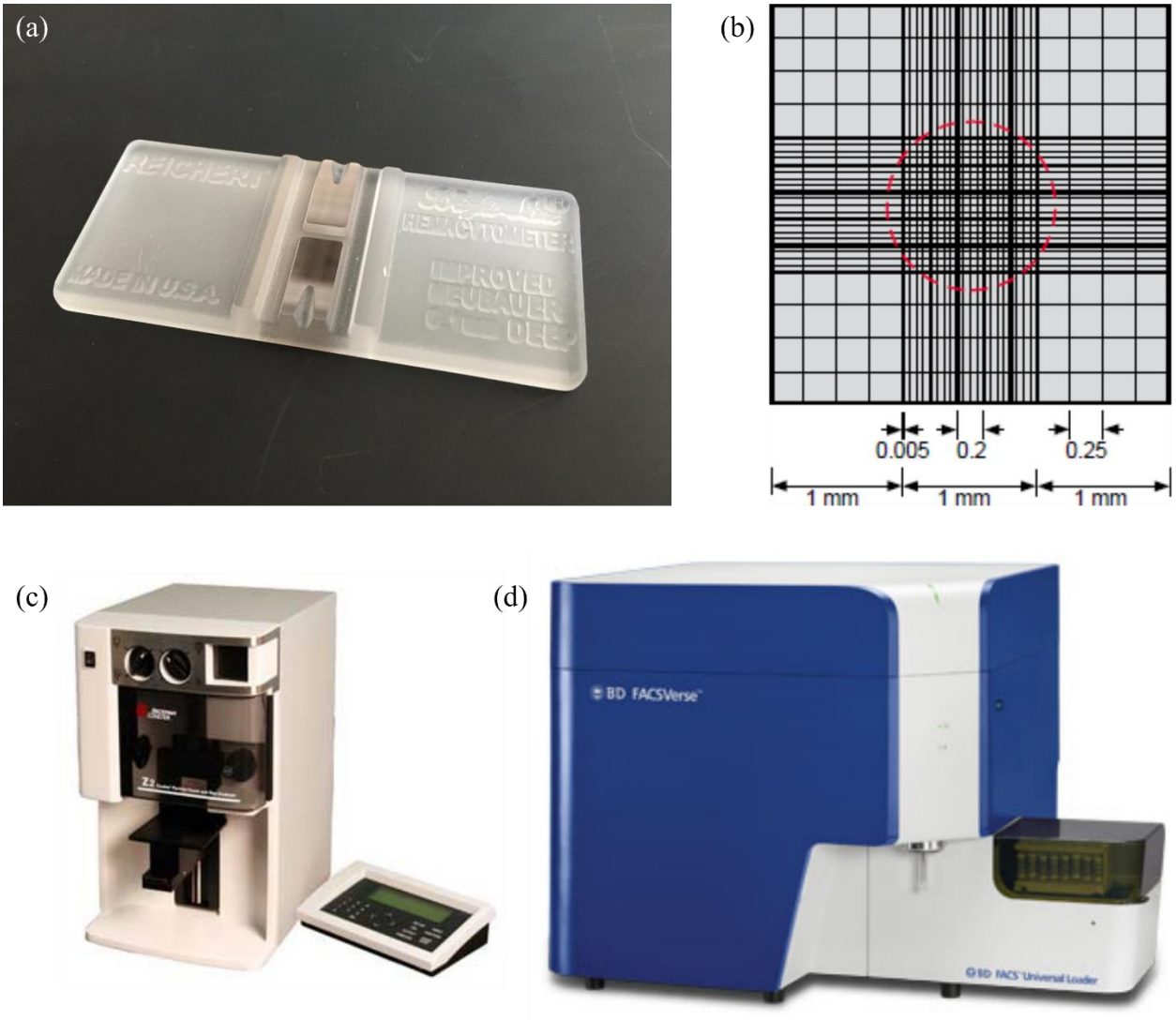

Figure 1-1. (a) Improved Neubauer hemocytometer. (b) Grid for Improved Neubauer hemocytometer (image source: http://www.marienfeld-superior.com). (c) Coulter counter, Beckman Coulter Z2 (image source: www.bckmancoulter.com) (d) Flow cytometer BD FACSVerse (image source: www.bdbioscience.com).

While these methods work well, they are not without limitations. The hemocytometer requires substantial manual handling that makes measurement time-consuming and laborious, and requires a well-trained technician to achieve accurate results. Also, due to its small analysis volume, it is less accurate for low concentration samples such as CSF [5]–[7]. The Coulter counter is automated and works well, but it is also less accurate for low concentration samples due to background electrical noise [5], [8]. The flow cytometer is a powerful instrument, but

expensive due to its many functions, and it requires the additional step of adding absolute count beads, which becomes a source of additional cost and error.

Ultrasound, on the other hand, provides several unique advantages for fluid sample analysis. At the typical level of acoustic energy used for ultrasound imaging, the method is nondestructive, which allows analyzing biological samples such as cells without harming them [9]–[11]. It can also be non-contact such that the sample can be analyzed while in the collection vial if the vial is ultrasound transparent. This allows the sample to be analyzed without being contaminated, and thus the same sample can be used for other analyses reducing the overall required volume to be collected. Also, because the sample does not have to be discarded after analysis, a larger volume of the sample can be analyzed, thus increasing accuracy, especially for lower concentration samples.

1.2 Quantitative Ultrasound

Estimation of particle concentration using ultrasound is not a new idea. There has been a significant amount of research in the field of quantitative ultrasound (QUS). QUS is a topic within the field of ultrasound focusing on tissue characterization based on the theory that ultrasound backscatter signal from a material has a specific spectral signature. One of the most significant developments under QUS is the concept of backscatter coefficient (BSC), a parameter derived by normalizing the backscatter intensity by the incident intensity. When normalization is done correctly, the BSC is a function of only the material and independent of the transducer characteristics, experimental setup, or the operator. The integrated backscatter coefficient (IBC), an integration of BSC over the frequency band of interest, is another key parameter often used in QUS. The BSC framework proposes that BSC and IBC can be used to characterize the size and

concentration of small scatterers contained within a material. The following discussion introduces the key literature in QUS and fluid sample analysis based on BSC and IBC.

The theoretical framework for BSC was developed by Lizzi et al. [12], [13] and Insana et al. [14]. The framework is based on fitting the BSC to a theoretical scattering model such as the one developed by Faran [15] to extract parameters relevant to the population of scatterers within the object. Since the initial development, there have been extensive studies on phantom as well as biological tissues in pre-clinical and clinical settings using this approach. Some of these works focus on individual cells [16], studies of blood [17], [18], and tissue-mimicking phantoms [19].

Tunis et al. [20] discuss experimental results using acute myeloid leukemia cells (OCI-AML5) and prostate adenocarcinoma cells (PC-3) suspended in phosphate-buffered saline (PBS) solution. A 20 MHz spherically focused transducer is used to measure the sample. Tunis and coworkers show that the fit parameters, a and c/v, of a generalized gamma distribution have an increasing trend with increasing cell concentration. However, they are able to show only a trend with concentration, and do not provide any means to achieve an absolute measurement.

Leithem et al. [21] use glass beads and ultrasound contrast agents to demonstrate a BSC-based concentration measurement technique. The measurements are made with a 20 MHz spherically focused transducer. The concentration range studied is greater than 1000 particles/μL. They use a Levenberg-Marquardt [22], [23] regression technique to fit the measured data to a theoretical scattering model by Faran. Particle size distribution and concentration are extracted from the fit. The result from the fit is compared against hemocytometer result, and the two show close agreement. This work does provide a way to estimate the absolute concentration; however, this method strongly depends on the accuracy of the model being used to fit the data. If the

sample or the measurement condition changes such that the model does not accurately estimate the attenuation, this method will not work.

Mercado et al. [24] estimate relative cell concentration in 3D engineered tissue using high-frequency ultrasound. This work seeks to address the need in engineered tissue fabrication for nondestructively characterizing and monitoring the cellular properties of the engineered tissue. Mercado et al. use 30 and 38 MHz spherically focused single element transducers to scan the sample, which have varying concentrations ranging from 10 to 1000 cells/μL. They calculate the BSC and IBC from the measurements. Samples without any cells and with low concentration of cells at 10 cells/μL are excluded from the analysis because the backscatter energy from the sample is too low. IBC from higher concentration samples is found to increase linearly with cell concentration. As in other works, this work is able to show only the relative measure of concentration and does not provide any means to acquire absolute concentration. In addition, their method fails at low concentrations because backscatter energy from a low concentration sample is not high enough to be reliably detected.

More recently, Elvira et al. [25] and Jimenez et al. [26] present their work on measuring low concentration cell suspension using the BSC method. Elvira et al. show concentration measurement results of *Saccharomyces cerevisiae* suspension samples. They use a 50 MHz transducer to measure the backscattered signal from the sample. The echoes from the cells are detected by using the Non-negative Matrix Factorization denoising technique. They are able to measure relative concentration for samples with concentrations from 10 to 1000 cells/μL.

Jimenez et al. show concentration measurement of WBC, with the goal of eventual CSF analysis application. They use a 75 MHz transducer to measure the backscattered signal from the

WBC suspension. The BSC of the samples are used to provide the relative concentration of the samples. Although the work states that they are able to measure 0 to 50 cells/μL, the presented results for the lower concentration range are not accurate, which is likely due to the fact that the backscattered energy is too low. More importantly, neither Elvira et al., nor Jimenez et al., are able to provide a measurement of the absolute concentration, which significantly limits the applications.

The BSC and IBC based methods that have been developed so far can provide relative concentration between different samples, but are not able to reliably measure absolute concentration without some type of additional calibration or reference measurements. This limitation is especially non-ideal for *in vivo* applications where accurate reference measurement is difficult if not impossible. Model-based approaches as in [21] are challenging in *in vivo* applications due to high intra- and inter-patient variability observed in biological parameters. Also, BSC and IBC based methods are not suitable for samples with low concentration because the backscatter energy is not high enough to be reliably detected. With any realistic amount of attenuation expected in a real measurement setting, the backscattered energy from a low concentration sample will likely be buried under noise.

1.3 The Proposed Method

The proposed method in this work departs from the traditional framework of QUS, which relies on frequency domain analysis, and approaches the problem in the spatial domain. It has been shown that when the particle concentration is low and the particle size is similar to the wavelength of the ultrasound, individual particles can be distinguished in B-mode ultrasound images [27], [28]. This is different from resolving particles, since resolution requires that the wavelength of the ultrasound be smaller than the object being imaged. Rather, the particles are

distinguished if there is no more than one particle per resolution cell of the ultrasound beam. This allows for detection and counting of the particles visible in an image, making it possible to obtain the number of particles per image. While this can be done relatively easily, measuring the absolute concentration requires knowing also the volume being analyzed by the ultrasound image, which is challenging because the out-of-plane thickness of the image, or the slice thickness, is unknown. One might attempt to use the typical -6 dB beam width to estimate the thickness, but as will be discussed in Section 2.1, the actual beam width interacting with the particles in a sample is dependent on not only the imaging system, but also on the acoustic characteristics of the sample. Therefore, using a fixed beam width as the slice thickness will lead to an incorrect result.

This work proposes a method for using B-mode images to measure absolute concentration of particles in suspension for low concentration samples. The method is based on detecting individual particles in the image to acquire a particle count and using the characteristics of the echoes to estimate the volume analyzed by the image. The method is entirely image-based and does not require any prior characterization of the sample. A preliminary result from this work has been published [29], which proposed a method for measuring particle concentration from B-mode images acquired with a mechanically scanned radially-symmetric single element transducer. In this thesis, the theoretical background for the proposed method is further developed and the method is generalized to be applicable for other types of imaging systems including arrays, which is essential for *in vivo* clinical use cases.

1.4 *In Vivo* Clinical Application

While the proposed method is a general one that can be applied to a wide range of applications, *in vivo* clinical application targeting neonatal bacterial meningitis (BM) is unique and interesting and provides a strong motivation for this work.

BM is an acute inflammation of the meninges usually caused by bacterial infection of the CSF. It is a serious condition that if untreated, can lead to neurological damage and even death within 48 hours [30]. The prevalence of BM is generally low, although it is region-dependent, with around 600 cases in the United States and around 4000 cases in the world annually [31]. Death rate is high at around 10%, with 30 – 50% suffering disabilities such as cognitive damage and hearing loss [32], [33]. Newborns and young infants (1 to 3 months) are at a higher risk for BM because their immune systems are not fully developed, so the initial diagnosis and monitoring of the progress in these populations is extremely important [33].

Currently, when young infants present fever without source (FWS) and overall healthy appearance, blood and urine analysis, and lumbar puncture (LP) are performed. Due to the severity and rapid progression of the disease, treatment for BM using broad range antibiotics typically begins immediately even without a conclusive diagnosis [34], [35]. Due to its low prevalence, around 90% of LPs show negative result for BM in the United States [36]. This is despite the fact that LP is a highly invasive and painful procedure even for adults and the fact that treatment is a form of aggressive antibiotics that could have severe side effects. In addition, due to procedural difficulty especially with young infants, the rate of traumatic LP, where the procedure results in unsuccessful acquisition of CSF sample, is high. Therefore, there is a significant need for a device that can provide clinicians with a way to screen and diagnose young

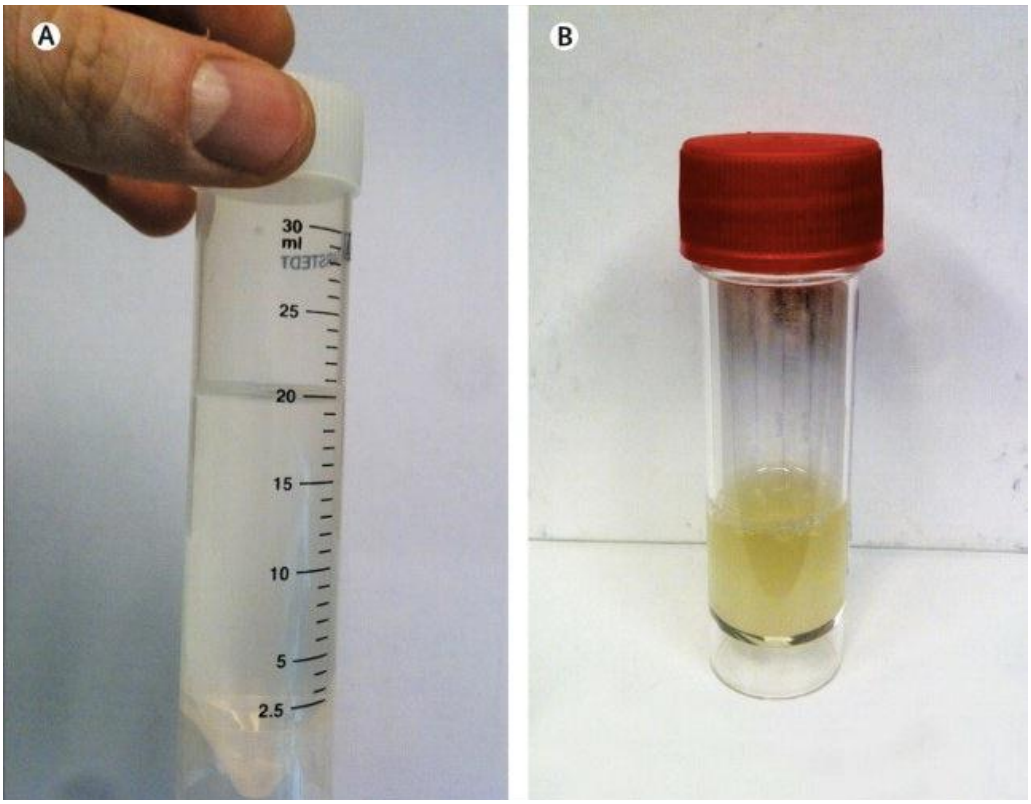

Figure 1-2. A comparison between normal and infected CSF [37]. (a) Normal CSF should be clear and water-like in appearance. (b) Infected CSF can become yellow and turbid due to increased cellularity and protein.

infants with symptoms in order to reduce unnecessary LPs as well as avoid aggressive treatment that may be unnecessary.

Once the CSF sample is acquired through LP, WBC type and concentration is measured along with protein and glucose concentrations. Also, the CSF sample is cultured to identify the bacteria causing the infection. CSF culture is the most accurate method of diagnosis, and identification of bacteria helps target the treatment [35]. However, the culture requires relatively long time (1 to 3 days) compared to the fast progression of BM. Therefore, although LP can provide accurate diagnosis, the discomfort and difficulty of the procedure, as well as the long wait time, renders LP a suboptimal diagnostic tool. In addition, due to the invasive nature of the procedure, it cannot be done regularly, rendering LP a suboptimal monitoring tool as well.

It is established that WBC, protein, and glucose levels in CFS are good indicators of infection, although they cannot give conclusive diagnosis. These parameters are currently used to assist clinicians' decisions before the result of the culture. Figure 1-2 shows the change in color and turbidity of CSF with infection due to changes in these parameters [37]. In case of BM, increase in WBC and protein concentrations and decrease in glucose concentration are observed in most cases. Although these parameters cannot replace CSF culture, they have the potential to be used as a screening method or a monitoring method for BM. However, currently there is no way to measure these parameters noninvasively without an LP.

The criteria for WBC, protein, and glucose levels differ for different countries, regions, hospitals and clinicians [38], [39], but the consensus among the collaborating clinicians at Boston Children's Hospital is shown in Table 1-1.

Table 1-1. WBC, protein, and glucose concentration threshold for healthy and infected CSF.

	WBC (cells/μL)	Protein (g/L)	Glucose (g/L)
Healthy	0 – 10	0.5 – 1	> 4
Infected	> 10	> 1	< 4

While an LP is unavoidable for CSF culture, a method that can measure WBC, protein, and glucose concentrations easily and noninvasively has the potential to be used as a screening mechanism to assist clinicians' decision on LP and treatment. Also such method can also be used as a monitor mechanism, which can provide an indication of the disease or treatment progress.

WBC concentration measurement has the potential to be done noninvasively with ultrasound imaging. Newborns and young infants have a special advantage of having fontanels, also called "soft spots" that are areas on the head where there is an opening in the skull. This provides an acoustic window through which ultrasound imaging can be done. CSF is accessible through the

fontanelle, less than ~ 5 mm from the skin surface. In fact, transfontanel ultrasound imaging is regularly done, but at a much lower frequency mainly to image the brain.

Two types of WBCs, neutrophils and lymphocytes, can be found in the CSF in case of BM. The size of these cells is in the range of 10 – 15 μm diameter while protein and glucose are much smaller, in the nm range. The spatial resolution of high frequency ultrasound is in the same range as the size of WBCs, which means that even imaging and detection of individual WBCs are possible. Previous work indeed showed that 20 MHz ultrasound can image individual WBCs (Figure 1-3) [27].

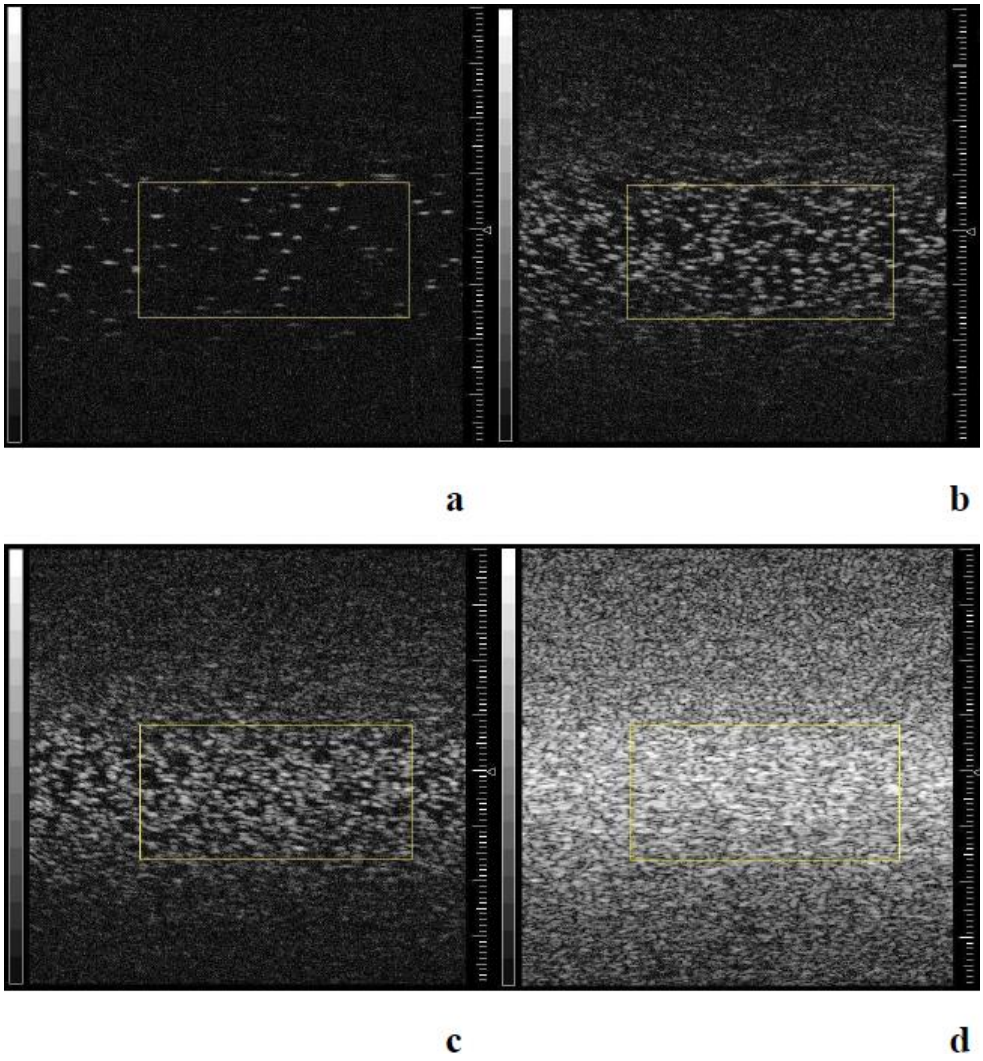

Figure 1-3. Ultrasound images from [27] showing different concentration of AML cell solutions (a) 0.0025%, (b) 0.05%, (c) 0.1% and (d) 0.8%. When concentration is low, the echoes from individual cells can be clearly distinguished in the image. However, when the concentration is high, individual echoes can no longer be distinguished. This occurs due to having more than one cell in the resolution cell of the beam.

The ability to measure CSF WBC concentration noninvasively without an LP has the potential to reduce the unnecessary LPs and enable the monitoring of the progression of the disease. The proposed method in this work provides a way to achieve this, and thus has the potential to affect the treatment of neonatal meningitis in a significant way.

1.5 Organization of Thesis

The thesis is organized as follows. The background and motivation for this work is discussed in Chapter 0, including an overview of the *in vivo* clinical application involving neonatal BM. In Chapter 2, the background and formulation of the proposed method are described in detail, including an overview of our implementation of the proposed method. The details of the imaging systems, samples, and the setup of the experiments are described in Chapter 3. Reference measurement and statistical analyses methods are also discussed. In Chapter 4, the key findings from six experiments using different sample types and imaging systems are presented to demonstrate the success of the proposed approach. In Chapter 5, detailed discussion of key aspects of the proposed method are presented. In Chapter 6, the contributions of this work is summarized followed by the discussion of future work entailing possible improvements and extensions to the proposed method.

2. Method Description

In this chapter, we describe the proposed method in detail including the important principles behind the method and the exact implementation of the method. First, an overview of the proposed method and the fundamental principles behind the method are discussed in Section 2.1. In Section 2.2, particle detection and parameter extraction steps necessary for the method are discussed. This is followed by the derivation of the effective slice thickness calculation for radially symmetric transducers in Section 2.3. The derived result is extended to a more general case, including array transducers in Section 2.4 followed by the implementation of the method in Section 2.5. In Section 2.6, the estimation of the uncertainty associated with different parameters is discussed. The method is summarized in Section 2.7.

2.1 Overview

The coordinate system used throughout this work is shown in Figure 2-1 and is defined as follows. The transducer is at the top of the image and the transmitted ultrasound beam propagates downward. The axial direction (z-axis) and lateral direction (x-axis) are along the depth and the width of the image, respectively. The elevational direction (y-axis) is perpendicular to the image plane. The origin ($x = 0, y = 0, z = 0$) is located at the top left corner of the image. The image plane is located at $y = 0$. The slice thickness refers to the out-of-plane thickness of the image.

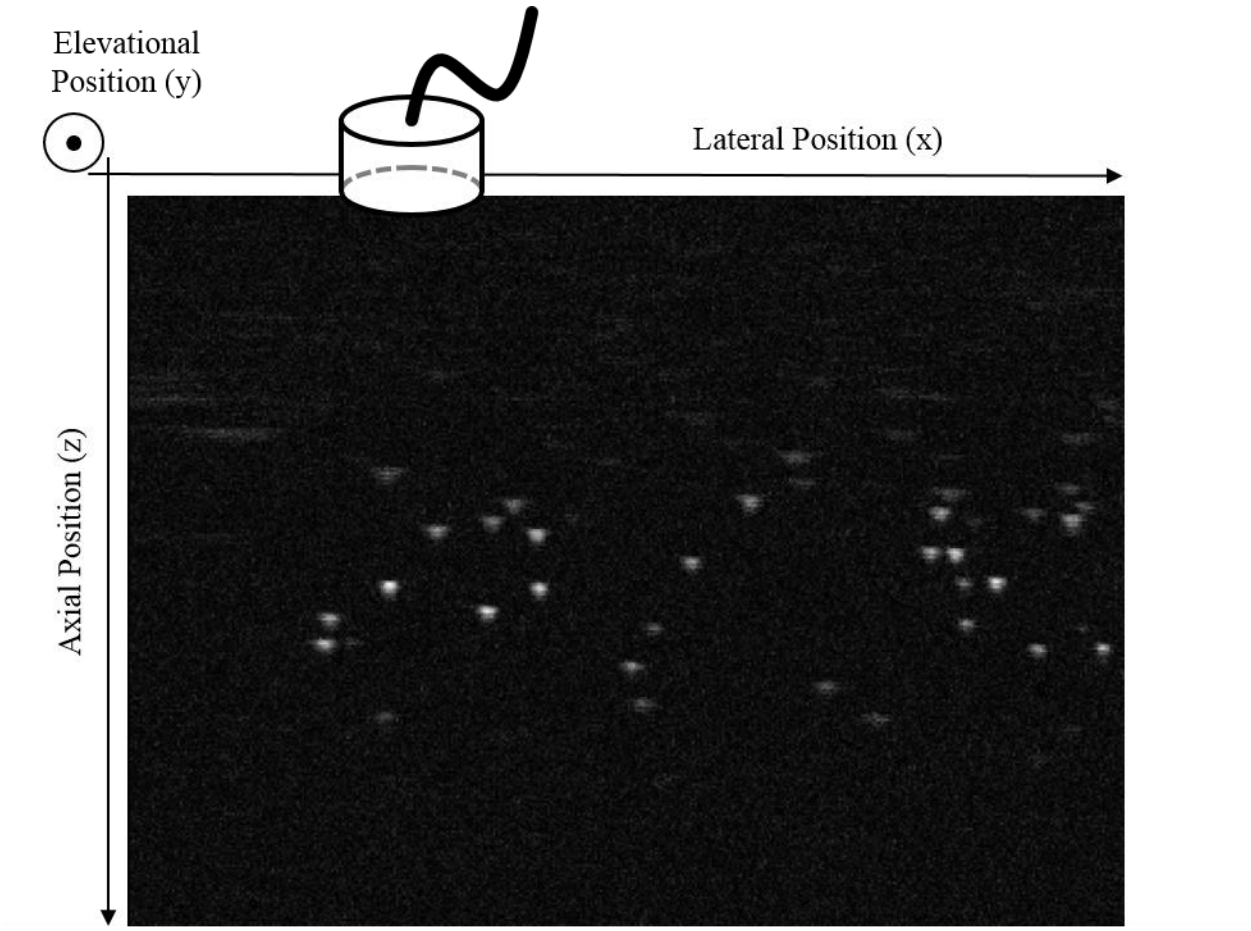

Figure 2-1. Coordinate system used in this work. It is assumed that the transducer is at the top of the image and the direction of the transmitted ultrasound beam is downward. The axial direction (z-axis) is along the depth of the image. The lateral direction (x-axis) is along the width of the image. The elevational direction (y-axis) is perpendicular to the image plane (out-of-plane).

The goal of this work is to measure the concentration of particles in suspension using high frequency B-mode ultrasound imaging. It has been shown that when the wavelength of the ultrasound is on the order of the scatterer size and the concentration of scatterers is low such that there is no more than one scatterer per resolution cell of the beam, individual scatterers can be identified in the resulting B-mode image [11], [27], [28]. Figure 2-2 shows B-mode images of monodispersed sample of 15 μm polystyrene (PS) microspheres suspended in distilled water. The image is acquired by mechanically scanning a single element transducer.

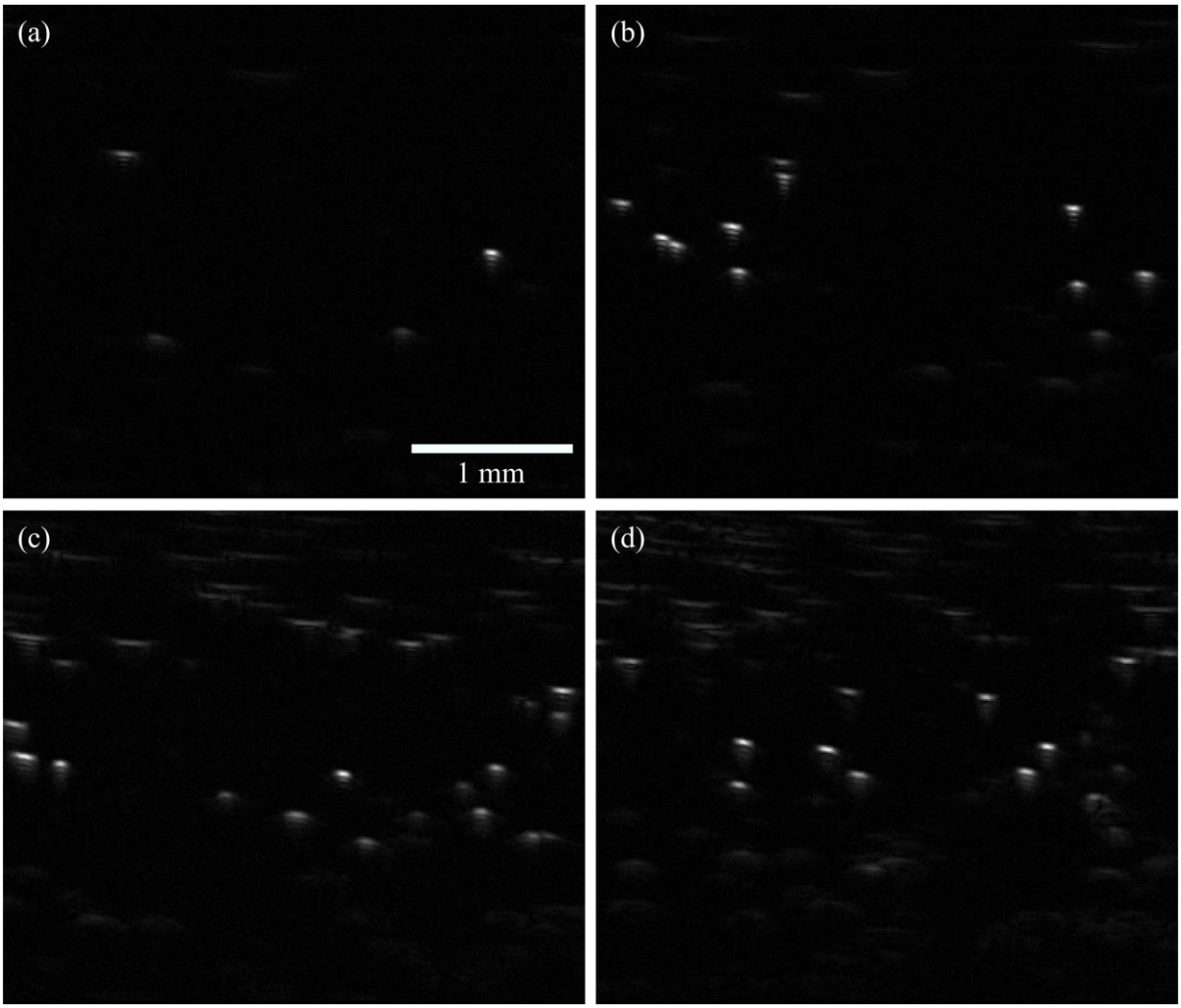

Figure 2-2. B-mode images of 15 μm PS microspheres suspended in distilled water acquired with mechanically scanned single element transducer. Four concentrations are shown: (a) 0.9 particles/μL, (b) 1.7 particles/μL, (c) 3.4 particles/μL, and (d) 6.9 particles/μL. Individual particles can be distinguished in the images because the particle concentration is low.

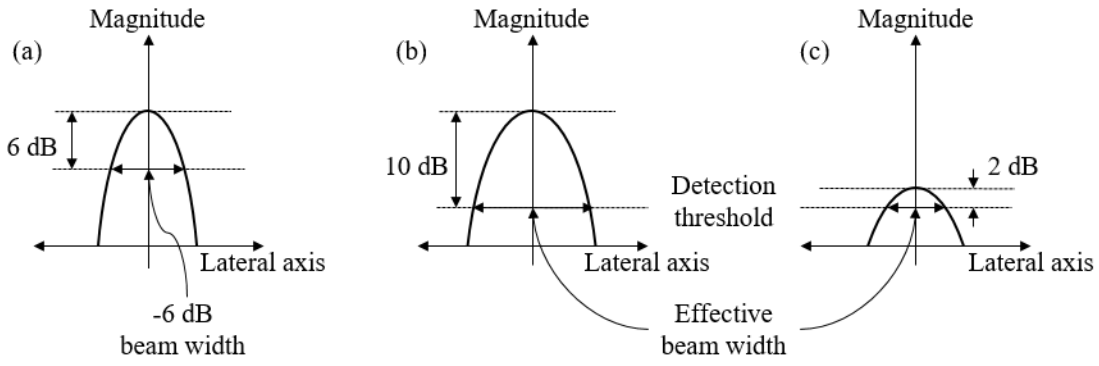

Figure 2-3. Description of effective beam width. (a) Conventional -6 dB beam width defined in reference to the peak intensity of the beam. (b) Effective beam width when the maximum echo intensity is 10 dB above the detection threshold, and (c) 2 dB above the detection threshold.

Calculating the concentration requires quantifying both the number of particles and the volume of the sample that is analyzed. Given the B-mode images of the sample, it is relatively straightforward to determine the number of particles visible in the image by using various existing particle detection methods. However, quantifying the volume being analyzed by the image is difficult because the slice thickness of the image depends not only on the beam characteristics, but also on the characteristics of the particles, the suspension media, and the experimental setup. This means that the slice thickness cannot be estimated by using the beam width calculated from the beam characteristics only, such as the -6 dB beam width.

In order to facilitate the discussion of the proposed method, the concept of effective beam width is introduced here. The term *effective* is used to convey that the beam width is not referring to a single quantity defined by the beam characteristics alone, but rather is a quantity that depends on the entire setup of the measurement, including the imaging system and the sample. The effective beam width can be defined as the extent to which a scatterer can deviate from the axis of the transducer and still produce an echo that can be detected in the image.

There is an important distinction between the effective beam width and the typically quoted -6 dB beam width. As shown in Figure 2-3 (a), -6 dB beam width is determined from the beam profile and measured in reference to the maximum intensity of the beam at a given axial position. Therefore, it depends only on the beam characteristics and is independent of the sample being imaged. On the other hand, the effective beam width is determined from the pulse-echo beam profile from a real physical scatterer, which means that it depends also on the characteristics of the sample such as the size, shape, and echogenicity of the scatterer and the attenuation of the medium. As shown in Figure 2-3 (b) and (c), depending on the echogenicity of the scatterer, the resulting effective beam width can vary widely. Characterizing the effective beam width allows capturing the aggregate effect of the interaction between the beam and the sample without having to characterize each separately.

We suggest that the effective beam width in the lateral direction can be characterized directly from the image. The proposed method utilizes the phenomenon of scatterer spreading in order to quantify the effective lateral beam width, which is then used to estimate the effective elevational beam width or equivalently, the effective slice thickness. The scatterer spread function (SSF), which quantifies the extent of scatterer spreading, is similar in concept to the point spread function (PSF). While the PSF describes the spreading observed in the resulting image from an ideal point object and expresses the impulse response of the imaging system, the SSF describes the spreading observed in the image due to a physical scatterer. Scatterer spreading occurs because the echo from a scatterer is visible on multiple scan lines due to the nonzero lateral beam width and the nonzero size of the physical scatterer. Since scatterer spreading is the consequence of the interaction between the beam and the physical scatterer, quantifying the amount of spreading provides information about the effective lateral beam width.

The proposed method is based on detecting and characterizing the amplitude and SSF of echoes from the particles and using them to estimate the effective slice thickness of the image. Since the characterization is directly from the image of the sample, the method can adapt to each measurement setup without the need for a calibration or reference measurement.

2.2 Particle Detection

Particle detection is performed on envelope-detected images by locating the echoes from individual particles. The detection algorithm is run on all frames that are acquired during the measurement. To improve detection accuracy, noise reduction is performed by using a median filter and a 2D Gaussian filter. The particle detection is performed using an algorithm based on template matching with a 2D Gaussian as the template. A more sophisticated template may be used based on some general prior knowledge about the scatterers, or a template could be extracted from training data.

In the following discussion, data acquired from a 15 μm PS microsphere sample (55 particles/μL) by scanning a high frequency radially-symmetric single element transducer is used as an example. Figure 2-4 shows the result of the particle detection and the parameter extraction steps. Figure 2-4 (a) shows a B-mode image of the sample and the result of the detection marked by red circles. For each echo, the corresponding location in the 2-dimensional (2D) radio frequency (RF) data is extracted for BSC calculation as shown in Figure 2-4 (b). The echo envelope is fitted to a 2D Gaussian as shown in Figure 2-4 (c) to estimate its amplitude, position, and lateral standard deviation, which is used to characterize its SSF. The axial and lateral positions of the particle are determined from the location of the centroid of the Gaussian fitting. The BSC along the axial direction is calculated by averaging the magnitude of the Fourier transforms of each scan line and dividing by the flat reflector measurement as shown in (1). N is

the number of scan lines in the extracted RF data, $H_i(f)$ is the Fourier transform of the i^{th} scan line, and $H_{flat}(f)$ is the Fourier transform of the flat reflector measurement . The magnitude of the BSC is normalized with reference to the magnitude of the first peak since its absolute magnitude is not needed. The BSC for the given echo is shown in Figure 2-4 (d). The frequency of the first peak in the BSC is used for particle type clustering, which enables the measurement of concentration of each type of particles present in the sample.

$$Normalized\ BSC = Normalize\left(\left|\frac{\frac{1}{N}\sum_{i=1}^{N} H_i(f)}{H_{flat}(f)}\right|^2\right) \quad (1)$$

The detection results from all measured frames are shown in Figure 2-5. The scatter plot of the detected echoes' amplitude vs. lateral position and axial position are shown in Figure 2-5 (a) and (b), respectively. Figure 2-5 (c) shows the scatter plot of the lateral standard deviation vs. axial position. Each point in the scatter plots represents an echo that is detected in the image. Figure 2-5 (d) shows the histogram of the peak frequency from the BSC of each echo.

As expected, Figure 2-5 (a) shows that the echo amplitude has no visible dependency on its lateral position. This is because the scanning, whether done mechanically or electronically, is along the lateral direction. Therefore, ignoring the effect near the edge of the transducer in the case of array imaging, the characteristics of the beam should remain unchanged from one scan line to another. However, at a given lateral position, a wide range of amplitudes is observed. This variation is due to the differences in the axial and elevational position of the scatterers.

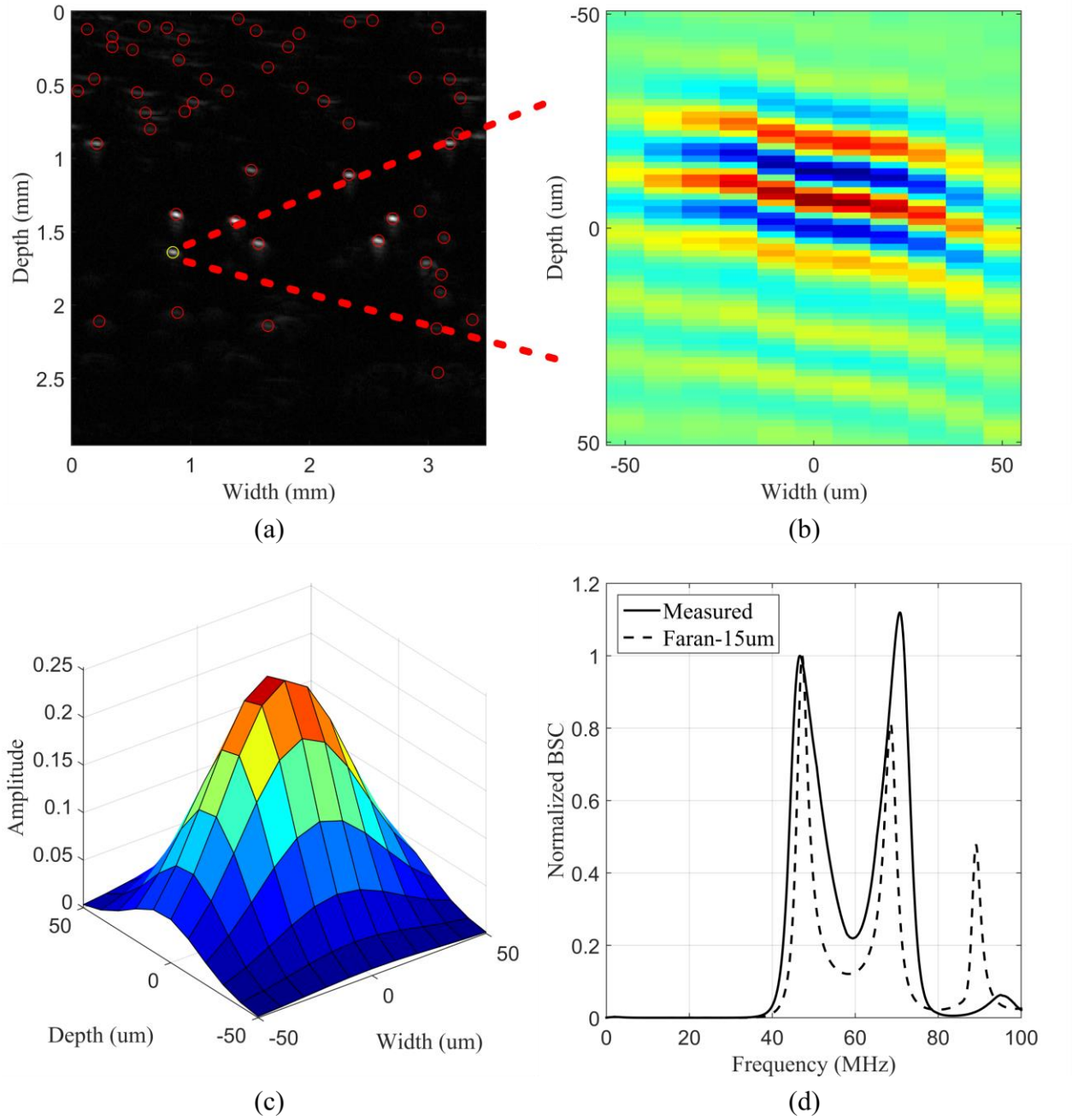

Figure 2-4. (a) A B-mode image of 15 μm PS microsphere suspension. The detected particles are marked by red circles. (b) The corresponding 2D RF data for the echo marked by the yellow circle. (c) 2D Gaussian fitting of the corresponding echo to extract its amplitude, position, and lateral standard deviation. (d) Normalized BSC for the echo compared to the Faran model for a 15 μm diameter PS microsphere.

On the other hand, as shown in Figure 2-5 (b), the echo amplitude shows a strong dependence on its axial position (depth). The amplitude reaches a maximum around the focal point of the transducer, which, in this case, is at 12.7 mm, because the acoustic energy is the highest around the focal point. At a given axial position, a large range of amplitudes is observed. This variation must result from the differences in the elevational position of the scatterers since it has already been shown that the amplitude does not depend on the lateral position. The elevational position of the scatterer has a strong effect on the echo amplitude. The amplitude reaches its maximum when the scatterer is located on the imaging plane ($y = 0$), and decreases as the scatterer location deviates away from the imaging plane.

The standard deviation also shows some dependency on the axial position as seen in Figure 2-5 (c), but, at a given axial position, there is only a small range of variation. This shows that while the echo amplitude is strongly affected by the elevational position, the lateral standard deviation and therefore SSF remain relatively constant. This is an important observation that supports the assumption required to derive the relationship between the echo amplitude and the effective lateral and elevational beam width, discussed in the next section.

Finally, the histogram in Figure 2-5 (d) shows that the peak frequencies are distributed around 50 MHz as predicted by the Faran model for 15 μm PS microspheres [15], [40]. In monodispersed samples, the peak frequencies are used to select only the particles of interest and remove any echoes from unwanted scatterers such as microbubbles or other impurities in the sample. In polydispersed samples, the peak frequencies are used to cluster the scatterers such that the concentration of each particle type can be calculated.

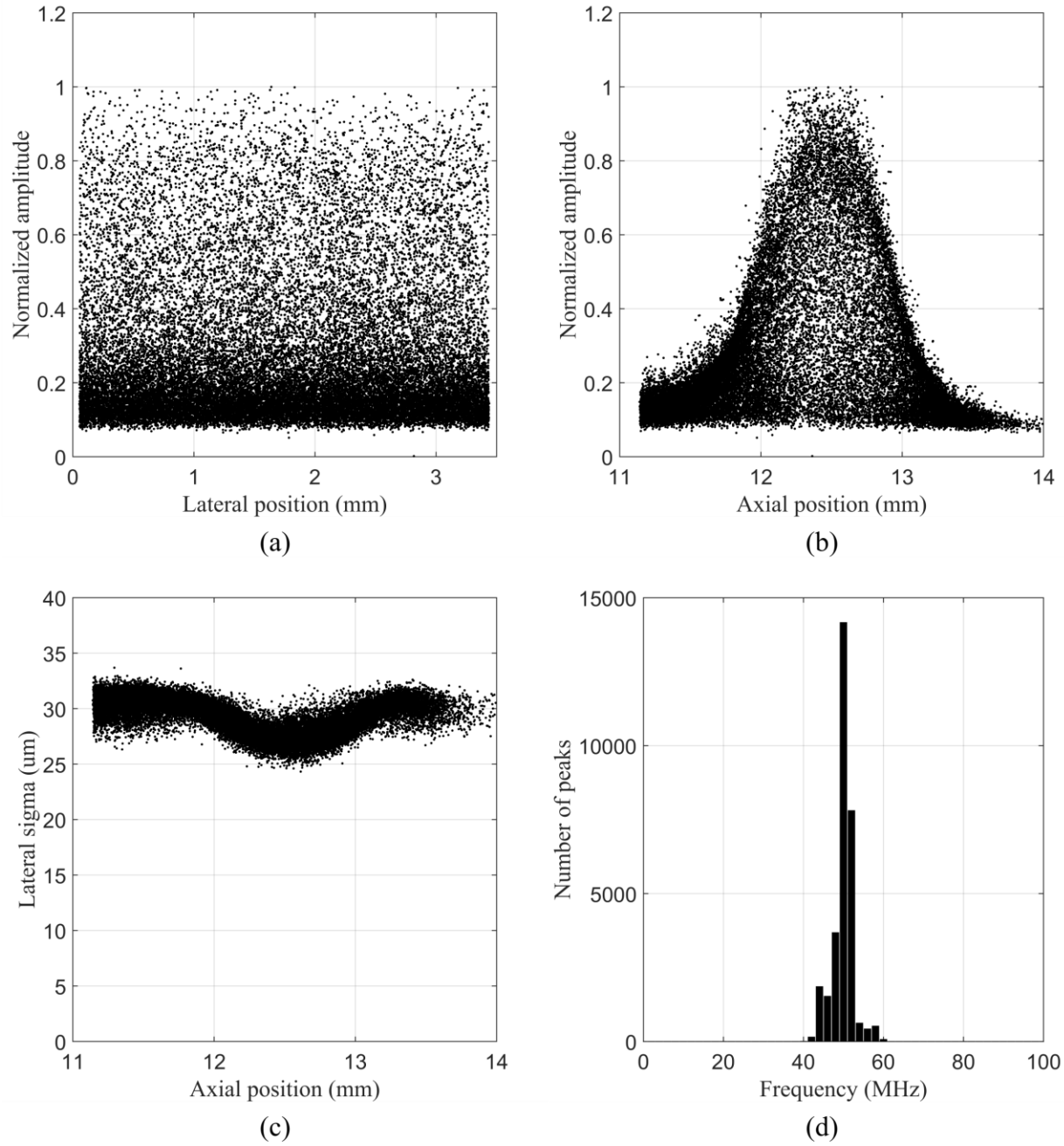

Figure 2-5. Results from running the particle detection algorithm on the entire set of frames. (a) Echo amplitudes vs. lateral positions. (b) Echo amplitudes vs. axial positions. (c) Echo lateral standard deviation vs. axial positions. (d) Histogram of the peak frequency in BSC.

2.3 Effective Slice Thickness Calculation

The effective slice thickness is calculated using the echo amplitudes and the lateral standard deviation measured from the image. The proposed method requires two assumptions: first, the pulse-echo beam profiles in both lateral and elevational directions are modeled as Gaussian; and second, the SSF is assumed to be constant for all echoes at a given axial position, independent of their lateral or elevational position. The effective slice thickness calculation will be first derived for imaging with a mechanically scanned radially-symmetric single element transducer and will be then extended to a more general case including linear arrays.

Figure 2-6 shows a simplified diagram explaining the principle behind the proposed method. Figure 2-6 (a) shows two identical scatterers, A and B, with equal axial positions, but unknown elevational positions. After a long observation time and seeing sufficient number of echoes, assume that A produces the maximum observed amplitude echo and B produces the minimum observed amplitude echo. The resulting idealized B-mode image is shown in Figure 2-6 (b), and the lateral cross-section of the image at the axial location marked by the red dotted-line in Figure 2-6 (b) is shown in Figure 2-6 (c). The echo from A has larger amplitude than that of B, but the SSF is equal and modeled by a Gaussian function with standard deviation of σ_{SSFx}.

Since both scatterers have an equal axial position and the effect of the lateral position on the echo amplitude is negligible, the difference in the echo amplitude of the two scatterers must result from the difference in their elevational position. The acoustic energy is the highest on the imaging plane ($y = 0$) and decreases away from it. Therefore, a scatterer positioned exactly on the imaging plane will produce the highest amplitude echo and those that deviate from it will produce lower amplitude echoes. The exact relationship between the echo amplitude and the elevational position of a scatterer is determined from the effective elevational beam profile.

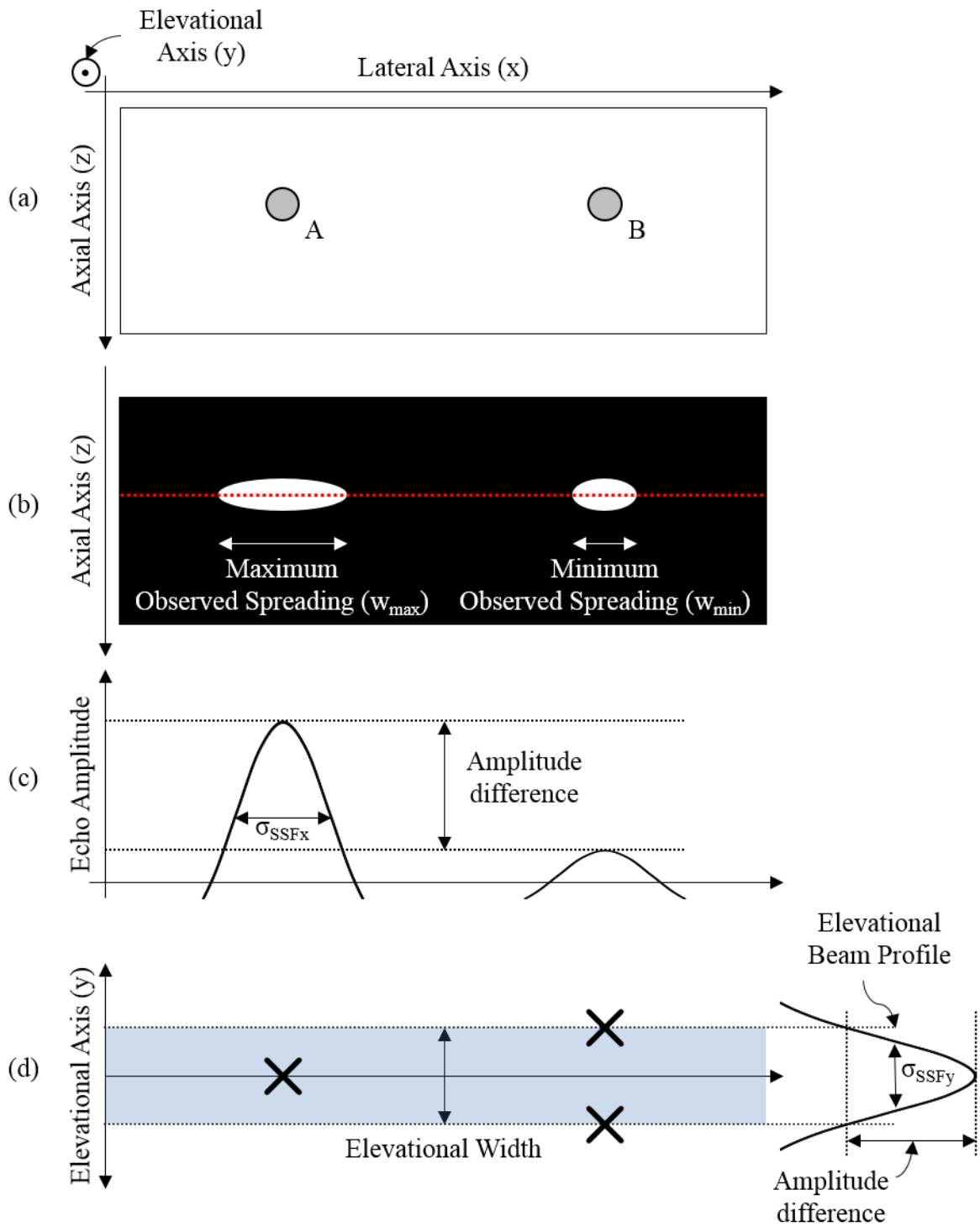

Figure 2-6. Diagram describing the principle behind the proposed method. (a) Position of the two ideal scatterers A and B who have an equal axial positions. (b) Resulting idealized B-mode image from the two scatterers in (a). A produces a maximum echo and B produces a minimum echo. (c) The cross-section of the B-mode image at the position marked by the red dotted line. (d) The possible elevational positions of A and B deduced from the amplitude of their echoes.

In the case where the imaging is performed using a radially-symmetric transducer, which has a circular cross-sectional beam shape, the effective elevational beam profile is identical to the effective lateral beam profile. Therefore, the effective elevational beam profile can also be modeled by σ_{SSFx}. With this information, the elevational position of A and B can be determined. Since A produced the highest observed amplitude echo, it must have been located on the imaging plane ($y = 0$) as shown in Figure 2-6 (d) marked by an X. On the other hand, B had lower amplitude echo than A, which means that it must be deviated from the imaging plane. The exact elevation position of B can be calculated by, first, modeling the effective elevational beam profile P_y as (2) where a_{scatA} is the amplitude of the echo from A.

$$P_y(y,z) = a_{scatA} \exp\left(-\frac{y^2}{2\sigma_{SSFx}^2(z)}\right) \tag{2}$$

The amplitude of the Gaussian function is a_{scatA} since an echo amplitude of a_{scatA} is produced when a scatterer is positioned at $y = 0$. The elevational position of B is calculated by finding y when P_y is equal to a_{scatB} as shown in (3) and (4). There are two possible positions, with B either in front of or behind the imaging plane. The two positions are marked by Xs in Figure 2-6 (d).

$$a_{scatB} = a_{scatA} \exp\left(-\frac{{y_{scatB}}^2}{2\sigma_{SSFx}^2(z)}\right) \tag{3}$$

$$y_{scatB} = \pm\sigma_{SSFx}(z)\sqrt{2\ln\left(\frac{a_{scatA}}{a_{scatB}}\right)} \tag{4}$$

Additionally, since B produced the lowest observed amplitude echo, it must have deviated the farthest away from the imaging plane among all observed echoes. If this were not true and there were another scatterer farther away from the imaging plane, that scatterer had to have produced a lower amplitude echo, in which case, the echo produced by B would not be the

lowest amplitude. Therefore, the two possible locations calculated by (4) also define the effective slice thickness $t_{slice}(z)$ of the image at the given axial position as shown in (5) where $A_{max}(z)$ is substituted for a_{scatA} and $A_{min}(z)$ for and a_{scatB}. $A_{max}(z)$ and $A_{min}(z)$ refer to the maximum and minimum observed echo amplitude at a given axial position z, respectively.

$$t_{slice}\,(z) = 2\sigma_{SSFx}(z)\sqrt{2\ln\left(\frac{A_{max}(z)}{A_{min}(z)}\right)} \tag{5}$$

This is an important result because it enables the estimation of the effective slice thickness at a given axial position by using just the observed maximum and minimum echo amplitudes and the standard deviation of the spreading at the given axial position, which are parameters readily available from the B-mode images of the sample. Once the effective slice thickness is found as a function of the axial position, the image volume can be easily calculated, which can then be used to calculate the absolute concentration.

2.4 Effective Slice Thickness Calculation – Generalization

In a more general case, such as imaging with a linear array, the transducer is not radially-symmetric and the cross-sectional beam shape is not a circle but rather is an ellipse. This means that the pulse-echo beam profile in the lateral direction is different than in the elevational direction. To accommodate this, (5) can be modified to (6), where R_{el} is defined as in (7).

$$t_{slice}\,(z) = 2R_{el}(z)\sigma_{SSFx}(z)\sqrt{2\ln\left(\frac{A_{max}(z)}{A_{min}(z)}\right)} \tag{6}$$

$$R_{el}(z) = \frac{\sigma_{SSFy}(z)}{\sigma_{SSFx}(z)} \tag{7}$$

The parameter R_{el} is the ratio between the scatterer spreading in the elevational direction and lateral direction. While the lateral SSF can be measured from the image, the elevational SSF

cannot typically be directly measured as imaging would have to be performed while scanning in the elevational direction, which is not routinely or easily done. Instead, in the proposed method, R_{el} is estimated as in (8) by measuring the ratio between the elevational beam profile and the lateral beam profile using either simulation or measurement of the beam profile. This is based on the assumption that the elevational beam profile is affected by a physical scatterer in the same fashion as the lateral beam profile. Therefore, while both lateral and elevational SSF depend on the type of sample being imaged, the ratio of the two remains independent of the scatterer. It is important to note that the estimation of R_e and therefore the elevational SSF only requires characterizing the imaging system, but not the sample.

$$R_{el} = \frac{\sigma_{SSFy}(z)}{\sigma_{SSFx}(z)} \cong \frac{\sigma_y(z)}{\sigma_x(z)} \tag{8}$$

For the experiments performed in this work using the Vevo 2100, the pulse-echo beam profile is simulated with one transmit focal zone centered at 7 mm. The simulation is performed with Field II [41], [42]. The simulated beam profiles are not provided due to the proprietary information used in the simulation. However, the cross-sectional beam profile is an ellipse, as expected, with an R_{el} value of 1.2.

2.5 Algorithm Implementation

A MATLAB based algorithm for effective slice thickness and absolute concentration estimation is implemented as follows. Since echo characteristics have a strong dependence on the axial position of the scatterers, the detection results are first sliced along the axial direction (depth). Figure 2-7 (a) shows the echo amplitude vs. axial position, with the different colors representing the different axial slices. The length of the axial slices l_{zslice} and the amount of overlap between the adjacent slices $l_{zsliceov}$ are chosen depending on the characteristics of the transducer, such as

the frequency and the f-number. The overlap is used to ensure the smoothness of the parameter. For the example in Figure 2-7, axial slice length l_{zslice} of 100 μm and overlap length $l_{zsliceov}$ of 80 μm are used. Figure 2-7 (b) shows the lateral standard deviation vs. axial position for different axial slices.

For each axial slice, the number of detected echoes $N_{slice}(z)$ are first determined. From the echoes in a given axial slice, the maximum and minimum observed amplitudes, $A_{max}(z)$ and $A_{min}(z)$, and the lateral standard deviation $\sigma_{SSFx}(z)$ are determined. $A_{max}(z)$ and $A_{min}(z)$ are determined by taking the 95% and the 5% echo amplitudes, respectively, instead of taking the actual maximum and minimum amplitude. This is done in order to reduce the susceptibility to outliers, which can drastically affect the resulting effective slice thickness. The value of $\sigma_{SSFx}(z)$ is determined by averaging the observed lateral sigma at a given axial position z. Using these values, the effective slice thickness for the given axial slice is calculated according to (6). Since the image width W and the slice window length l_{zslice} are now defined, the slice volume $V_{slice}(z)$ and slice concentration $C_{slice}(z)$ can be calculated as in (9) and (10).

$$V_{slice}(z) = W \times l_{zslice} \times t_{slice}(z) \tag{9}$$

$$C_{slice}(z) = \frac{N_{slice}(z)}{V_{slice}(z)} \tag{10}$$

The calculation is repeated for all axial slices. Figure 2-7 (c) shows a plot of number of detected echoes as a function of axial position, which is acquired by counting the total number of detected echoes in the corresponding axial slice. Figure 2-7 (d) shows a plot of effective slice thickness as a function of axial position. The plot shows that the effective slice thickness reaches maximum around the focal point of the transducer and decreases moving away from it. This may seem counter-intuitive at first since beam width is thought to be the narrowest at the focus of the

transducer and one might expect that so should the slice thickness. This is true when -6 dB beam width is considered where the width is calculated relative to the peak amplitude at that axial position: since the beam is most converged at the focus of the transducer, the -6 dB beam width is the narrowest at the focus. For the effective slice thickness, however, the beam width is measured at an absolute amplitude determined by the dynamic range of the image and the detection algorithm, and should be appropriately constant for all axial positions. Since the intensity of the beam is the highest at the focus, a larger portion of the beam exceeds the reference amplitude leading to a larger effective beam width. Away from the focus, even though the beam spreads more, the intensity is lower, resulting in a smaller portion of the beam exceeding the reference amplitude, which leads to a smaller effective thickness.

Figure 2-7 (e) shows the particle concentration for each axial slice. Ideally, the slice concentration should remain constant over the entire range since the concentration should be uniform throughout the sample. However, the slice concentration calculation varies depending on the axial position, reaching a significantly higher concentration in the axial slices that are farther away from the focus. This is due to noisy or faulty detections in those slices arising from low beam intensity. Since the beam is diverged, the echoes are weaker but wider, which leads to over-counting of the echoes. However, the amplitude of the echoes are still measured correctly and the effective slice thickness is accurately estimated. Since the volume is estimated correctly, but the number of particles is overestimated, this leads to overestimating the concentration in low intensity axial slices. For this reason, the final concentration is calculated as an average of $C_{slice}(z)$ using only the axial slices within the -6 dB effective depth of focus (DOF) as determined from the amplitude vs. axial position plot in Figure 2-7 (a). The term effective is used to emphasize the fact that DOF in this context refers to a parameter that is not only dependent on

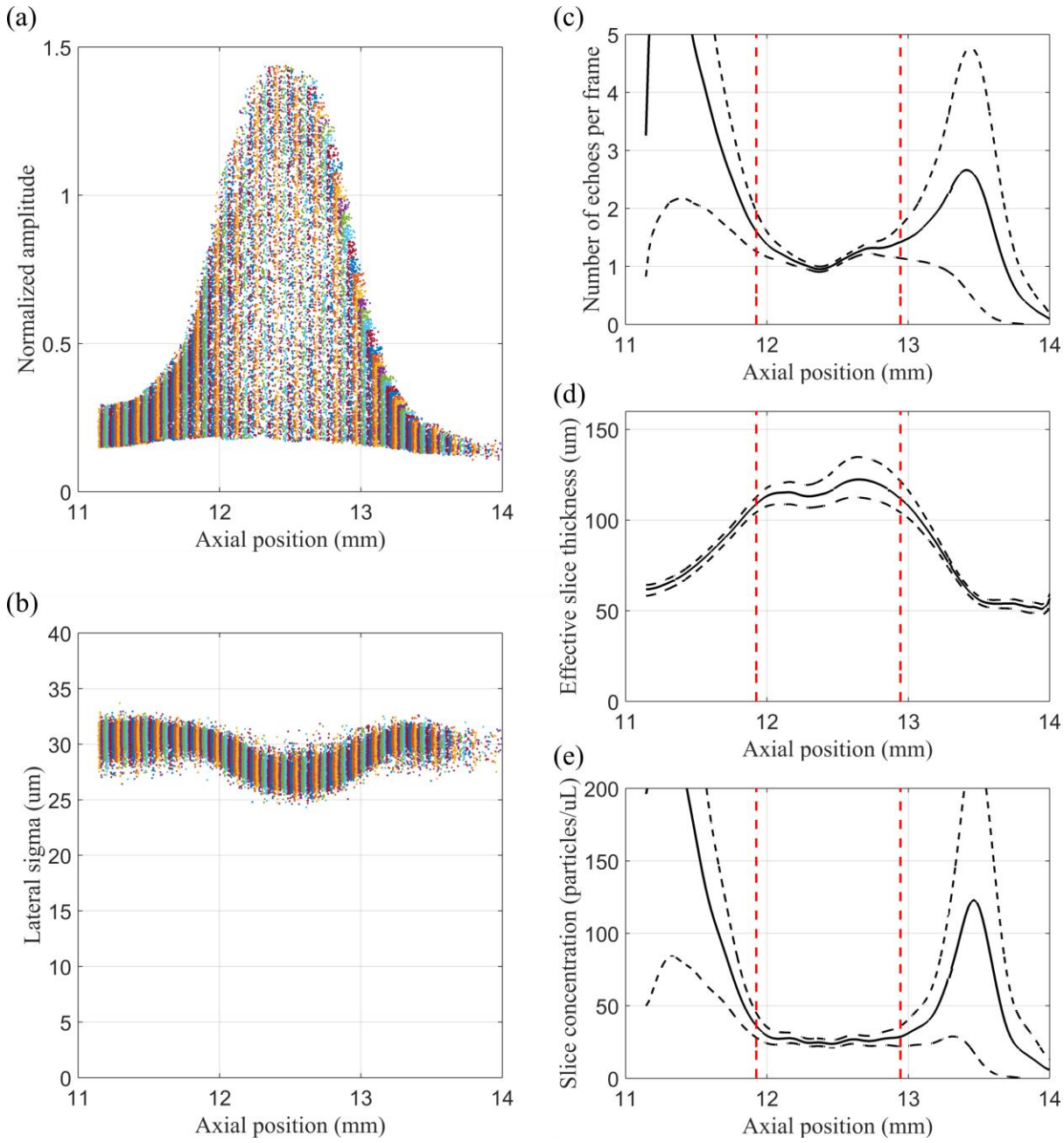

Figure 2-7. Results from the particle detection sliced along the axial direction: (a) echo amplitudes vs. axial positions and (b) echo lateral standard deviation vs. axial positions. Calculated parameters: (c) number of detected echoes per frame vs. axial slices, (d) effective slice thickness vs. axial slices, and (e) slice concentration vs. axial slices. The black dotted lines in the plots (c) – (e) represent the estimated measurement uncertainty.

the imaging system but also on the sample type. The effective DOF refers to the one that would be measured from the pulse-echo beam profile produced by the given particle types present in the sample, which is why it is determined from the measured data and not the transducer specification. Because the effective DOF is particle type dependent, the axial region used for the final concentration measurement will vary for each particle type, even when they are in the same sample as is the case for a polydispersed sample, which will be shown in Section 4.3. The region used in the calculation for this sample is shown by the two red dotted lines in Figure 2-7 (c) and (d).

2.6 Estimation of Measurement Uncertainty

There are uncertainties associated with calculation of each parameter and it is important to evaluate their contribution to the final concentration calculation.

In Figure 2-7 (c), the black dotted lines show the estimated error bounds in acquiring the particle count for each axial slice. The error is mainly due to two causes: first, the error in particle detection and second, the sampling nature of the measurement process. As discussed previously, the particle detection error increases for echoes that are farther away from the focal point of the transducer because the beam diverges and the intensity decreases leading to lower echo amplitude. Therefore, the error in particle detection is a strong function of the echo amplitude. While it is ideal if the particle detection algorithm could be characterized so that the detection error as a function of the echo amplitude can be quantified, it is not straightforward how this can be achieved. Instead, the detection error due to echo amplitude, $Err_{amp}(z)$, is estimated empirically using (11), where $A_{max}(z)$ is the maximum observed echo amplitude at axial position z, α is the proportionality constant, and β is a term that sets how strongly the error is affected by the echo amplitude. Both α and β are set empirically from the measured data. First,

α is set such that the detection error is minimized at the axial position where the maximum echo amplitude occurs. The value of α is dependent on the absolute value of the echo amplitudes and thus is different for each experiment. Second, β is set such that the detection error is low within the DOF. For this work, β is set to 0.2.

$$Err_{amp}(z) = \alpha\left(\frac{1}{A_{max}(z)}\right)^{\beta} \tag{11}$$

The error in particle count due to the sampling nature of the measurement is estimated by assuming that the particle count at a given axial position follows a Poisson distribution. This results from the assumption that the particles in the sample are uniformly distributed in the three-dimensional space and each measurement samples a finite volume of that space. Since the standard deviation of a Poisson distributed random variable is the square root of the mean of that random variable, the standard deviation of the particle count can be estimated by (12).

$$\sigma_{sampling}(z) = \sqrt{N_{slice}(z)} \tag{12}$$

Since each measurement consists of one sample, the standard error $SE_{sampling}(z)$ is also equal to $\sigma_{sampling}(z)$. Combining the two components, the total particle detection error can be estimated by (13), where 1.645 is used to calculate the 90% confidence interval.

$$Err_{detection}(z) = Err_{amp}(z) + 1.645 \times SE_{sampling}(z) \tag{13}$$

As expected, the resulting particle detection error shown in Figure 2-7 (c) increases drastically for axial slices that are farther away from the focal point of the transducer. While this is only an estimation, it provides useful insight into the underlying behavior and also enables the estimation of the contribution of the particle detection error to the final concentration measurement.

Another important source of error is in the estimation of the effective slice thickness. The black dotted lines in Figure 2-7 (d) represent the 90% confidence interval for the effective slice thickness estimation, which captures the uncertainty due to the variation observed in the lateral sigma measurement. As discussed before, the method assumes that the scatterer spreading is independent of the elevational position. While the range of lateral sigma values at a given axial position is relatively small, they still vary. This variation directly contributes to the error in effective slice thickness estimation, and therefore it is important to evaluate its contribution to the error in the final concentration calculation. The confidence interval is calculated from the top 95% and the bottom 5% value of lateral sigma in Figure 2-7 (b).

The resulting measurement error is shown in Figure 2-7 (e). The upper and lower bounds represents the estimation of the 90% confidence interval and are calculated from the error associated with determining the number of particles and the effective slice thickness. As expected, the measurement error is low around the DOF, which is noted to be the region between the two red dotted lines, but increases outside of this region.

2.7 Summary

A summary of the proposed method is shown in Figure 2-8. Given RF data acquired with an imaging system, envelope detection is performed and the particle detection algorithm is run. The detection algorithm measures the amplitude, the axial and lateral positions, the lateral standard deviation, and the BSC of each echo. Using the BSC measurement, the echoes are clustered into different particle types such that the concentration measurement can be performed for each type. The detection data is sliced along the axial direction according to the slice window length and window overlap length parameters. The effective slice thickness is calculated from the maximum and minimum observed echo amplitudes, and the standard deviation of the SSF according to (6),

where R_e represents the ratio between the elevational and the lateral SSF. In the case of a radially-symmetric transducer such as a disk transducer, R_e is equal to 1. In a non-radially-symmetric case, R_e is estimated through either prior simulation or measurement of the beam profile. Using the calculated effective slice thickness, the slice volumes and concentration are calculated. The overall sample concentration is calculated by averaging the calculated concentration in each of the slices in the depth of field of the transducer.

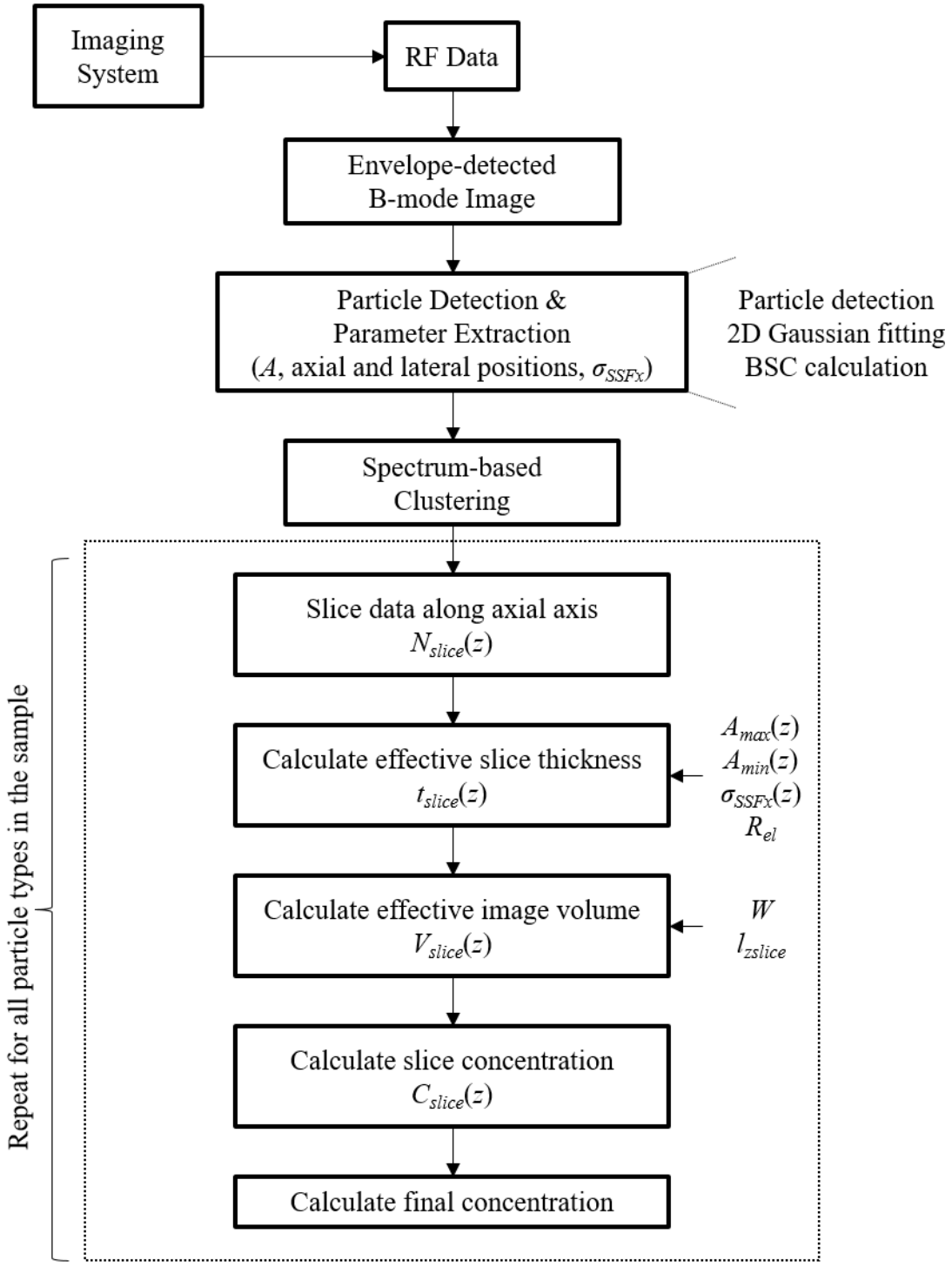

Figure 2-8. Summary of the proposed method. The sample is imaged with an imaging system. The particle detection algorithm is run on the data from the measurement, which provides the location, amplitude, SSF, and BSC of each detected echo. Using the BSC, the particles are classified into different types, and concentration is calculated for each particle type.

3. Experimental Work

In this chapter, a description of the experimental work performed to demonstrate the proposed method is provided. The imaging systems and the samples used in the experiments are discussed in Sections 3.1 and 3.2, respectively. An overview of the six experiments performed is provided in Section 3.3. A method for providing the reference measurements and the statistical analyses are discussed in Sections 3.4 and 3.5, respectively.

3.1 Imaging systems

High frequency B-mode images are acquired with two imaging systems: a mechanically scanned single element transducer and a VisualSonics Vevo 2100. The mechanically scanned single element transducer imaging system (MS) is shown in Figure 3-1 (a). The system consists of a high frequency ultrasound transducer, a high frequency pulser-receiver (P/R), a digitizer, and a 3-axis scanning stage driven with stepper motors. Figure 3-1 (b) shows the 75 MHz spherically focused single element disk transducer (V3320, Olympus NDT, Waltham, MA). The diameter of the transducer is 6.35 mm and the focal distance is 12.7 mm (f-number of 2). The -6 dB bandwidth of the transducer is 81%. There is a 20 μs silica delay line attached to the front of the transducer because there is no matching layer. A double shielded cable (BCM-74-x DS, Olympus NDT, Waltham, MA) is used to connect to the transducer in order to reduce noise coupling in from other instruments. The pulse-echo imaging is performed with a high frequency square wave-based pulser-receiver (P/R) (UT340, UTEX Scientific Instruments, Ontario, Canada). The amplitude of the excitation pulse is 250 V and the width is 10 ns, which is chosen to maximize the amplitude of the echo from the sample. The low pass and high pass filter in the P/R is turned off. Rather, filtering is performed digitally during post processing. The RF signal from the P/R is digitized with a PicoScope 5444b oscilloscope (Pico Technology,

Cambridgeshire, United Kingdom) shown in Figure 3-1 (c). The PicoScope 5444b is a USB-based digitizer that has an on-board memory of 512 Mbyte and is capable of sampling rates up to 2 Gsps. For this setup, the sampling rate is set to 500 Msps at 12-bit resolution.

Linear scanning is performed with a 3-axis scanning stage driven with stepper motors. The stage is built from ShapeOko 2, a low-cost, open source Computer Numerical Control (CNC) mill [43] shown in Figure 3-1 (d). The stage has four stepper motors (NEMA 23), which are driven with low-noise linear stepper motor drivers (CLD, Phytron Inc., Williston, VT) shown in Figure 3-1 (e) to minimize the motors and the drivers from emanating electrical noise, which can be detrimental to the signal-to-noise ratio (SNR) of the ultrasound signal. The motor on the scanning direction is microstepped at 1/10 ratio to achieve a lateral resolution of 10 μm. The stage control and the trigger signal for the P/R and the digitizer generation are done with an FPGA board (XEM3010-1000, Opal Kelly, Portland, OR) [44] that is connected to the computer and interfaced through MATLAB (MathWorks, Natick, MA). An image is constructed by stacking 350 scan lines spaced by 10 μm, resulting in an image width of 3.5 mm. Images are acquired on both scanning directions. RF data is acquired and processed using MATLAB.

The VisualSonics Vevo 2100 (Vevo) (VisualSonics, Toronto, Canada), a high frequency ultrasound imaging system using linear arrays, is shown in Figure 3-2 (a). The Vevo is currently the only commercially available array-based high frequency imaging system and is used widely for animal studies in life science and clinical research laboratories [45], [46]. It is capable of imaging up to center frequency of 50 MHz with solid-state linear array probes. For this work, an MS550D probe shown in Figure 3-2 (b) is used that has a center frequency of 40 MHz with -6 dB bandwidth of 82.5% spanning 22 to 55 MHz and a geometric focus at 7 mm. The maximum image depth and width of MS550D are 14.1 mm and 15.0 mm, respectively. The

resolution in the axial and lateral direction measured at the geometric focus is 40 μm and 90 μm, respectively. Each scan line is spaced by 36 μm.

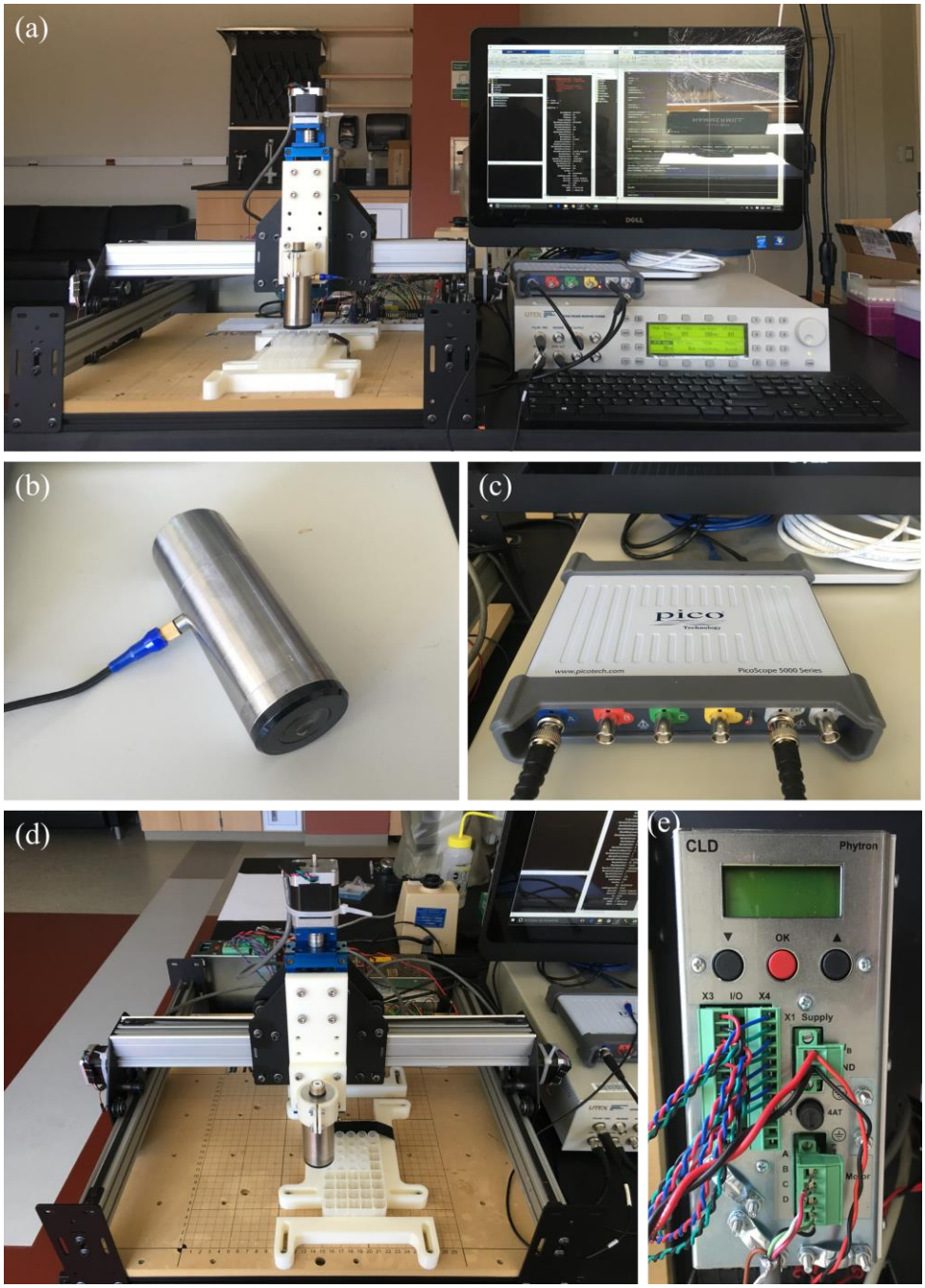

Figure 3-1. (a) Mechanically scanned single element transducer imaging system. (b) V3320, a 75 MHz spherically focused single element transducer. (c) PicoSope 5444b used to digitize the output signal from the P/R. (d) 3-axis scanning stage built from an open source CNC mill kit. (e) CLD, a low-noise linear stepper motor driver.

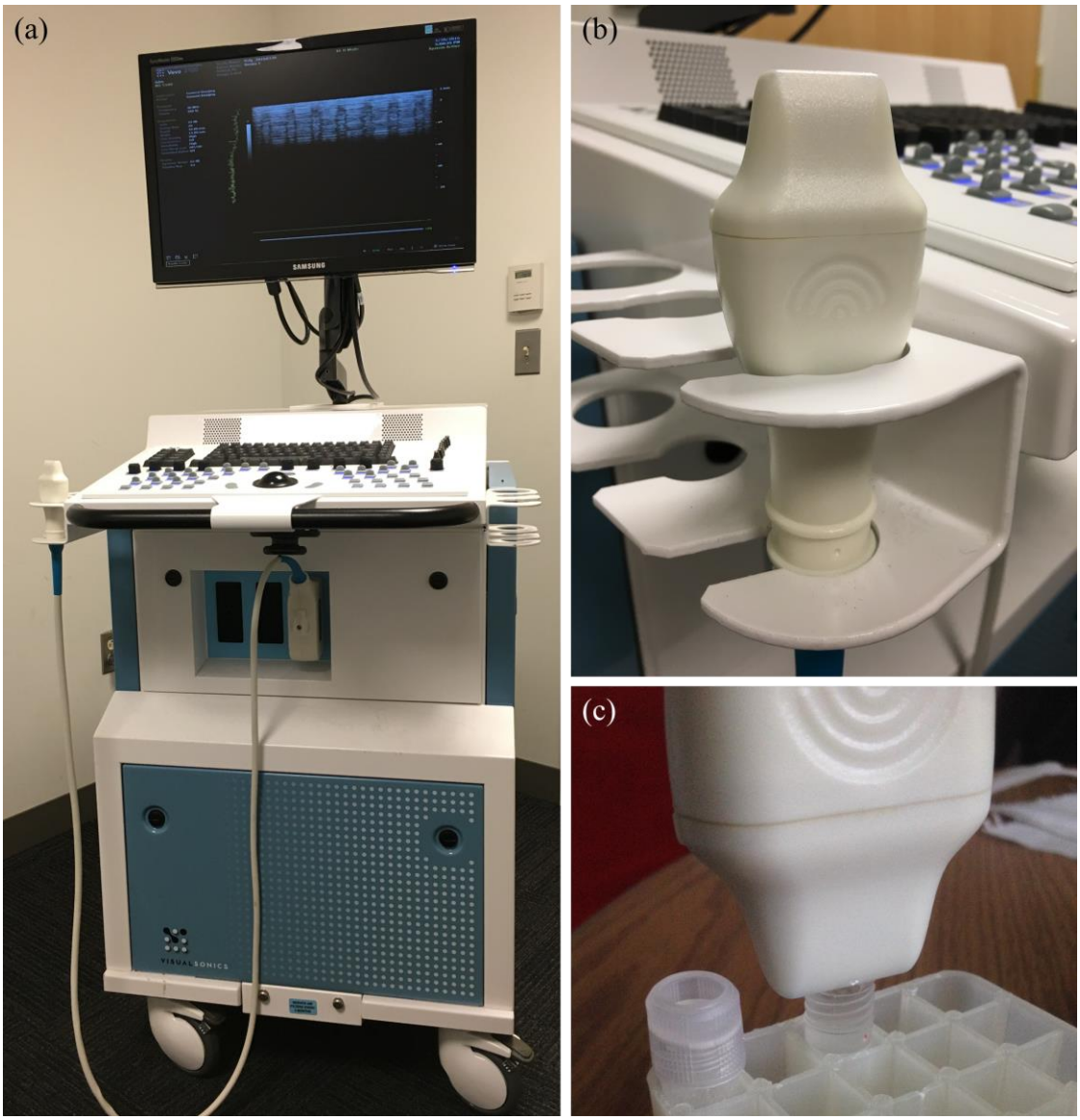

Figure 3-2. (a) VisualSonics Vevo 2100 high frequency array-based imaging system.
(b) MS550D, a solid-state linear array probe with center frequency of 40 MHz. (c) Imaging setup with the transducer in direct contact with the sample. The sample is contained in a polypropylene cryogenic vial.

3.2 Samples

Both non-biological and biological samples are used to demonstrate the proposed method. The non-biological samples consist of microspheres suspended in distilled water. Three different size and type combinations of microspheres are used: 10 μm and 15 μm polystyrene (PS) (Sigma-Aldrich, Natick, MA), and 10 μm silica (Corpuscular Inc., Cold Spring, New York) [47]. The particle sizes are chosen to emulate the size of human WBC.

The biological samples consist of human peripheral blood mononuclear cells (PBMC) cultured with 50 IU/mL of rHu-IL2 for six to eight days before the measurement. The culture condition is set to ensure that 99% of the cells are T cells, which are a type of WBC. More specifically, these T cells (named after the thymus, the specialized lymphoid organ in which they mature) are lymphocytes that play an important role in cell-mediated immunity. The T cells used in this work are around 10 – 15 μm in diameter. The concentration measurements are made with cells suspended in PBS.

For the non-biological samples, preparation and handling are done in a disposable borosilicate glass culture tube shown in Figure 3-3 (a). This is chosen to minimize the microspheres from adhering to the wall of the vial. The microspheres showed too much adherence to the polystyrene and polypropylene centrifuge tubes widely used in life science laboratories, causing the concentration to decrease over time. This was especially severe for high concentration samples. For the biological samples, polypropylene centrifuge tubes are used, which is the recommended vial for the cell type.

For both non-biological and biological samples, the actual measurement is made in a 2 mL polypropylene round bottom cryogenic vial shown in Figure 3-3 (b). Polypropylene is chosen

despite the fact that microspheres adhere to the surface because glass tubes of the required size were not available. In order to reduce adherence, the measurement vial is first rinsed with a medium concentration sample to coat the surface. This improves the stability of the concentration of the actual sample being measured.

For the non-biological samples, the transducer is in direct contact with the sample in order to maximize the acoustic coupling as shown in Figure 3-2 (d). For the biological samples, a similar setup is used but the probe is covered with an ultrasound probe cover to avoid contamination.

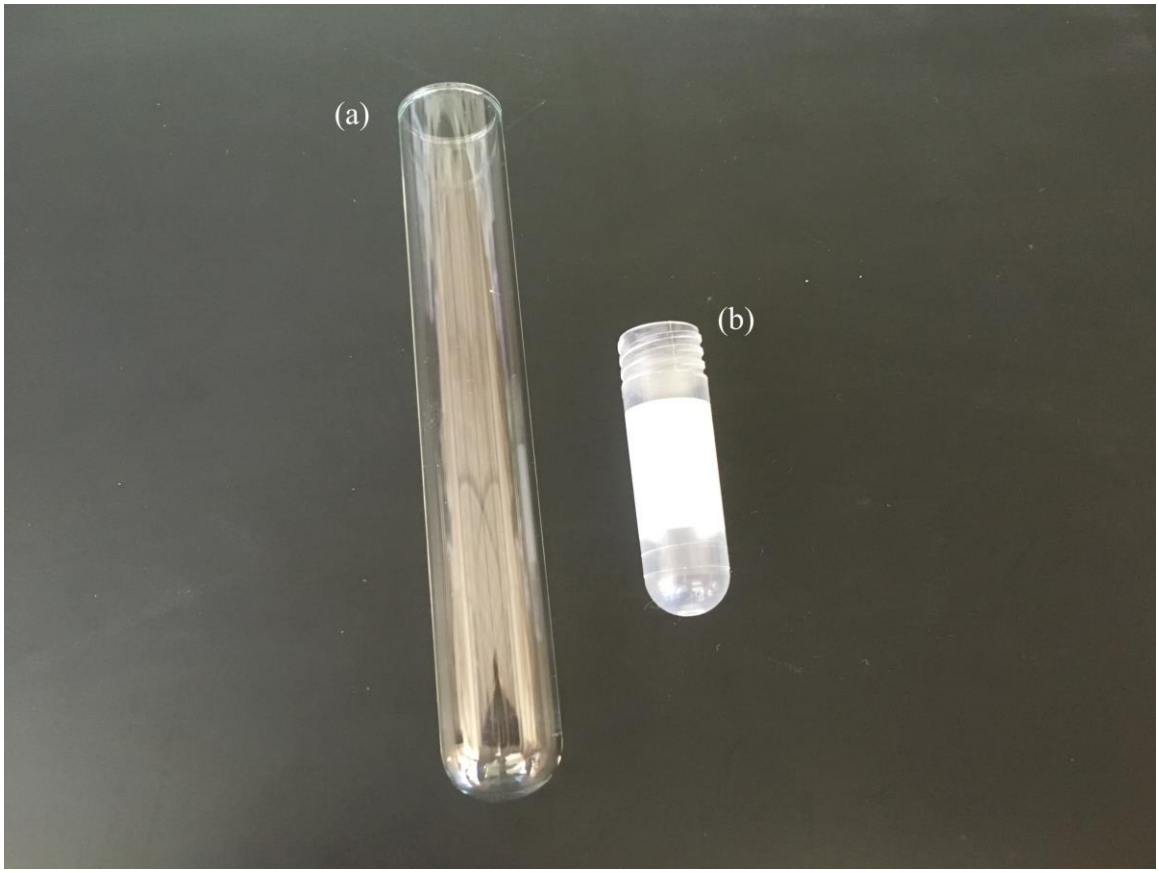

Figure 3-3. Vials used for manipulating samples. (a) Disposable borosilicate glass culture tube, 16 × 100 mm, 14 mL. (b) Polypropylene round bottom cryogenic vial, 2 mL.

3.3 Overview of the Experiments

In order to demonstrate the proposed method, six experiments are performed using different types of samples consisting of both non-biological and biological particles. The key parameters of the experiments are summarized in Table 3-1.

Table 3-1. Experiments performed to demonstrate the proposed method.

Experiment	Imaging System	Particle Type	Suspension Fluid
1	MS	10 μm PS	dH_2O
2	Vevo	10 μm PS	dH_2O
3	MS	15 μm PS	dH_2O
4	MS	10 μm silica	dH_2O
5	MS	10 μm PS + 15 μm PS	dH_2O
6	Vevo	T cells	PBS

∗ MS: mechanically scanned single element transducer imaging system
∗ Vevo: VisualSonics Vevo 2100 imaging system
∗ dH2O: distilled water
∗ PBS: phosphate-buffered solution

In experiments 1 through 4, monodispersed samples of non-biological particles of different types are measured using the MS and Vevo to demonstrate that the proposed method works for different particle types as well as with different imaging systems. In experiment 5, polydispersed samples consisting of 10 μm and 15 μm PS microspheres are measured to demonstrate the ability to distinguish and cluster particle types using BSC and the type-dependent concentration measurement. To demonstrate that the proposed method can work with non-ideal biological samples, T cells suspended in PBS are measured in experiment 6.

3.4 Reference Measurement

The reference concentration measurements are performed using disposable Fuchs-Rosenthal (FR) hemocytometers (DHC-F01, INCYTO, South Korea) [48] shown in Figure 3-4 (a). There are two counting chambers per slide, marked by A and B in the photograph. A microscope view of the FR is shown in Figure 3-4 (b). A 1 mm × 1mm grid is shown in the photograph. The

sample shown in the figure is a 10 μm PS microsphere sample with concentration of 450 particles/μL. The FR hemocytometer can analyze up to 3.2 μL of fluid sample (4 mm × 4 mm × 0.2 mm) per chamber and is used to analyze samples with low particle concentration such as CSF. It is chosen for this work since the target particle concentration range is low (< 200 particles/μL). To make a measurement, the sample is first well-mixed to re-suspend the particles and 20 μL of the sample is pipetted into the chamber. After waiting a few minutes to ensure that the sample has settled, particles are counted under an optical microscope. Each sample is measured four times, consistent with the standards used in clinical laboratories for CSF cell counts [6], [49]. The concentration is calculated by averaging the four measurements.

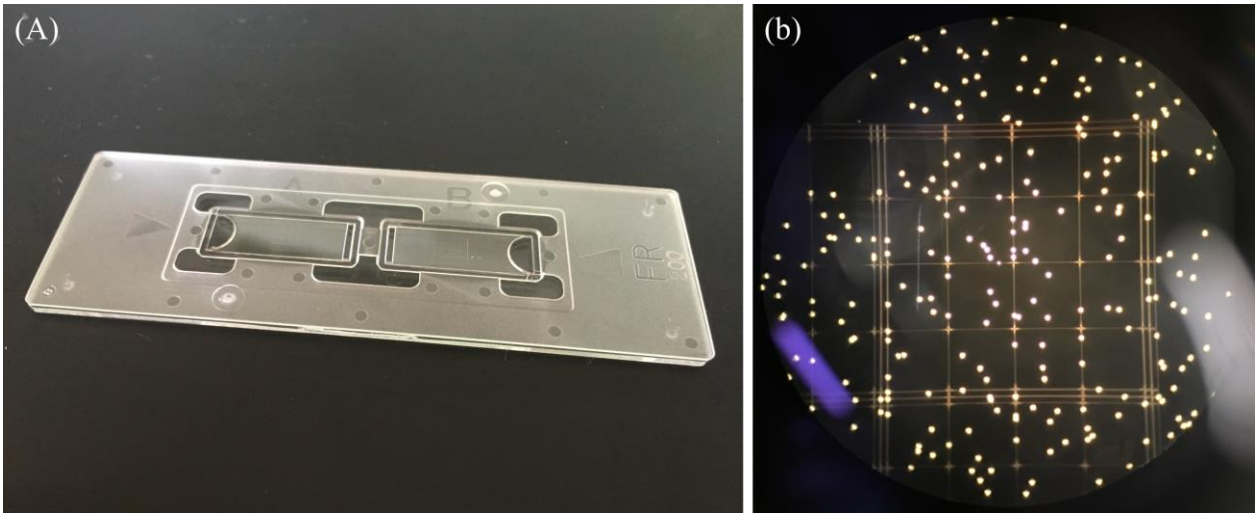

Figure 3-4. (a) DHC-F01 disposable Fuchs-Rosenthal hemocytometer. There are two chambers of 3.2 μL per slide. 20 μL of sample is pipetted into the chamber and examined under an optical microscope after some time to let the particles settle down. (b) Photograph of microscope view of a 1 mm^2 region of the DHC-F01 hemocytometer with 10 μm PS microsphere sample (450 particles/μL).

3.5 Statistical Analysis

Since the goal of this work is to compare the proposed method to the hemocytometer-based methods, it is important to accurately estimate the measurement error associated with both. A straightforward way of estimating the error for the hemocytometer is to calculate the standard

error from the four measurements. While this works and is often done, it is not an accurate estimation of the best achievable error of the method because it is strongly affected by the user-dependent variability, especially when the user is not a trained technician [6], [8]. Therefore, rather than using the statistics of the measurements, other established methods of calculating achievable error is used to estimate the error.

There are two established methods of estimating the measurement error associated with a hemocytometer measurements. The first method is based on the fact that counts made from a well-mixed sample follows the Poisson distribution. With this assumption, the standard deviation of the counts can be estimated by the square root of the mean. The second method is empirical and based on the typical error achieved by trained technicians. It has been shown that measurement error as low as 10 to 15% can be achieved. This value applies to cases where the concentration is relatively high such that there are sufficiently large counts. For low concentrations, the error increases [50]–[52].

In this work, the two methods are combined to estimate the error associated with the hemocytometer measurements. For lower concentration samples where the count is below 32 per 3.2uL, which corresponds to 10 particle/μL, the first method is used, where the standard deviation is estimated by the square root of the mean count. The error bars for this range of concentrations denote the 95% confidence interval. For higher concentration samples, the second method of 15% error is applied.

For ultrasound based concentration measurement, the error is estimated by using the bootstrap method. Each measurement consists of 500 frames in the case of MS and 250 frames in

the case of Vevo. Bootstrap is performed by resampling the frames 1,000 times with replacement. The error bars for the proposed method depict the 95% confidence interval.

4. Results

In this chapter, the results of the six experiments described in Chapter 3 are provided. In Section 4.1, the results from experiments 1 and 2, in which 10 μm PS microsphere samples are measured with MS and the Vevo, respectively, are presented. In Section 4.2, the results from experiments 3 and 4, in which 15 μm PS microsphere and 10 μm silica microsphere samples are measured with MS, respectively, are presented. The results from experiment 5, where polydispersed samples of 10 μm and 15 μm PS microsphere samples are measured with MS, and experiment 6, where human T cells samples are measured with the Vevo, are discussed in Sections 4.3 and 4.4, respectively.

4.1 Experiments 1 and 2

In experiments 1 and 2, ten samples with different concentrations of 10 μm PS microspheres are measured with MS and the Vevo, respectively. The purpose of these experiments is to demonstrate that the proposed method can accommodate images acquired with a radially-symmetric transducer as well as a linear array as described in Section 2.4. The same set of samples are measured with both imaging systems within a few hours of each other in order to ensure that the concentration of the samples does not change due to the particles settling or adhering to the wall of the vial. The concentrations range from 0.5 to 200 particles/μL.

4.1.1 Experiment 1

The B-mode images acquired with MS are shown in Figure 4-1. The concentrations of the four samples are (a) 5 particles/μL, (b) 10 particles/μL, (c) 20 particles/μL, and (d) 50 particles/μL. As can be seen in the figure, there is an increase in the number of echoes in the image as the sample concentration increases. Due to the relatively low concentration, each echo is far apart from all others, allowing individual echoes to be distinguished. The result from the

particle detection is shown in Figure 4-2. The particle detection results show the same trend as the example measurement presented in Chapter 2. One notable difference is the echo amplitude vs. axial position shown in Figure 4-2 (b). While the overall trend of maximum amplitude echoes occurring around the focal point of the transducers is the same, the peak around the focal point is narrower in this case compared to Figure 2-5 (b). This is due to the difference in the particle size. Since the particle size is smaller in this case, the frequencies involved in backscattering are higher and the wavelengths smaller. This means that the DOF also becomes smaller, which results in a narrower peak. Another feature to note is the peak frequency in the BSC shown in Figure 4-2 (d), which occurs around 70 MHz. This is in agreement with the Faran model for 10 μm PS microspheres.

The axial slices as well as the number of detected echoes, calculated effective slice thickness, and slice concentration are shown in Figure 4-3. These also follow the same trend as the example in Chapter 2. However, it is worth noting the slice concentration in Figure 4-3 (e). The region that is used for final calculations indicated by the two red dotted lines is much narrower than the region used in Figure 2-7 (e). This is again due to the smaller particle size, which leads to a smaller DOF.

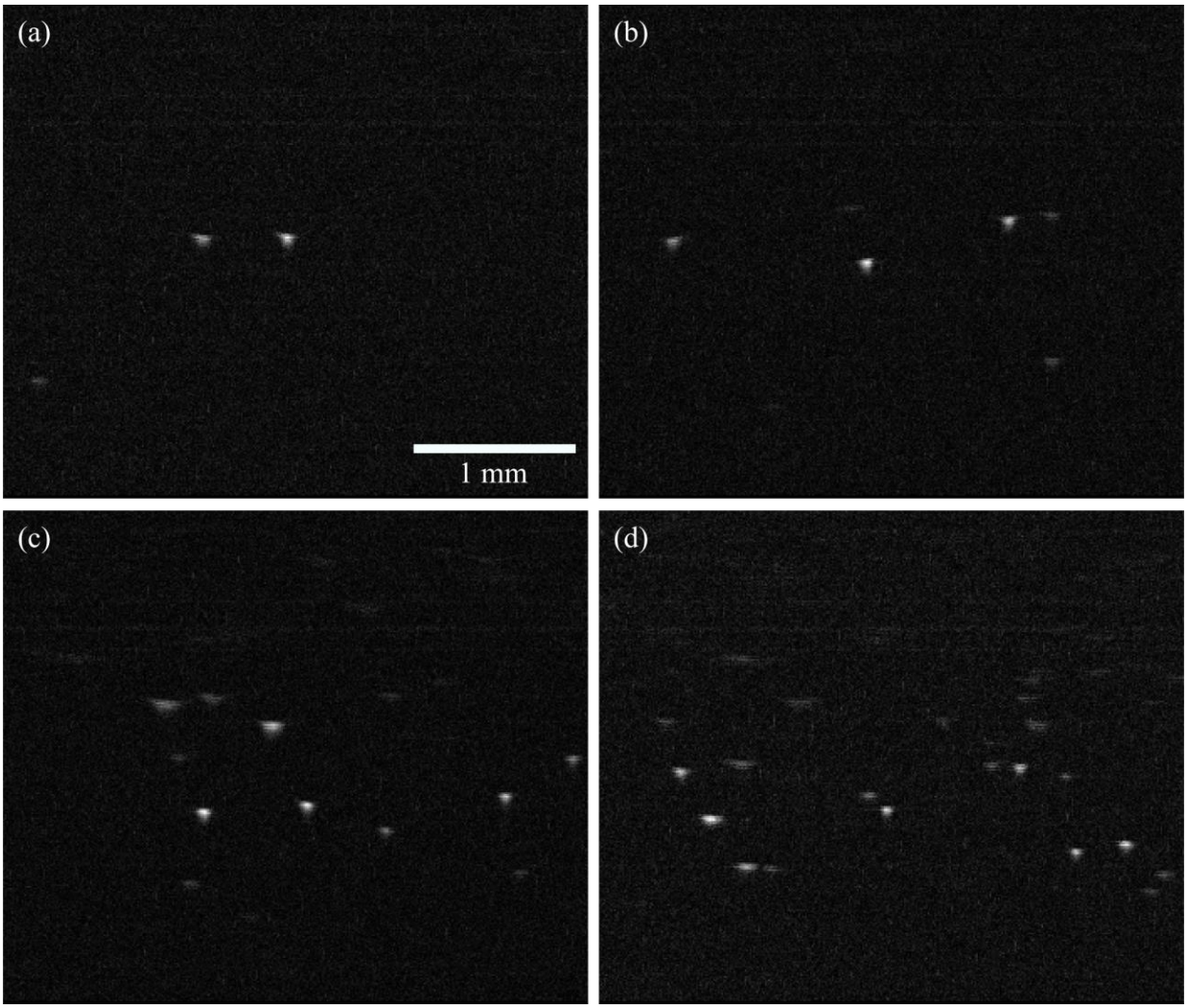

Figure 4-1. B-mode images of 10 μm PS microspheres suspended in distilled water acquired with MS (experiment 1). Four concentrations are shown: (a) sample 4, 5 particles/μL, (b) sample 5, 10 particles/μL, (c) sample 6, 20 particles/μL, and (d) sample 7, 50 particles/μL.

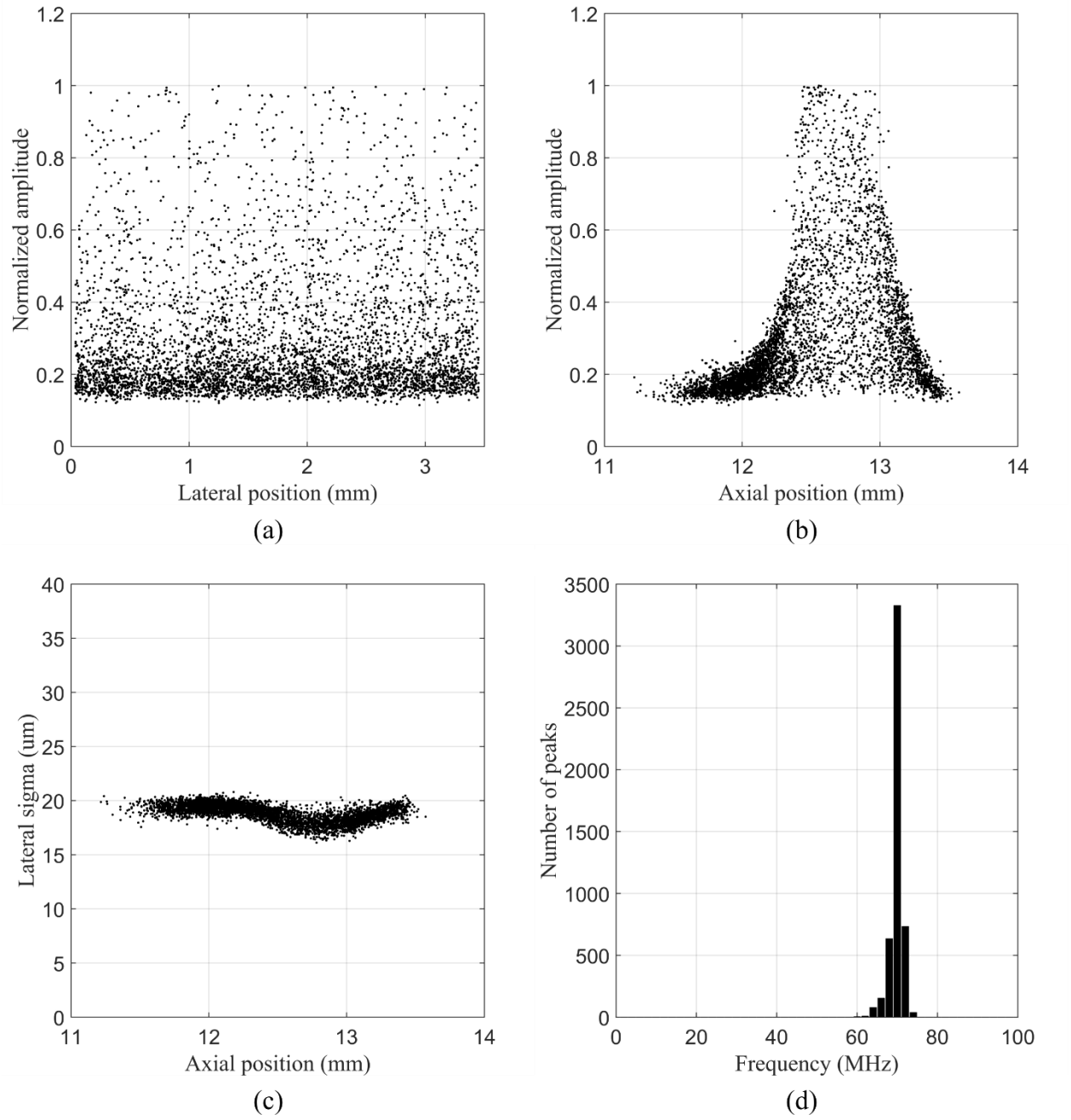

Figure 4-2. Results from particle detection for 10 μm PS microsphere samples imaged with MS (sample 6, 20 particles/μL). (a) Echo amplitudes vs. lateral positions. (b) Echo amplitudes vs. axial positions. (c) Echo lateral standard deviations vs. axial positions. (d) Histogram of the peak frequency in BSC.

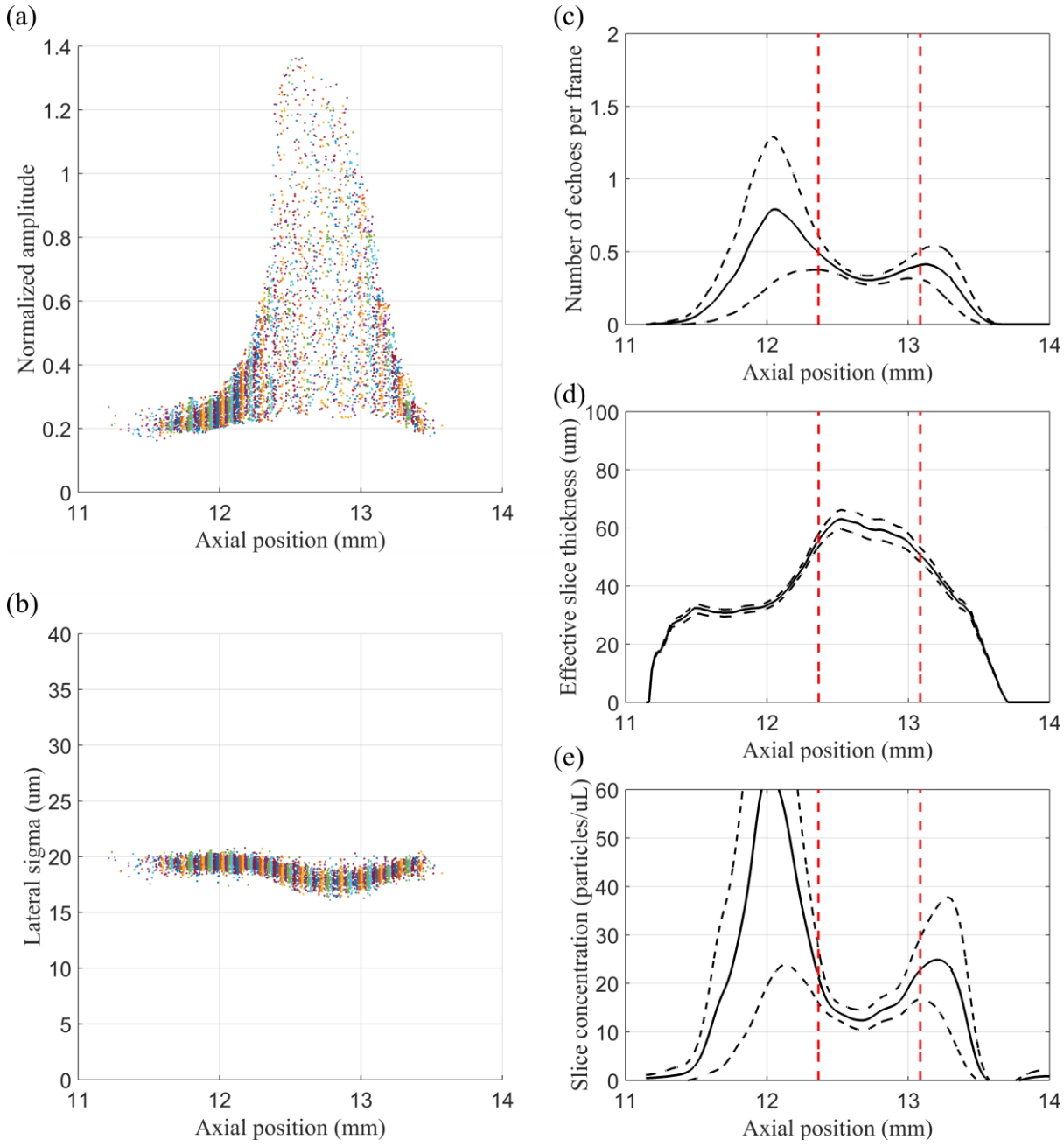

Figure 4-3. Results from the particle detection sliced along the axial direction for 10 μm PS microsphere samples imaged with MS (sample 6, 20 particles/μL): (a) echo amplitudes vs. axial positions and (b) echo lateral standard deviations vs. axial positions. Calculated parameters: (c) number of detected echoes per frame vs. axial slices, (d) effective slice thickness vs. axial slices, and (e) slice concentration vs. axial slices. The black dotted lines in the plots (c) – (e) represent the estimated measurement uncertainty and the red dotted lines represent the DOF.

4.1.2 Experiment 2

Figure 4-4 shows the B-mode images acquired with the Vevo for the same four samples shown in Figure 4-1. There are many more echoes visible in Figure 4-4 compared to Figure 4-1 even though they are the same samples, because the measurements made with the Vevo have a larger effective slice thickness. The results from the particle detection are shown in Figure 4-5. The axial slices as well as the number of detected echoes, calculated effective slice thickness, and slice concentration are shown in Figure 4-6. These measurements also follow the same trend as the ones with MS. The plot of echo amplitude vs. axial position behaves similarly in the sense that the amplitude peaks around the focal point of the transducer, which is at 7 mm. However, the shape of the plot is significantly different from that of Figure 4-2 (b). This is because the pulse-echo beam profile of the linear array used in the Vevo is drastically different from the radially-symmetric transducer used in MS. Due to the dynamic receive focusing done in Vevo, the DOF is larger. The fact that this difference is captured by the characteristics of the echo demonstrates that the interaction between the beam and the sample is being captured as intended.

It is important to note that Figure 4-5 (d) is not showing the peak frequency in the BSC, but rather in the raw frequency spectrum. This is because the bandwidth of the transducer used with the Vevo does not cover the frequency range where the peak is expected to occur. The bandwidth of MS550D, the probe used with the Vevo, spans 22 to 55 MHz while the expected frequency of the first peak in the BSC is around 70 MHz. Therefore, the backscatter energy in the 70 MHz range is too low to be visible in the BSC. This is why the peak frequency is much lower compared to experiment 1 in Figure 4-2 (d)

The effect of the difference seen in the echo amplitudes vs. axial positions is also present in the number of detected echoes, the calculated effective slice thickness and slice concentration

shown in Figure 4-6. The three plots have different shapes compared to the MS measurements, and the valid region for the final calculation is much wider as well.

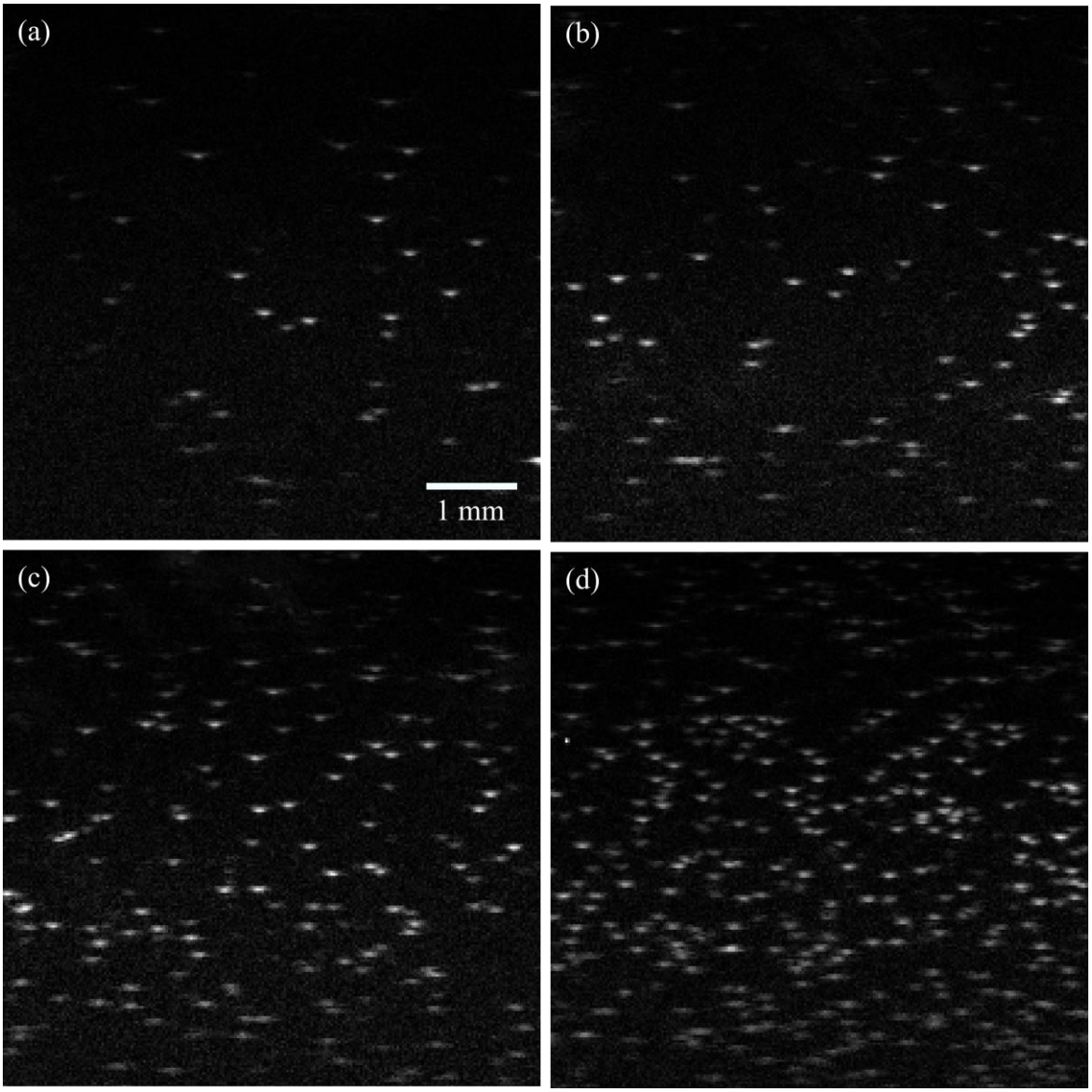

Figure 4-4. B-mode images of 10 μm PS microspheres suspended in distilled water acquired with Vevo (experiment 2). Four concentrations are shown: (a) 5 particles/μL, (b) 10 particles/μL, (c) 20 particles/μL, and (d) 50 particles/μL. The difference in the concentration can be clearly seen from the images.

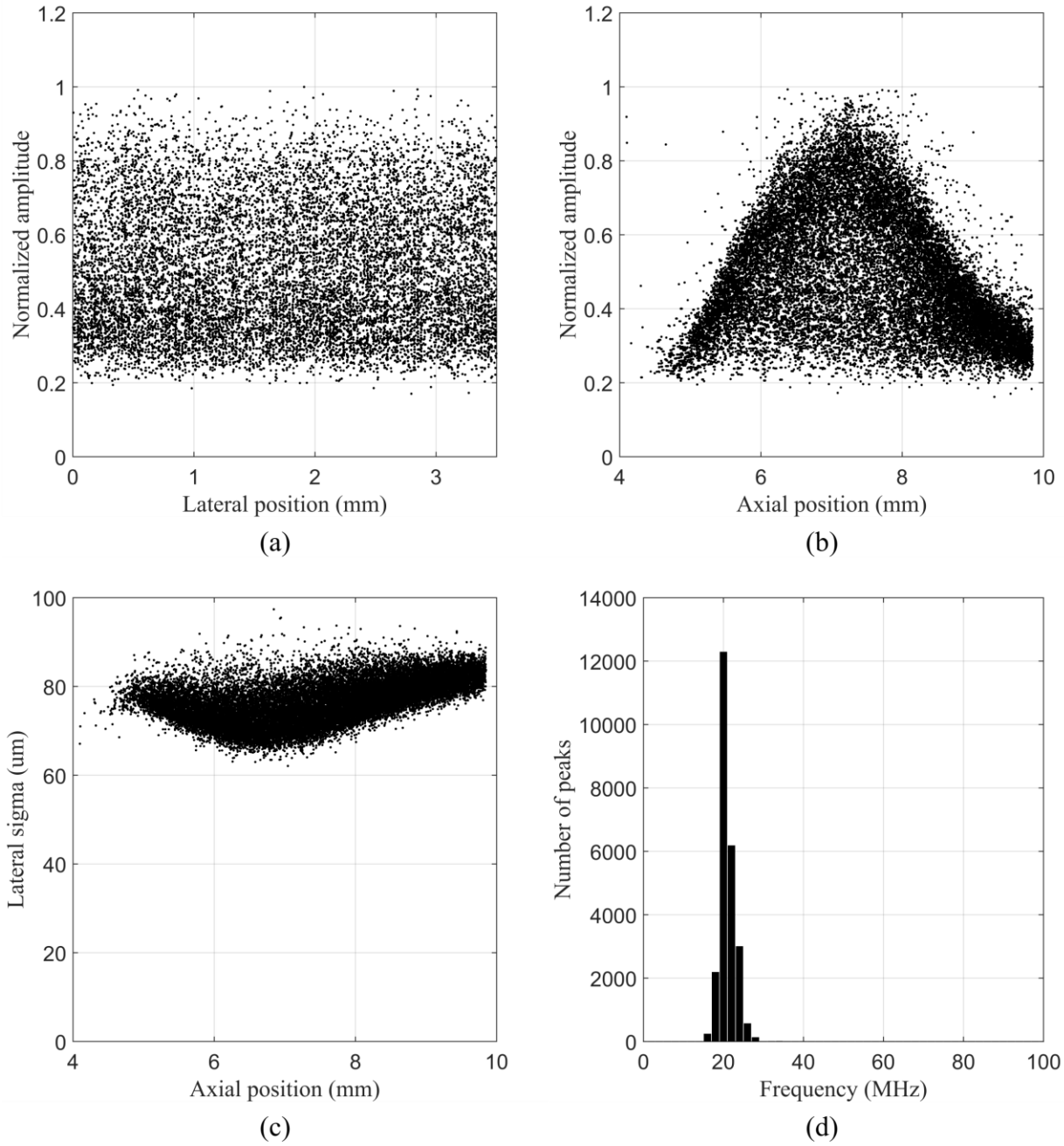

Figure 4-5. Results from particle detection for 10 μm PS microsphere samples imaged with Vevo (sample 6, 20 particles/μL). (a) Echo amplitudes vs. lateral positions. (b) Echo amplitudes vs. axial positions. (c) Echo lateral standard deviation vs. axial positions. (d) Histogram of the peak frequency in the raw frequency spectrum of the echo.

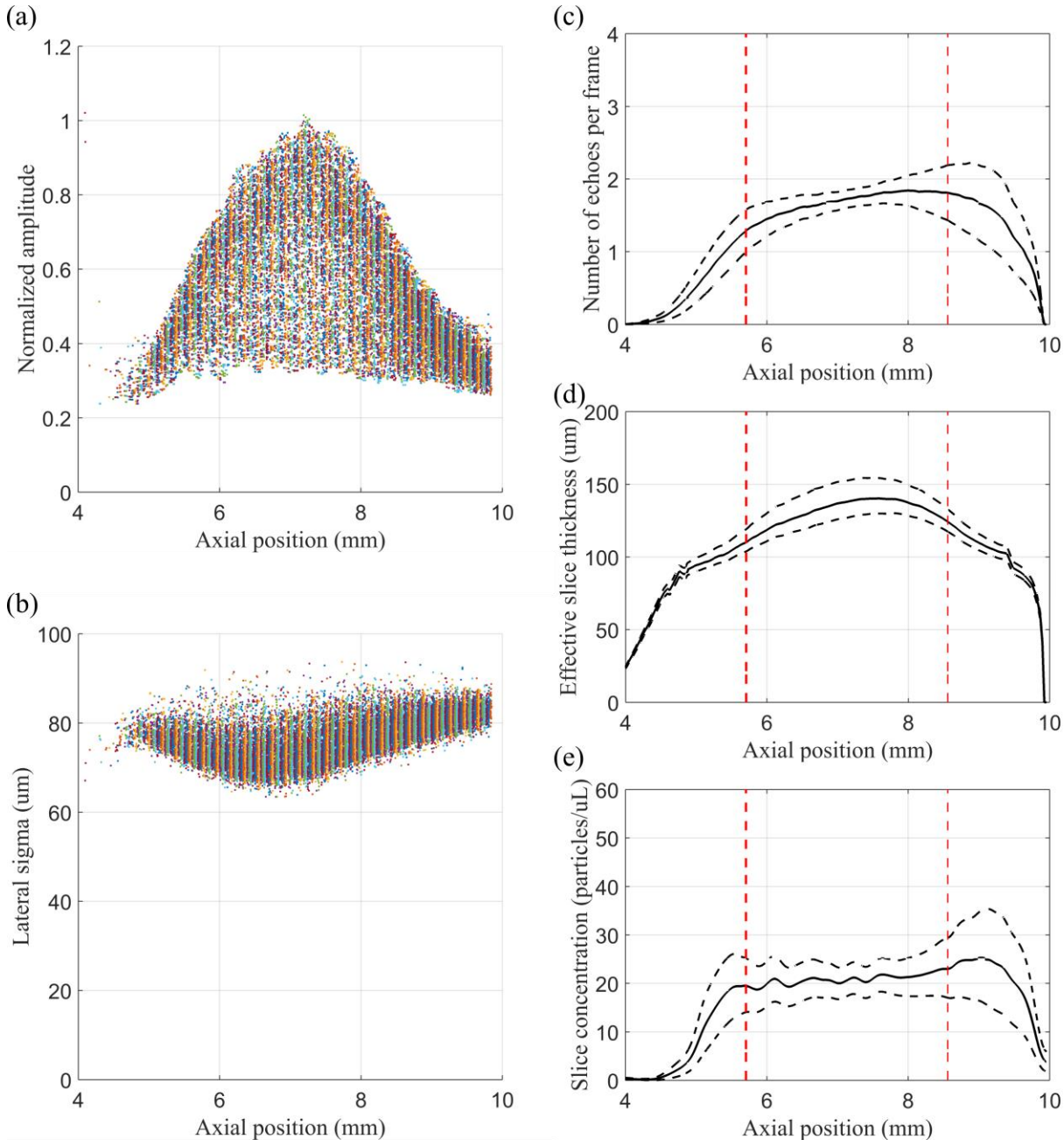

Figure 4-6. Results from the particle detection sliced along the axial direction for 10 μm PS microsphere samples imaged with the Vevo (sample 6, 20 particles/μL): (a) echo amplitudes vs. axial positions and (b) echo lateral standard deviations vs. axial positions. Calculated parameters: (c) number of detected echoes per frame vs. axial slices, (d) effective slice thickness vs. axial slices, and (e) slice concentration vs. axial slices. The black dotted lines in the plots (c) – (e) represent the estimated measurement uncertainty and the red dotted lines represent the DOF.

The concentration measurement results from all three measurement methods, including using a hemocytometer, are shown in Figure 4-7. As seen in the figure, the MS measurements show good agreement with the hemocytometer up to 200 particles/μL, while the Vevo measurements show good agreement up to 50 particles/μL. The main reason for failure in the higher concentration range is faulty particle detection. When the concentration is so high that there are too many echoes visible in the image, the detection algorithm undercounts the particles, which directly leads to underestimating the concentration. The maximum measurable concentration is different for the measurements made with MS and the Vevo because the effective slice thickness of the image is larger for the Vevo than for MS due to various factors, including differences in the acoustic output energy, signal-to-noise ratio of the system, and beam shape. Since a larger volume is analyzed, for the same concentration, more echoes are visible in the image acquired with the Vevo and the detection algorithm starts to fail at a lower concentration. The maximum measurable concentration is further addressed in Section 5.2.

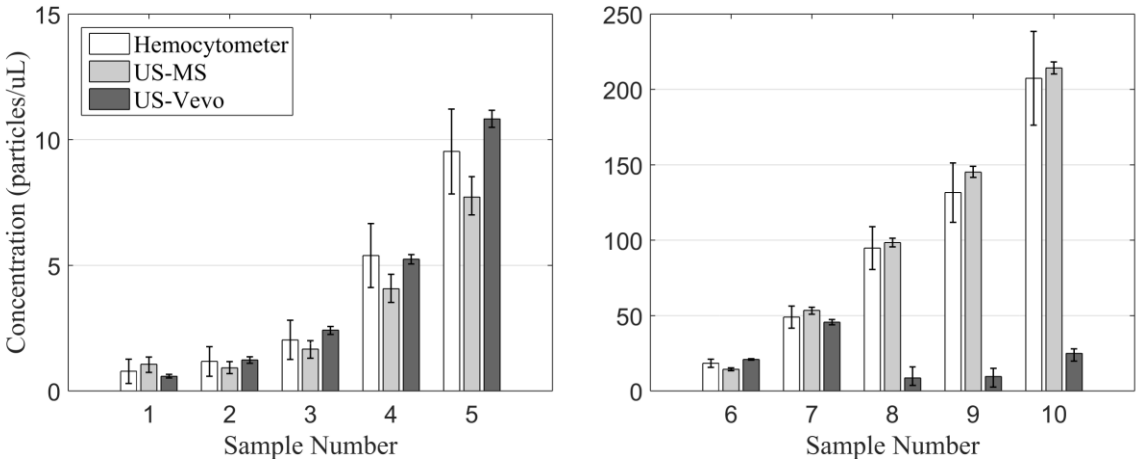

Figure 4-7. Concentration measurement results for experiment 1 and 2. The measurements made with MS show good agreement with the hemocytometer up to 200 particles/μL while the measurements made with Vevo show good agreement up to 50 particles/μL. The Vevo starts to fail at lower concentration because its effective slice thickness is larger, and thus, there are more echoes visible in the image.

4.2 Experiment 3 and 4

In experiment 3, seven samples of 15 μm PS microspheres with concentration ranging from 0.5 to 60 particles/μL are measured with MS, while in experiment 4, nine samples of 10 μm silica microspheres with concentration ranging 0.5 to 120 particles/μL are measured with MS. These experiments are performed to demonstrate that the proposed method works for different particle sizes and types. It is important to note that the parameters for the algorithm are not calibrated for different samples prior to the measurement.

4.2.1 Experiment 3: 15 μm PS microspheres

Figure 4-8 shows the B-mode images of four samples of 15 μm PS microspheres imaged with MS. The concentrations of the samples are (a) 0.9 particles/μL, (b) 1.7 particles/μL, (c) 3.4 particles/μL, and (d) 6.9 particles/μL. The echoes are visibly wider than the 10 μm PS microspheres in Figure 4-1. The shape of the echoes in the axial direction is also different with more reverberation-like pattern. These differences are due to the larger particle size. This will be confirmed by the larger lateral standard deviation and the lower peak frequency in the BSC.

The results from the particle detection are shown in Figure 4-9. The lateral sigma shown in Figure 4-9 (c) is about 30 μm, which is larger compared to the 20 μm lateral sigma for the 10 μm PS microspheres measured with MS in Figure 4-2 (c), despite the fact that the measurement is performed with the same transducer. This is because, as discussed previously, the lateral sigma, which is used to model the SSF depends not only on the beam, but also on the sample being imaged. The larger lateral sigma confirms that the interaction of the beam with larger particles is being captured correctly.

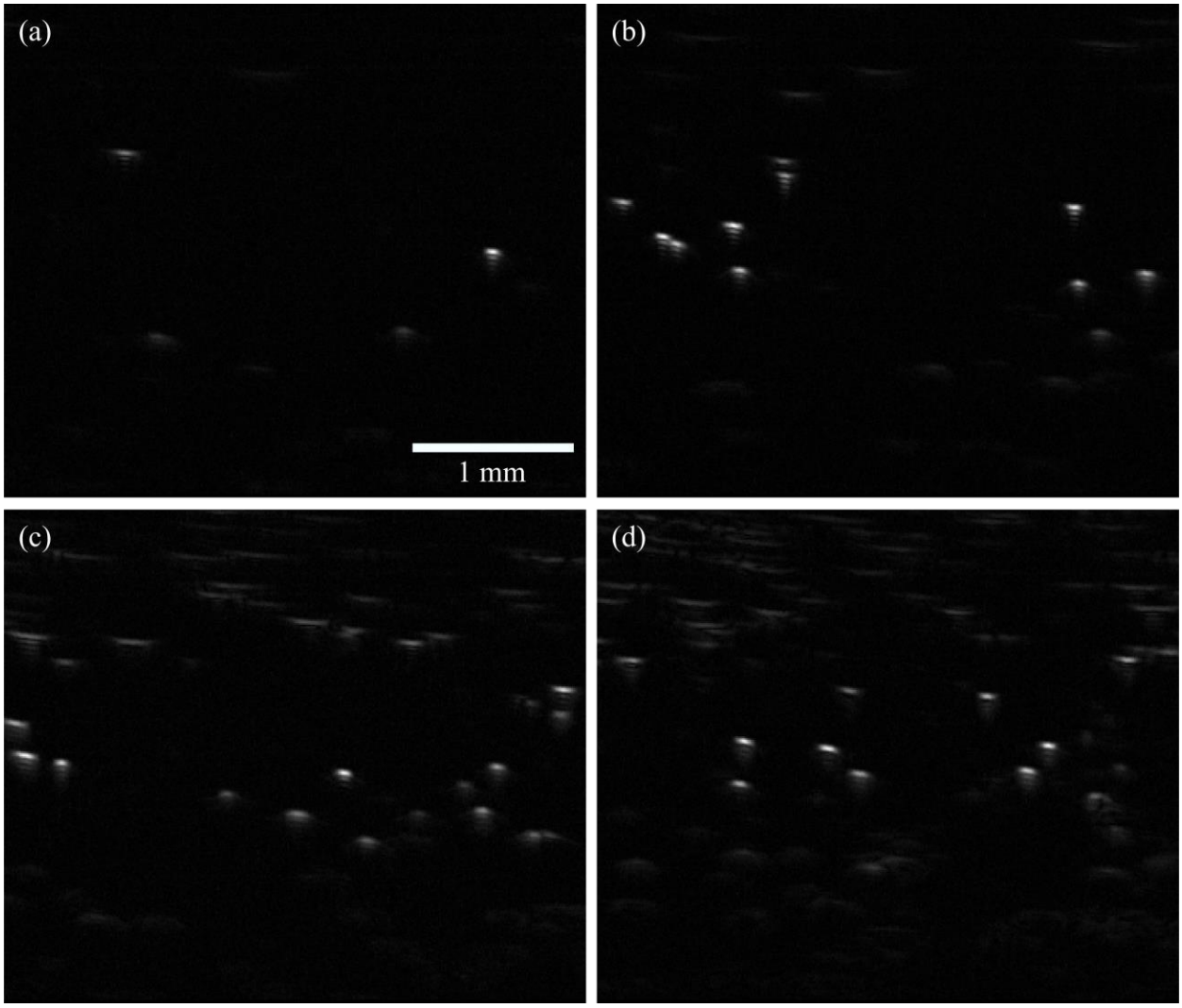

Figure 4-8. B-mode images of 15 μm PS microspheres suspended in distilled water acquired with MS (experiment 3). Four concentrations are shown: (a) 0.9 particles/μL, (b) 1.7 particles/μL, (c) 3.4 particles/μL, and (d) 6.9 particles/μL.

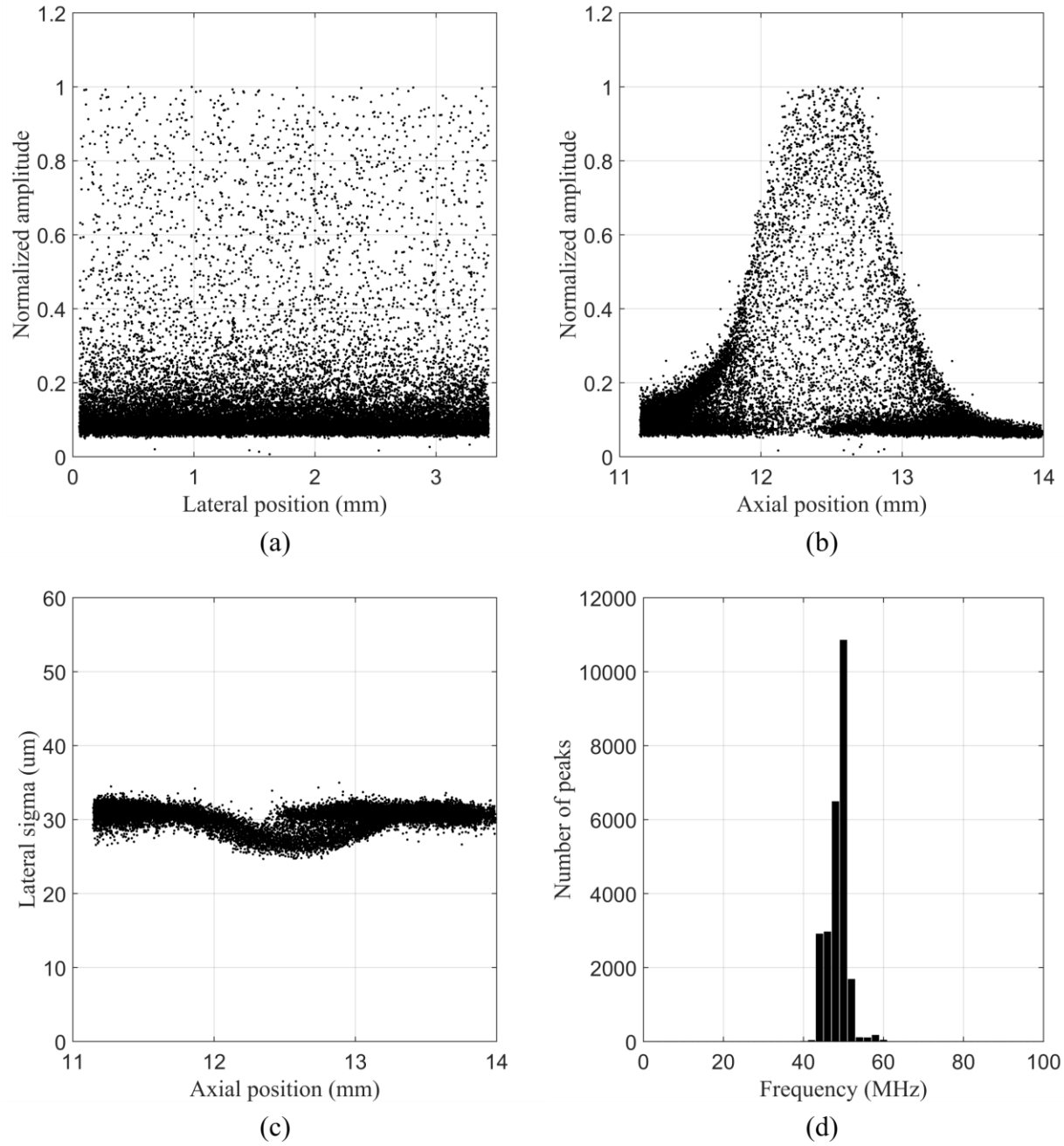

Figure 4-9. Results from particle detection for 15 μm PS microsphere samples imaged with MS (sample 5, 13.7 particles/μL). (a) Echo amplitudes vs. lateral positions. (b) Echo amplitudes vs. axial positions. (c) Echo lateral standard deviation vs. axial positions. (d) Histogram of the peak frequency in the BSC.

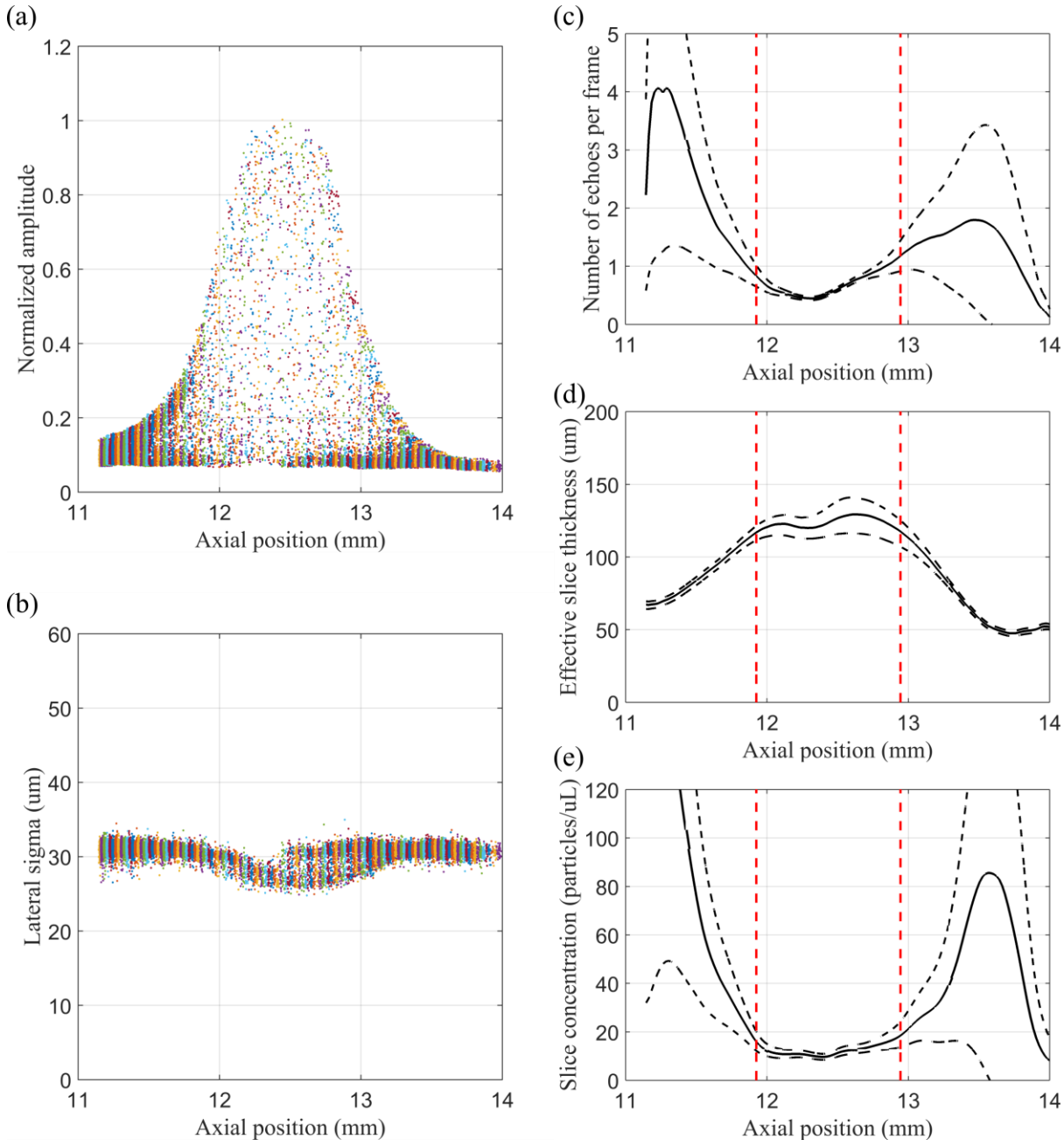

Figure 4-10. Results from the particle detection sliced along the axial direction for 15 μm PS microsphere samples imaged with MS (sample 5, 13.7 particles/μL): (a) echo amplitudes vs. axial positions and (b) echo lateral standard deviation vs. axial positions. Calculated parameters: (c) number of detected echoes per frame vs. axial slices, (d) effective slice thickness vs. axial slices, and (e) slice concentration vs. axial slices. The black dotted lines in the plots (c) – (e) represent the estimated measurement uncertainty and the red dotted lines represent the DOF.

The larger particle size is also reflected in the peak frequency in the BSC as shown in Figure 4-9 (d). The peak frequencies are around 50 MHz, which is consistent with the prediction by the Faran model for 15 μm PS microspheres. This is significantly different than the peak frequencies from 10 μm PS microspheres, which is what allows clustering to be performed for the polydispersed samples in experiment 5.

The axial slices, and the number of detected echoes, the calculated effective slice thickness, and the slice concentration are shown in Figure 4-10. While they follow the same trend as in experiment 1, the valid axial region for final concentration calculation is significantly larger due to the larger effective DOF caused by the larger particle size. Another way to understand this phenomenon is by noting that the ultrasound frequency that is involved in backscattering from a larger particle is lower than that from a smaller one. Since the frequency is lower and thus the wavelength larger, the effective DOF should also be larger, which is what is observed in the amplitude vs. axial position plot in Figure 4-10 (a).

As shown in Figure 4-11, the 15 μm PS microsphere samples show similar results compared to the 10 μm PS microsphere samples. The proposed method shows good agreement with the hemocytometer in the lower concentration range but fails in the higher concentration range. The maximum measurable concentration is 60 particles/μL for the 15 μm PS microspheres measured with MS. As in experiments 1 and 2, the difference in maximum measurable concentration is due to the difference in the effective slice thickness, which, in this case, is from the difference in echogenicity caused by the larger particle size. The higher echogenicity results in a larger number of echoes being visible in the image, for the same concentration, which leads to the detection algorithm failing at a lower concentration.

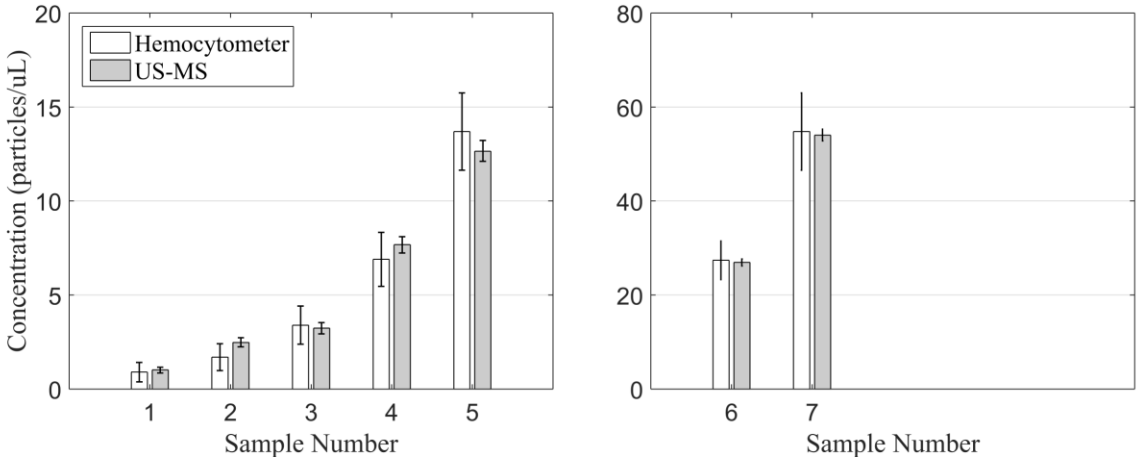

Figure 4-11. Concentration measurement results for experiment 3, 15 μm PS microspheres measured with MS. The ultrasound method show good agreement with the hemocytometer up to about 60 particles/μm.

4.2.2 Experiment 4: 10 μm silica microspheres

Figure 4-12 shows the B-mode images of four samples of 10 μm silica microspheres imaged with MS. The concentrations of the samples are (a) 3.8 particles/μL, (b) 7.5 particles/μL, (c) 15 particles/μL, and (d) 30 particles/μL. The results from the particle detection are shown in Figure 4-13 and the axial slices as well as the number of detected echoes, calculated effective slice thickness, and slice concentration are shown in Figure 4-14. While the width of the echoes are similar to the 10 μm PS microspheres in Figure 4-1, the shape along the axial direction is different in the sense that there is less reverberation-like pattern present. This is due to the difference in the acoustic properties between silica and PS.

The amplitude vs. axial position plot shown in Figure 4-13 (b) is much noisier compared to the PS microspheres. While the dark region in the plot does show a similar trend to that observed in both PS microsphere samples, there are outliers with larger amplitudes. This is likely due to the adhered particles. Unlike PS microspheres that rarely adhere to each other because they are slightly negatively charged, the silica microspheres have some tendency to adhere to each other.

This is also observed during the hemocytometer measurement where a small fraction (< 10 %) of microspheres are adhered together.

The lateral sigma is about 30 μm as shown in Figure 4-13 (c), which is similar to that of the 15 μm PS microspheres. This is likely due to the fact that the silica microspheres are more echogenic than PS microspheres. The peak frequency in the BSC is around 40 MHz as shown in Figure 4-13 (d), which is consistent with the Faran model for a 10 μm silica microsphere. The spread of the frequencies is larger than for the PS microspheres, which is likely from the fact that some of the particles are adhered together.

The calculated effective slice thickness shown in Figure 4-14 (d) is much more uniform across axial positions than for PS microspheres. This is because the echo amplitudes do not follow the clear trend that is seen with PS microspheres. Since there are high amplitude echoes at axial positions away from the focal distance, the resulting depth is also larger. The calculated slice concentration shown in Figure 4-14 (e) is also noisier compared to the PS microspheres due to the outliers observed in Figure 4-14 (a), but it does not severely affect the overall concentration calculation.

The calculated concentrations for the 10 μm silica microsphere samples measured with MS are shown in Figure 4-15. Despite the likely particle adherence, the proposed method shows good agreement with the hemocytometer up to about 120 particles/μL. This is because the particles that are adhered to each other are only a small fraction of the entire sample. The result of experiment 4 is significant because it shows that the proposed method works with a different particle type that has a completely different acoustic properties. It is able to adapt to the different particle type because the resulting echoes reflect these properties.

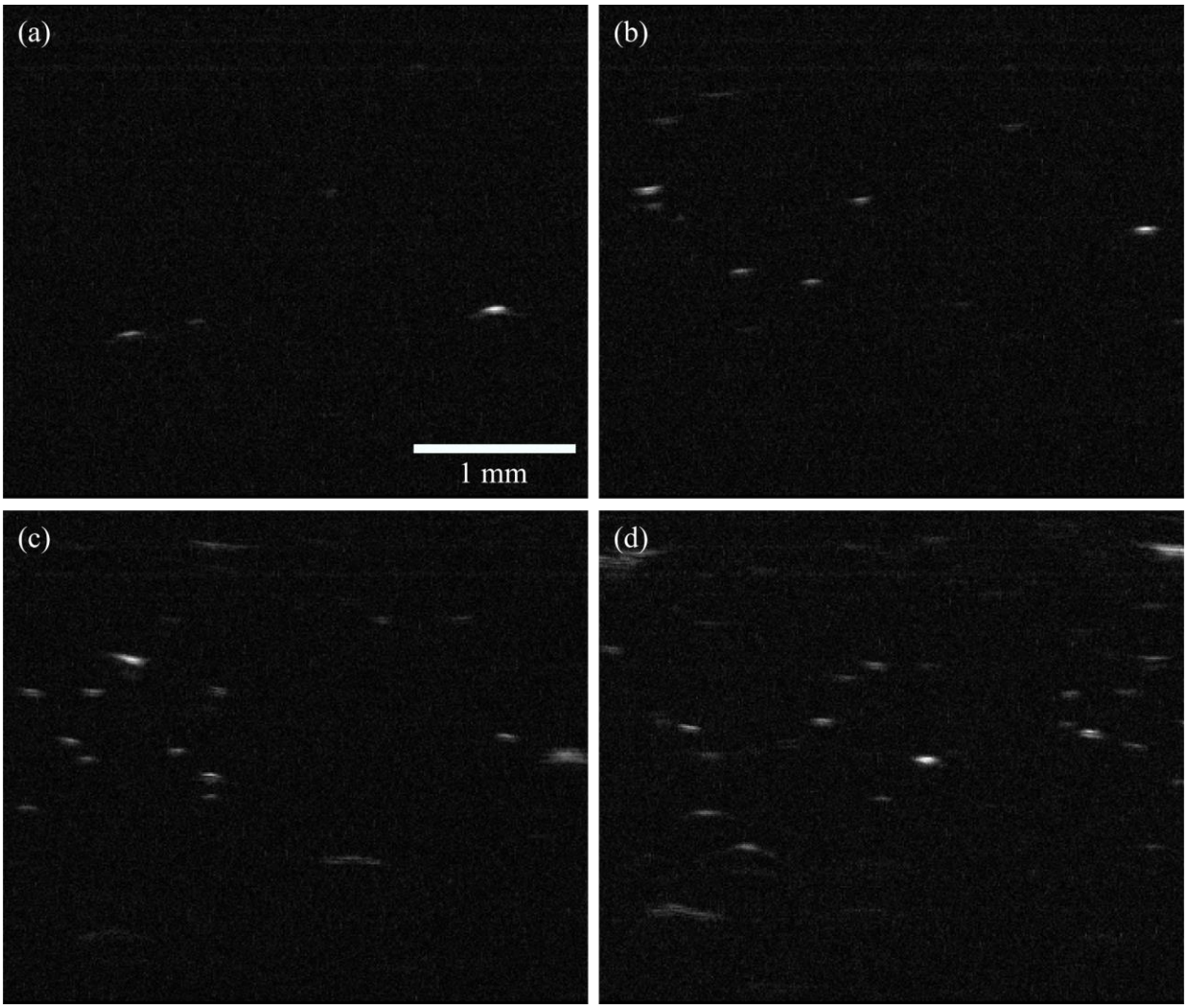

Figure 4-12. B-mode images of 10 μm silica microspheres suspended in distilled water acquired with MS (experiment 4). Four concentrations are shown: (a) 3.8 particles/μL, (b) 7.5 particles/μL, (c) 15 particles/μL, and (d) 30 particles/μL.

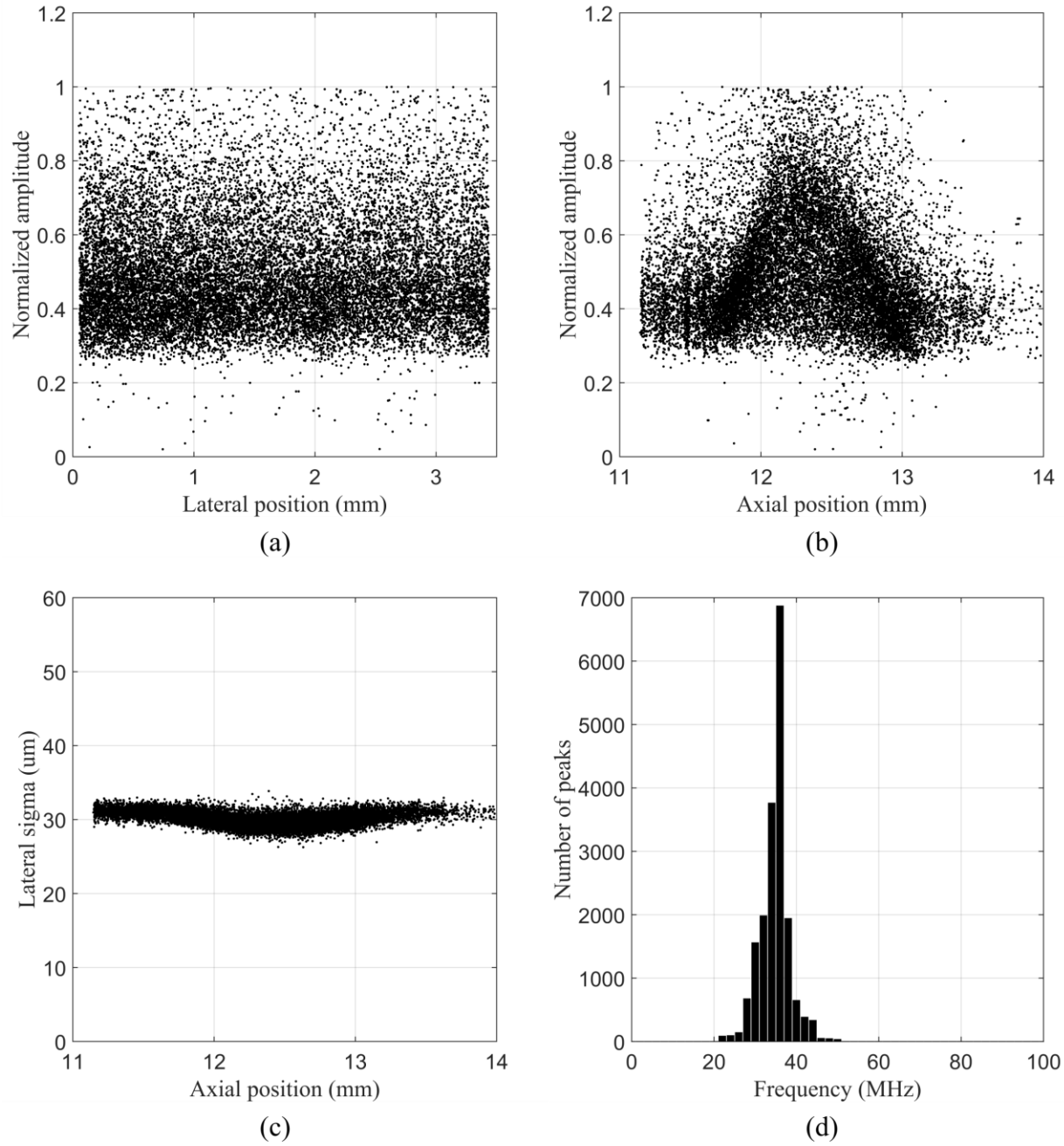

Figure 4-13. Results from particle detection for 10 μm silica microsphere samples imaged with MS (sample 8, 60 particles/μL). (a) Echo amplitudes vs. lateral positions. (b) Echo amplitudes vs. axial positions. (c) Echo lateral standard deviations vs. axial positions. (d) Histogram of the peak frequency in the BSC.

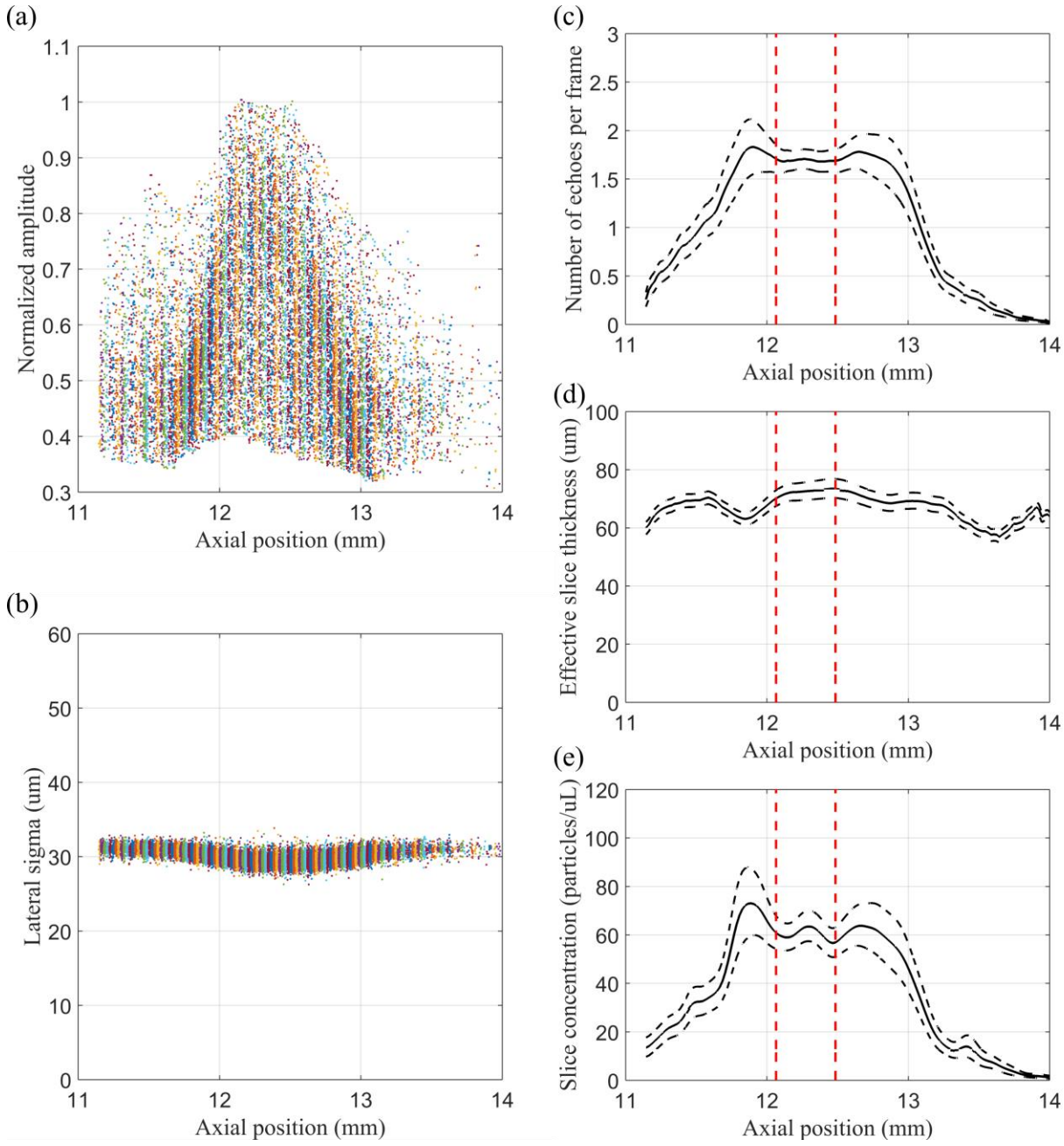

Figure 4-14. Results from the particle detection sliced along the axial direction for 10 μm Silica microsphere samples imaged with MS (sample 8, 60 particles/μL): (a) echo amplitudes vs. axial positions and (b) echo lateral standard deviations vs. axial positions. Calculated parameters: (c) number of detected echoes per frame vs. axial slices, (d) effective slice thickness vs. axial slices, and (e) slice concentration vs. axial slices. The black dotted lines in the plots (c) – (e) represent the estimated measurement uncertainty and the red dotted lines represent the DOF.

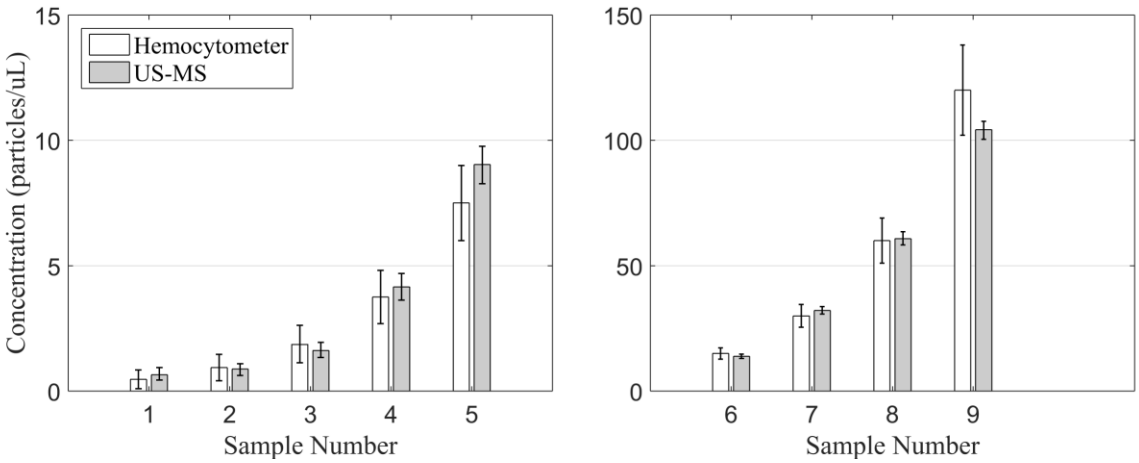

Figure 4-15. Concentration measurement results for experiment 4, 10 μm silica microspheres measured with MS. The ultrasound method show good agreement with the hemocytometer up to about 120 particles/μm.

4.3 Experiment 5

In experiment 5, polydispersed samples of 10 μm and 15 μm diameter PS microspheres are measured with MS. The objective of this experiment is to demonstrate the performance of BSC-based particle type clustering and concentration measurement. The B-mode images of the samples are shown in Figure 4-16. The 10 μm PS microsphere concentration ranges from 1 to 12 particles/μL, while the 15 μm PS microsphere concentration is held constant at 2.5 particles/μL. Although it is possible to tell from the B-mode images that the overall concentration is increasing, it is not easy to tell how it is changing for the different particle types because it is difficult to identify visually which echoes belong to which particle.

The results from the particle detection are shown in Figure 4-17. The results shown in the figure are after the BSC-based clustering. The red marks are for the 10 μm PS microspheres and the black marks indicate for the 15 μm PS microspheres. Figure 4-17 (a) shows the echo amplitudes vs. axial positions. The two populations are clearly separated and each follows the same trend that has been observed in monodispersed samples in experiment 1 and 3. It resembles

what it would have been if Figure 4-2 (b) is overlaid on top of Figure 4-9 (b). The lateral sigma shown in Figure 4-17 (b) also show a similar result.

The calculated effective slice thickness shown in Figure 4-17 (c) is an important demonstration of the key concept behind the proposed method. Despite experiencing the same measurement conditions, and despite both particle populations being in the same at the same time, the effective slice thickness for the two particle types are different due to their different echogenicity. The different echogenicity results in different echo shapes, which is captured by the proposed method to result in accurate estimation of the different slice thickness. For the 10 μm PS microspheres, the effective slice thickness is around 70 μm and for the 15 μm PS microspheres, the effective slice thickness is around 100 μm.

The concentrations measured for each particle type in the samples after classification are shown in Figure 4-18 (a). As seen in the figure, the concentrations measured for each particle type show good agreement with the hemocytometer measurement. This demonstrates that the clustering and the estimation of the type-dependent effective slice thickness works as expected. The histogram of the peak frequency in the BSC of all detected particles after classification are shown in Figure 4-18 (b). Despite the fact that the 15 μm PS microspheres have lower concentration, they show larger counts because the effective slice thickness is larger for 15 μm PS.

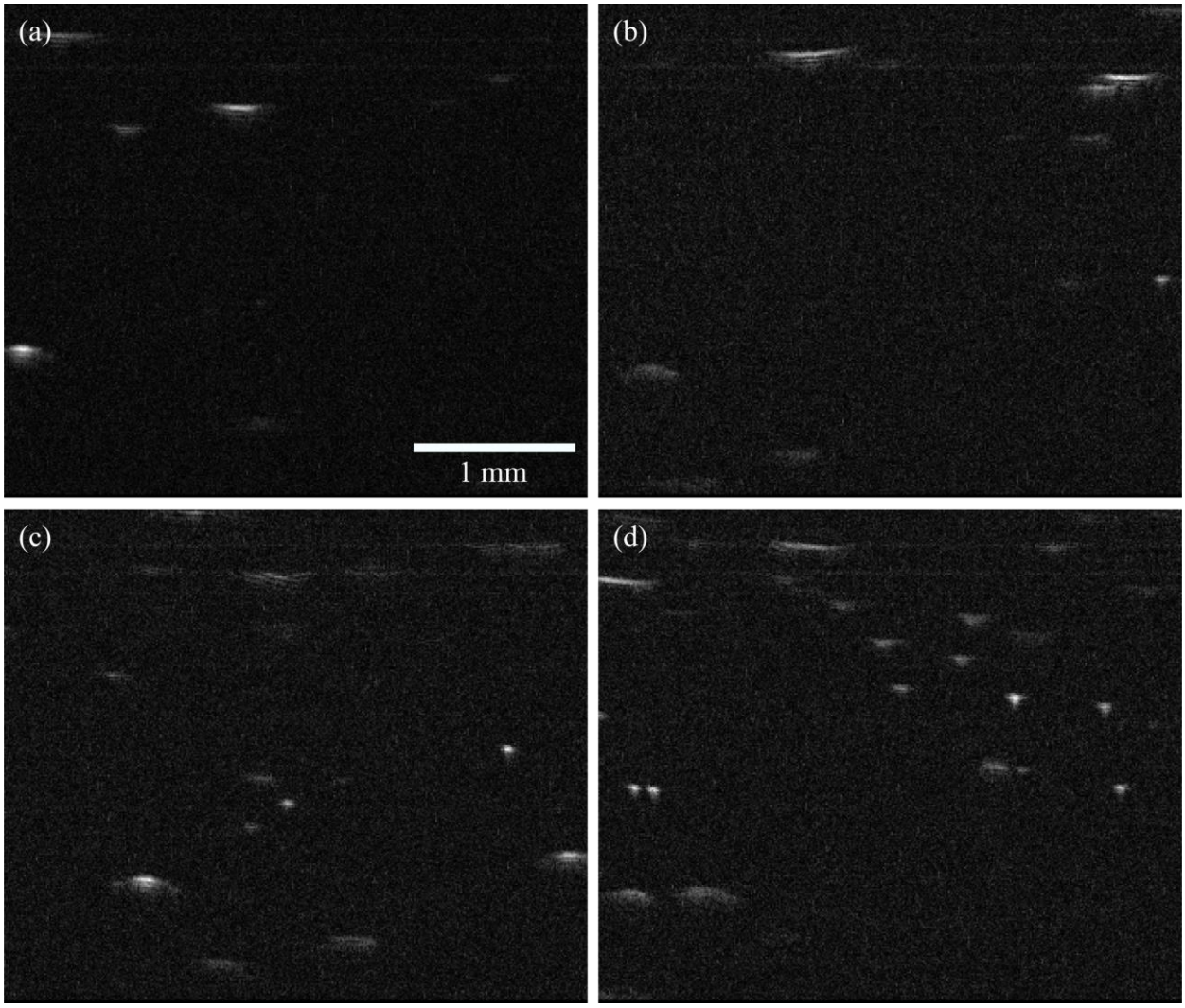

Figure 4-16. B-mode images of polydispersed samples of 10 μm and 15 μm PS microspheres suspended in distilled water acquired with MS (experiment 5). Four sets of concentrations are shown (10 μm PS:15 μm PS): (a) 1.5:2.5 particles/μL, (b) 3:2.5 particles/μL, (c) 6:2.5 particles/μL, and (d) 12:2.5 particles/μL.

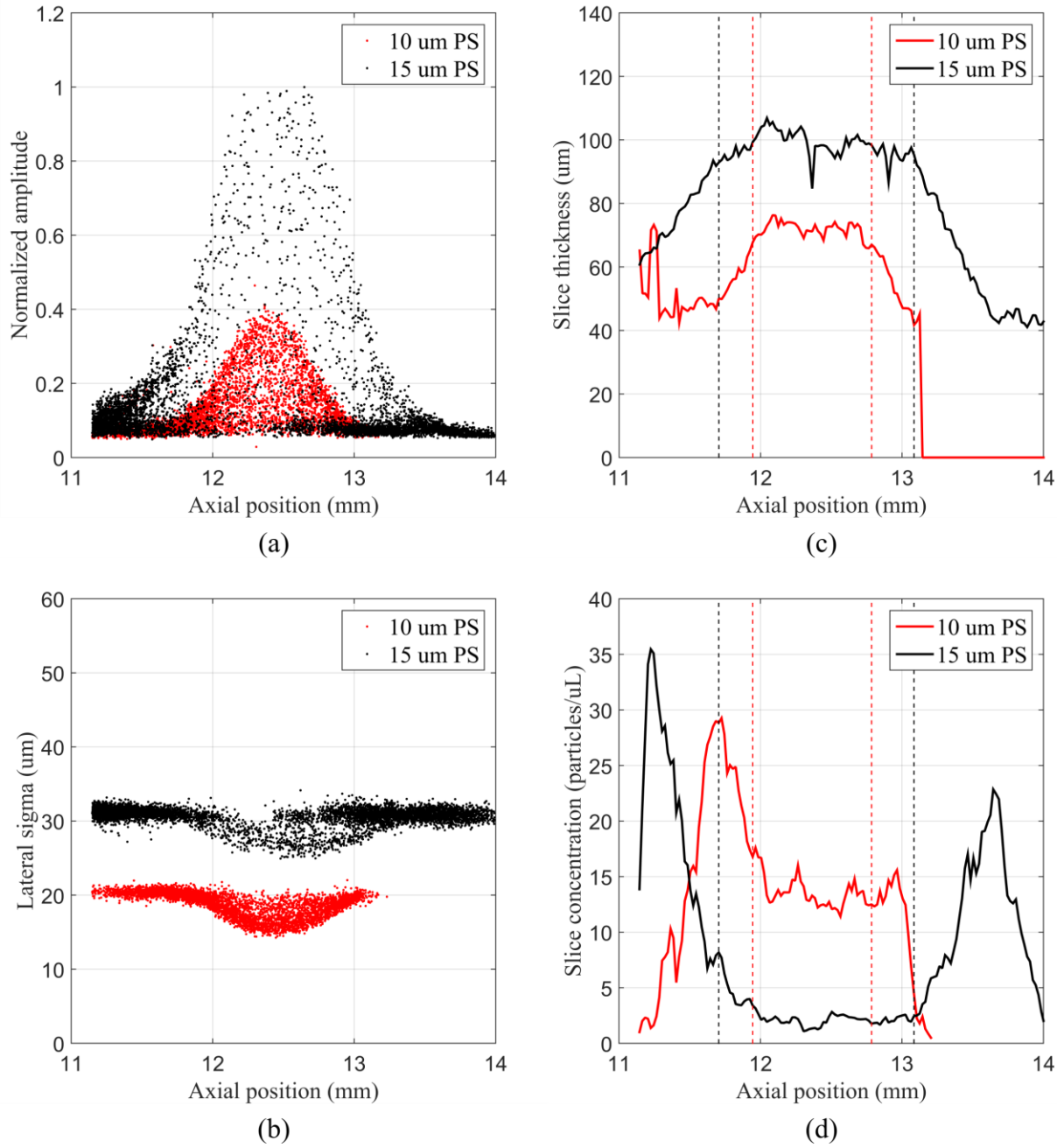

Figure 4-17. Results from particle detection for polydispersed samples of 10 μm and 15 μm PS microspheres suspended in distilled water acquired with MS (experiment 5) (sample 4, 12:2.5 particles/μL). (a) Echo amplitudes vs. lateral positions. (b) Echo lateral standard deviation vs. axial positions. (c) Calculated effective slice thickness vs. axial slices. (d) Calculated slice particle concentration vs. axial slices.

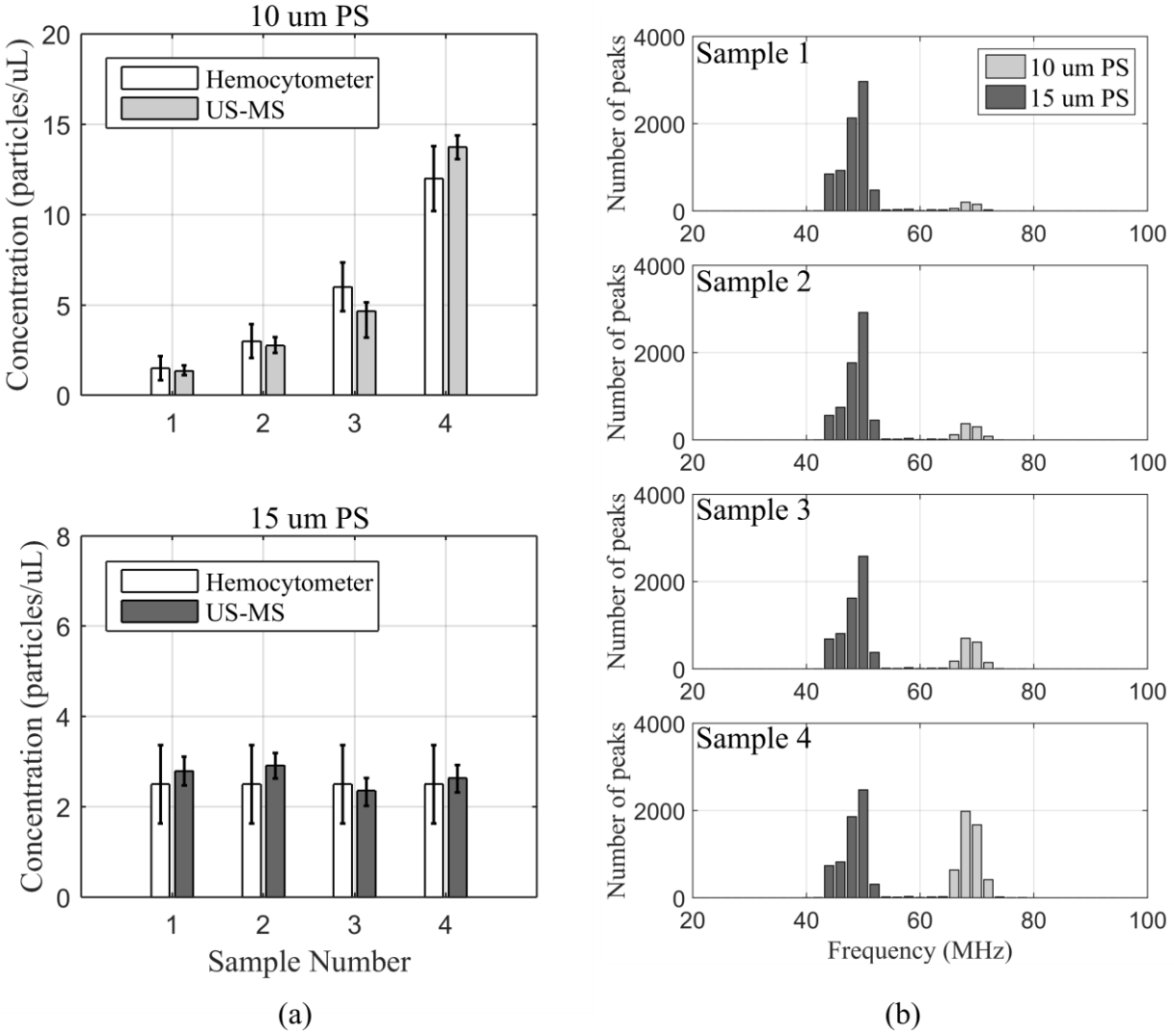

Figure 4-18. Concentration measurement results for experiment 5. Four polydispersed samples of 10 μm and 15 μm PS microspheres are measured with MS. (a) Concentration of 10 μm PS microspheres (top) and 15 μm PS microspheres (bottom) for each samples. (b) Histogram of the peak frequency in BSC of detected echoes after classification for each sample.

4.4 Experiment 6

In experiment 6, the samples consisting of T cells suspended in PBS are measured with the Vevo. The purpose of this experiment is to determine how the method performs for non-ideal particles such as human cells. The previous experiments used ideal microspheres that are manufactured with tight control of their shapes and sizes. In contrast, biological cells, even of the

same type, can vary widely in terms of their size and shape depending on various factors, such as environment, cell cycle, etc [28]. Therefore, it is important to evaluate the performance of the method for realistic particle types and identify any key challenges.

Figure 4-19 shows the B-mode images of four samples of T cells imaged with the Vevo. The concentrations of the samples are (a) 9.4 particles/μL (b) 18.8 particles/μL, (c) 37.5 particles/μL, and (d) 75 particles/μL. The number of visible echoes correlates well with the concentration, although the density of the echoes is high in Figure 4-19 (d) where it is starting to become difficult to distinguish the individual echoes. As discussed, this leads to detection failure and error in calculating the concentration.

The results from particle detection are shown in Figure 4-20, and the axial slices, the number of detected echoes, calculated effective slice thickness, and slice concentration are shown in Figure 4-21. The detection results show a similar trend as for the PS microspheres. The echo amplitude vs. axial positions shown in Figure 4-20 (b) is much noisier compared to the 10 μm PS microspheres in Figure 4-2 (b), which is likely due to the variability in the shape and size of the cells. The lateral sigma is about 80 μm, which is close to the 10 μm PS microspheres measured with the Vevo. While the lateral sigma is also noisier compared to the PS microsphere measurements, its range is relatively tight, which suggests that the extent of the variation in cell size and shape is not excessive.

It is important to note that as in experiment 2, Figure 4-20 (d) is not showing the peak frequency in the BSC but in the raw frequency spectrum, because the bandwidth of the transducer does not cover the frequency range where the peak should occur.

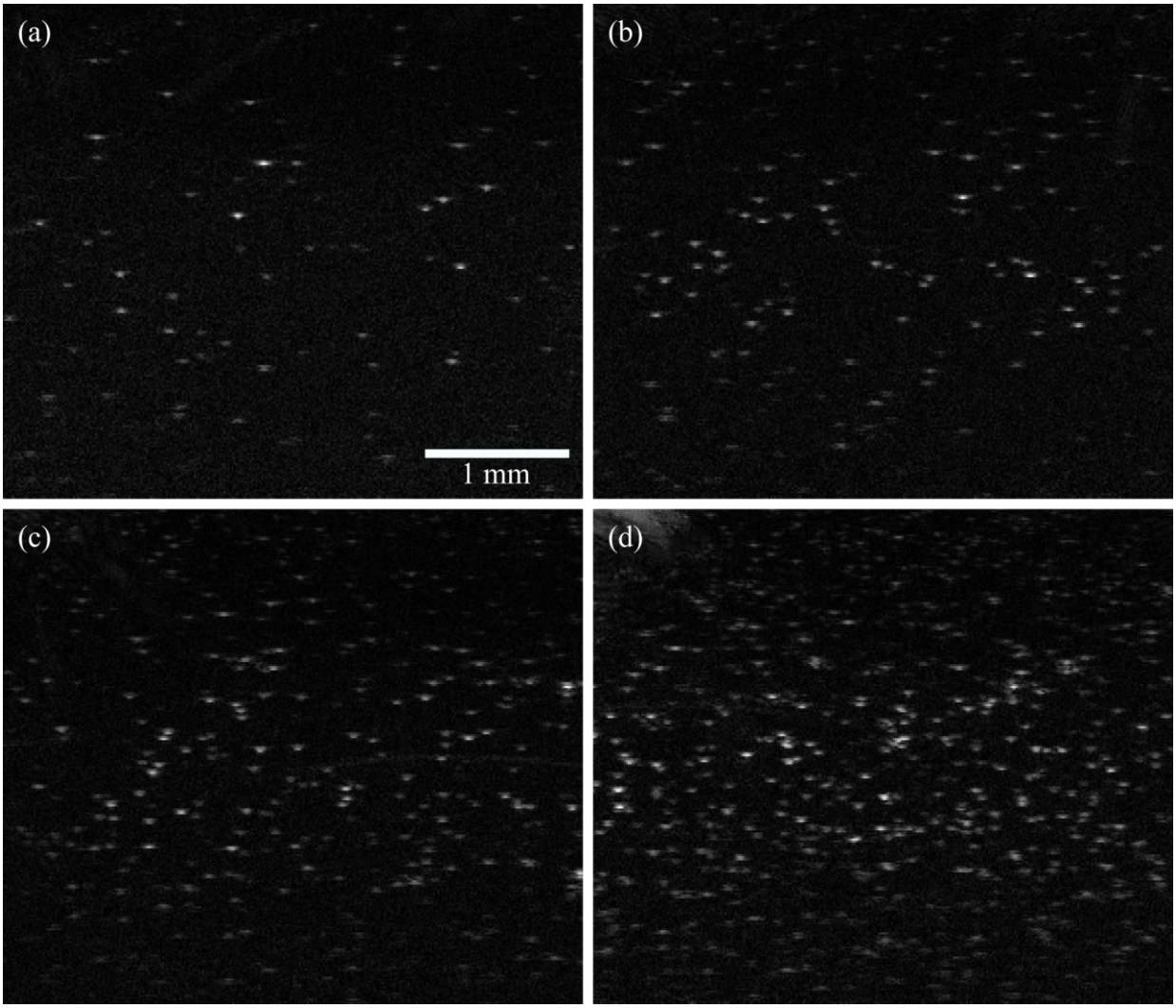

Figure 4-19. B-mode images of human T cells suspended in PBS acquired with the Vevo (experiment 6). Four concentrations are shown: (a) 9.4 cells/μL, (b) 18.8 cells/μL, (c) 37.5 cells/μL, and (d) 75 cells/μL.

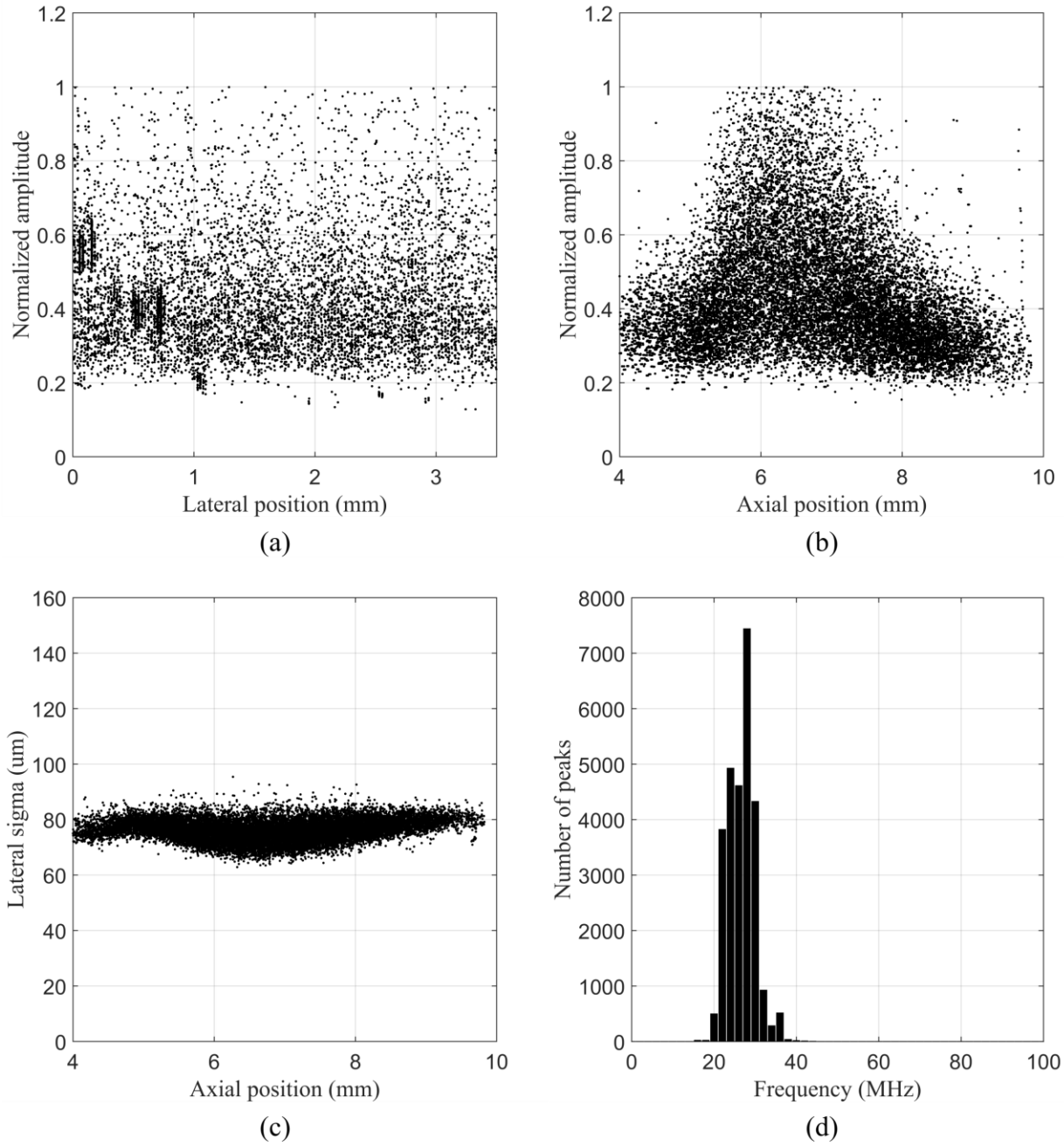

Figure 4-20. Results from particle detection for human T cell samples imaged with MS (sample 7, 37.5 particles/μL). (a) Echo amplitudes vs. lateral positions. (b) Echo amplitudes vs. axial positions. (c) Echo lateral standard deviation vs. axial positions. (d) Histogram of the peak frequency in the raw frequency spectrum of the echo.

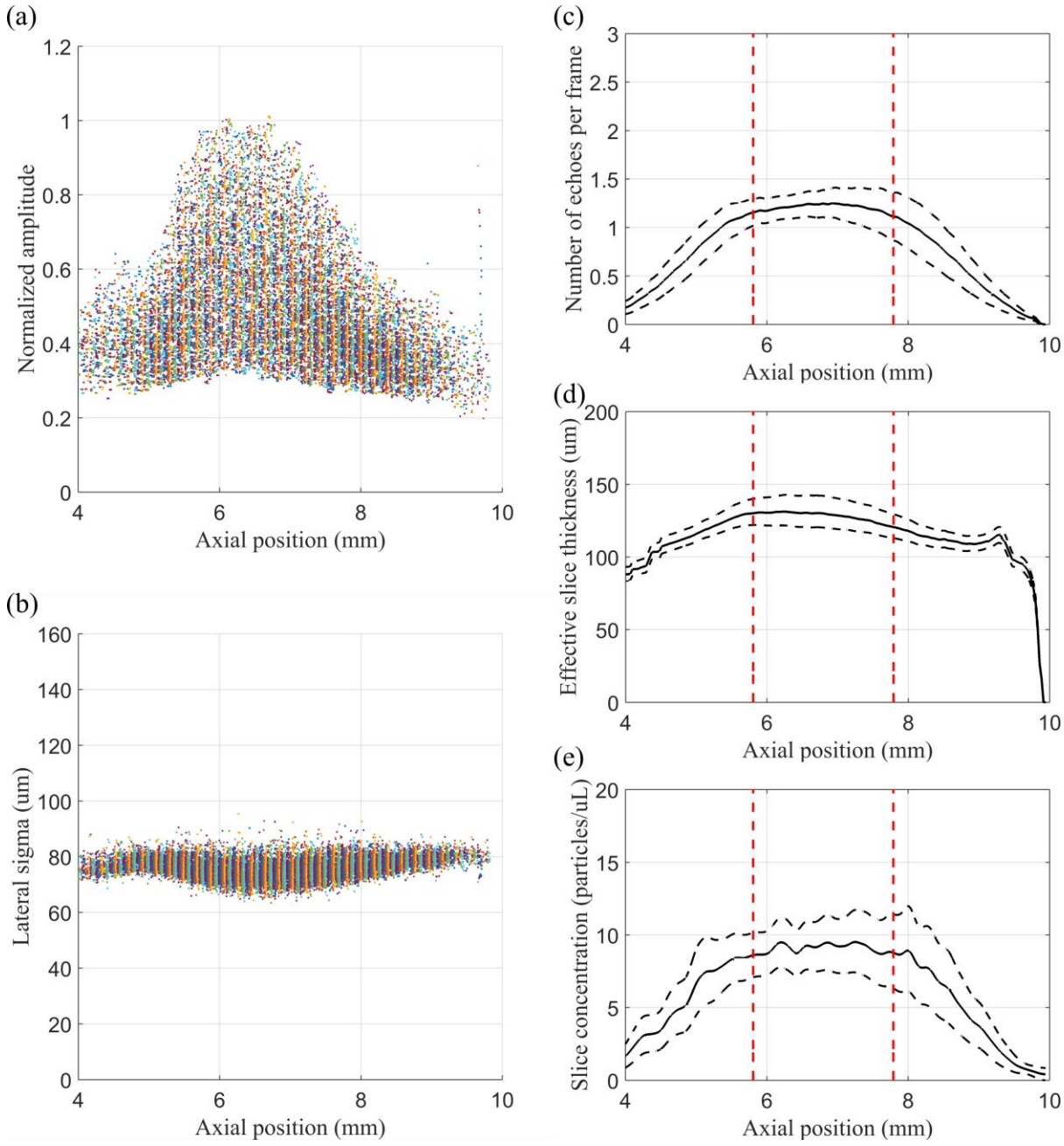

Figure 4-21. Results from the particle detection sliced along the axial direction for human T cell samples imaged with MS (sample 7, 9.4 particles/μL): (a) echo amplitudes vs. axial positions and (b) echo lateral standard deviation vs. axial positions. Calculated parameters: (c) number of detected echoes per frame vs. axial slices, (d) effective slice thickness vs. axial slices, and (e) slice concentration vs. axial slices. The black dotted lines in the plots (c) – (e) represent the estimated measurement uncertainty and the red dotted lines represent the DOF.

The concentration measurement results are shown in Figure 4-22. The results show good agreement with the hemocytometer up to 20 cells/μL. As in other experiments, the method fails at higher concentrations due to particle detection failure.

This experiment is a promising result because it demonstrates that the proposed method works with human cells that are much more non-ideal compared to the microspheres. It should be noted that while the T cells have larger variability compared to the microspheres, the echo amplitude and the lateral sigma measurements suggest that the variability in their shapes and sizes are not excessive, which allows the concentration measurement to be successful.

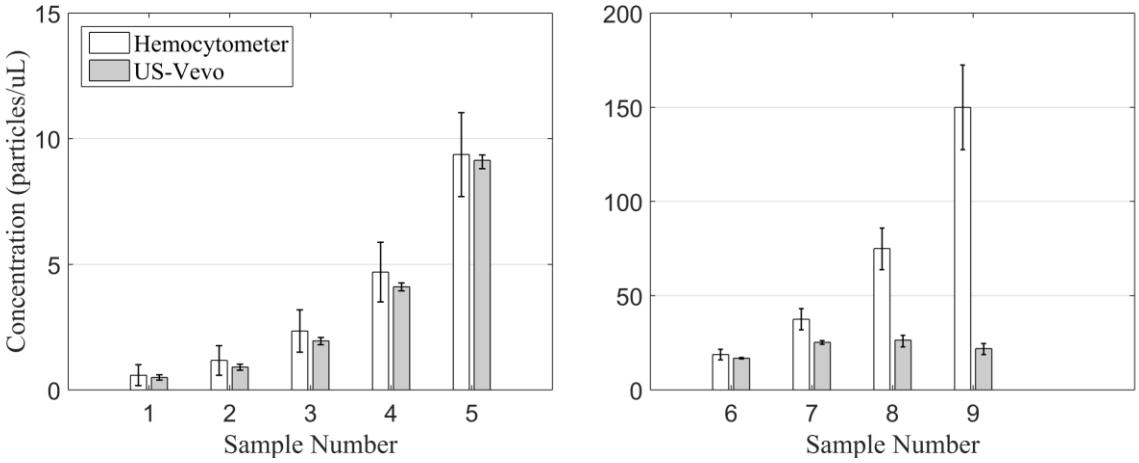

Figure 4-22. Concentration measurement results for experiment 6. T cells suspended in PBS are measured with the Vevo.

5. Discussion

In this chapter, three key concepts related to the proposed method are discussed. In Section 5.1, the dependence of image volume on various measurement parameters is discussed in detail. In Section 5.2, the concept of maximum measurable concentration for a given measurement setup is discussed as well as ways to increase the measurable concentration. Finally, in Section 5.3, the effect of the number of detections on measurement accuracy is discussed.

5.1 Image Volume Dependencies

An important principle behind the proposed method is that the volume being analyzed by the image depends not only on the imaging system but on the entire imaging setup including the particle type and the suspension medium of the sample. This is because the effective slice thickness is determined by the interaction between the ultrasound beam and the sample.

The imaging system, of course, has a large effect. The beam characteristics determined by the geometry of the transducer and beam formation are major factors in particle detection and concentration estimation. Having a different beam shape even for the same imaging system will result in different effective slice thickness. In addition, other settings such as focusing, gain, and filtering all contribute to controlling the effective slice thickness. For example, setting the gain larger to increase the SNR will result in a larger effective slice thickness, because a particle can deviate farther from the imaging plane and still be detected.

In terms of particle type, the more echogenic the particle, whether due to size, shape, or acoustic impedance, the larger the effective slice thickness and thus the larger the image volume. This is because a more echogenic particle can be farther away from the image plane and still produce a high enough echo such that it can be detected in the resulting B-mode image.

Therefore, the effective slice thickness and the image volume are larger. A less echogenic particle must be closer to the image plane for its echo to be detected in the image, which means that the effective slice thickness is smaller.

Considering the suspension medium, a less attenuative medium results in a larger image volume, while a more attenuative medium results in a smaller volume. This is because attenuation of the medium results in decreased incident and reflected acoustic energy, and thus a particle has to be closer to the image plane for it to be detected in the resulting image. Following the same logic, any additional attenuative layers in the path of the ultrasound wave result in reducing the image volume.

When it comes to *in vivo* clinical applications, this dependency of image volume on numerous factors become a more critical issue. Because there are many parameters that can vary between one measurement and another, it becomes difficult, if not impossible, to replicate the setup. Therefore, it would likely be impossible to achieve an accurate result by using a model or a calibration scheme alone.

For example, imaging of bodily fluids such as CSF needs to be performed through skin and fat layers. The effective slice thickness is affected by the attenuation due to these layers; the higher the attenuation, the smaller the effective slice thickness. At the extreme where the attenuation is too high, the effective slice thickness becomes zero and detection becomes impossible. It is not realistic to measure and model all the components that can contribute to the overall attenuation of the ultrasound signal because there are too many variables. For example, even the ultrasound gel applied for imaging can significantly affect the image volume. The

thickness of the ultrasound gel varies not only between different sonographers, but also during a given procedure because the gel gets spread out while imaging.

Our findings show that a constant image volume derived from the beam profile alone cannot be used. The proposed method works because it relies on the image that already encompasses the effect of the key parameters involved in the measurement. Therefore, the volume estimation is tailored to an individual measurement and can adapt to the specific set of parameters, both controllable, such as beam focus, and uncontrollable, such as skin and fluid attenuation, for that measurement.

Table 5-1. Calculated effective slice thickness and maximum measurable concentration for different measurements.

Experiment	Type	Effective slice thickness (μm)	Maximum measurable concentration (particles/μL)
1	10 μm PS + MS	62	200
2	10 μm PS + Vevo	163	50
3	15 μm PS + MS	128	60
4	10 μm Silica + MS	76	100
6	T cells + Vevo	139	25

Table 5-1 shows the effective slice thickness and the maximum measurable concentrations for different sample types and imaging systems used in our experiments. Comparing experiment 1 and 2, where the same set of samples of 10 μm PS microspheres are measured with MS and with the Vevo, respectively, the effective slice thickness for the Vevo measurement is almost three times larger than for the MS measurement. Since the samples are the same for both imaging systems, the difference in effective slice thickness is mostly due to the difference in the imaging system, which, as expected, is significantly different.

Comparing experiment 1 and 3, where 10 μm and 15 μm PS microspheres are measured with MS, respectively, the effective slice thickness for 15 μm PS is about twice larger than for 10 μm

PS. Since both samples are measured with the same transducer, the difference in the effective slice thickness is mostly due to the difference in the particle types. The 15 μm PS microspheres are more echogenic due to their larger size, which results in larger effective slice thickness.

5.2 Maximum Measurable Concentration

The dependency of image volume results in different maximum measurable concentration for different measurement setups. As shown in Table 5-1, the larger the effective slice thickness, the lower the maximum measurable concentration. As noted previously, this is because a larger effective slice thickness results in more echoes being visible in the image for the same concentration, which leads to the particle detection algorithm failing to distinguish separate particles, starting at a lower concentration.

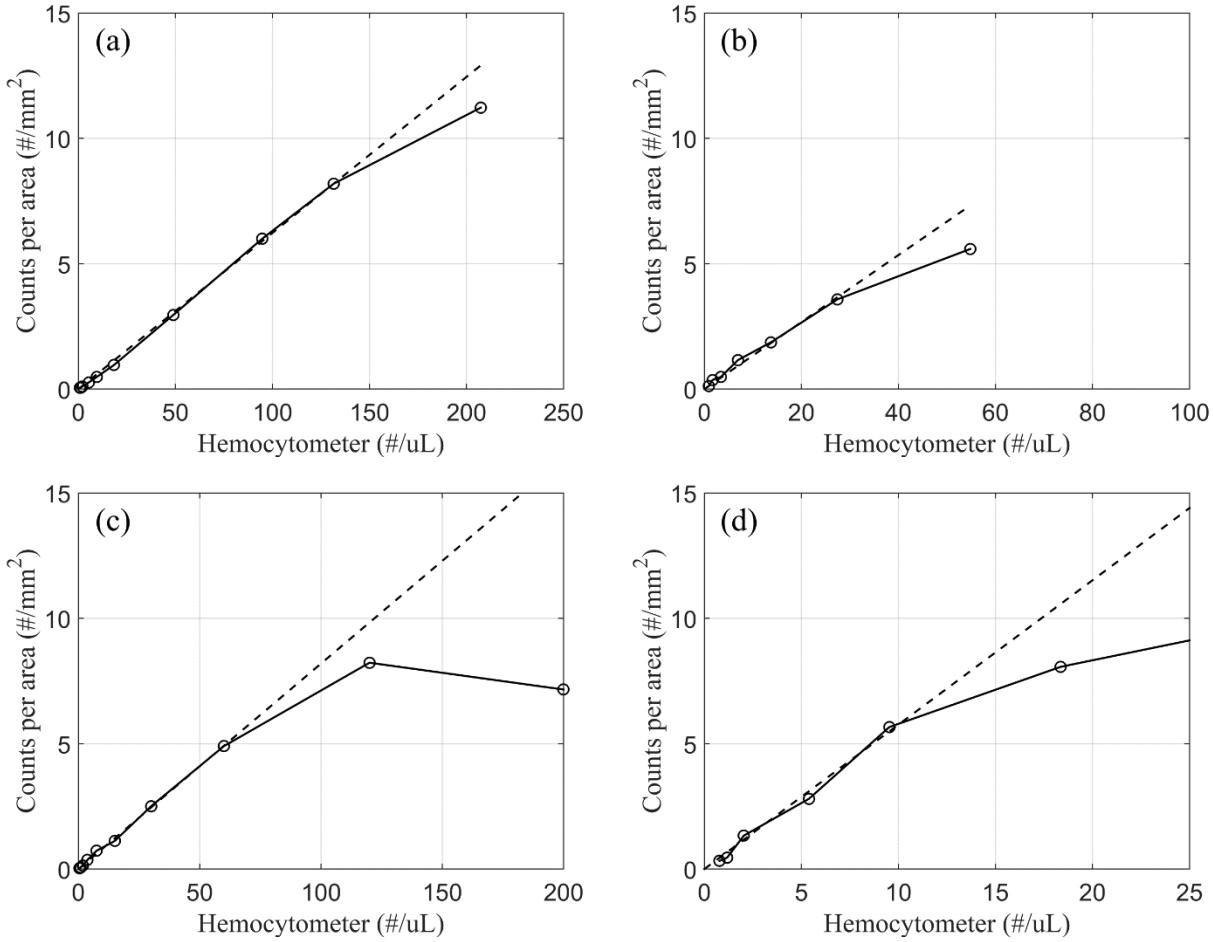

Figure 5-1. Plot of counts per area (counts/mm^2) vs. sample concentration for different measurements showing the points where the particle detection starts to fail. (a) 10 μm PS microspheres measured with MS. (b) 15 μm PS microsphere measured with MS. (c) 10 μm silica microsphere measured with MS. (d) 10 μm PS microsphere measured with the Vevo.

Since the maximum measurable concentration is limited by particle detection, it is insightful to look at the number of detected echoes in the image in addition to the absolute concentration of the sample. While a wide range of concentration is observed as shown in Table 5-1, ranging from 25 particles/μL for T cells imaged with the Vevo to 200 particles/μL for 10 μm PS microspheres imaged with MS, the range of corresponding counts per area of the image is much smaller. Figure 5-1 shows the plot of counts per mm^2 of the image area vs. sample concentration for different measurements. The straight line in the plot is a linear fit using only the low

concentration samples while enforcing a (0, 0) condition, and represents the ideal counts/mm^2 if the detection works perfectly. This is because the detection is accurate when the concentration is low. As seen in the figure, across different particle types and imaging systems, the detection starts to fail at around 5 counts/mm^2. Although this value varies somewhat due to the fact that the size and shape of the echo are not exactly the same, the extent of the variation in counts/mm^2 is much smaller than the variation in the maximum measurable concentration. The fact that the method starts to fail at such similar values of counts/mm^2 confirms that the large range of maximum measurable concentration is due to the failure in particle detection.

Before moving forward, it is important to address the seeming discrepancy between Table 5-1 and Figure 5-1. The maximum measurable concentration, according to Table 5-1, is higher than the concentration at which the detection starts to fail in Figure 5-1. For example, the maximum measurable concentration for the 10 μm PS microsphere sample imaged with MS is 200 particles/μL according to Table 5-1, but Figure 5-1 shows that the detection starts to fail around 130 particles/μL, which is significantly lower. While this appears to be a discrepancy, it is not: the particle detection does start to fail at a lower concentration, in the sense that it starts to undercount. The particles that are detected are those with higher amplitude, which increases the minimum observed echo amplitude in (6). A higher minimum echo amplitude results in smaller effective slice thickness. Since the echoes are undercounted but the effective slice thickness also decreases, the concentration can still be estimated correctly. This compensatory behavior eventually ceases when the particle detection completely fails.

The observation of the relationship between the effective slice thickness and the maximum measurable concentration in Table 5-1 and the counts/mm^2 in Figure 5-1 provides an important

insight into two issues: first, how to estimate the maximum measurable concentration for a given measurement and second, how to increase the maximum measurable concentration.

For a given measurement, it is important to know what the maximum measurable concentration is. Figure 5-2 shows the plot of maximum measurable concentration vs. effective slice thickness for experiments 1 through 4 and 6. An exponential fit with R^2 of 0.857 is achieved. The maximum measurable concentration decreases exponentially as the effective slice thickness increases. This is because, under the Gaussian assumption, the pulse-echo beam intensity drops off exponentially as the slice thickness increases. Therefore, when the effective slice thickness is small, increasing it leads to detecting many more echoes in the image, which, in turn, leads to a significant decrease in the maximum measurable concentration. When the effective slice thickness is large, increasing it leads to diminishing increase in the number of echoes since the beam intensity is already low, which, in turn, leads to a less significant decrease in the maximum measurable concentration.

It is important to remember that the data in Figure 5-2 is not from a single measurement, but multiple ones with different imaging systems and sample types. There are many parameters that vary across the five experiments including the imaging frequency, transducer types, nature of the particles, size of the particles, etc. Therefore, the exponentially decaying behavior observed in the figure is largely independent of the measurement parameters.

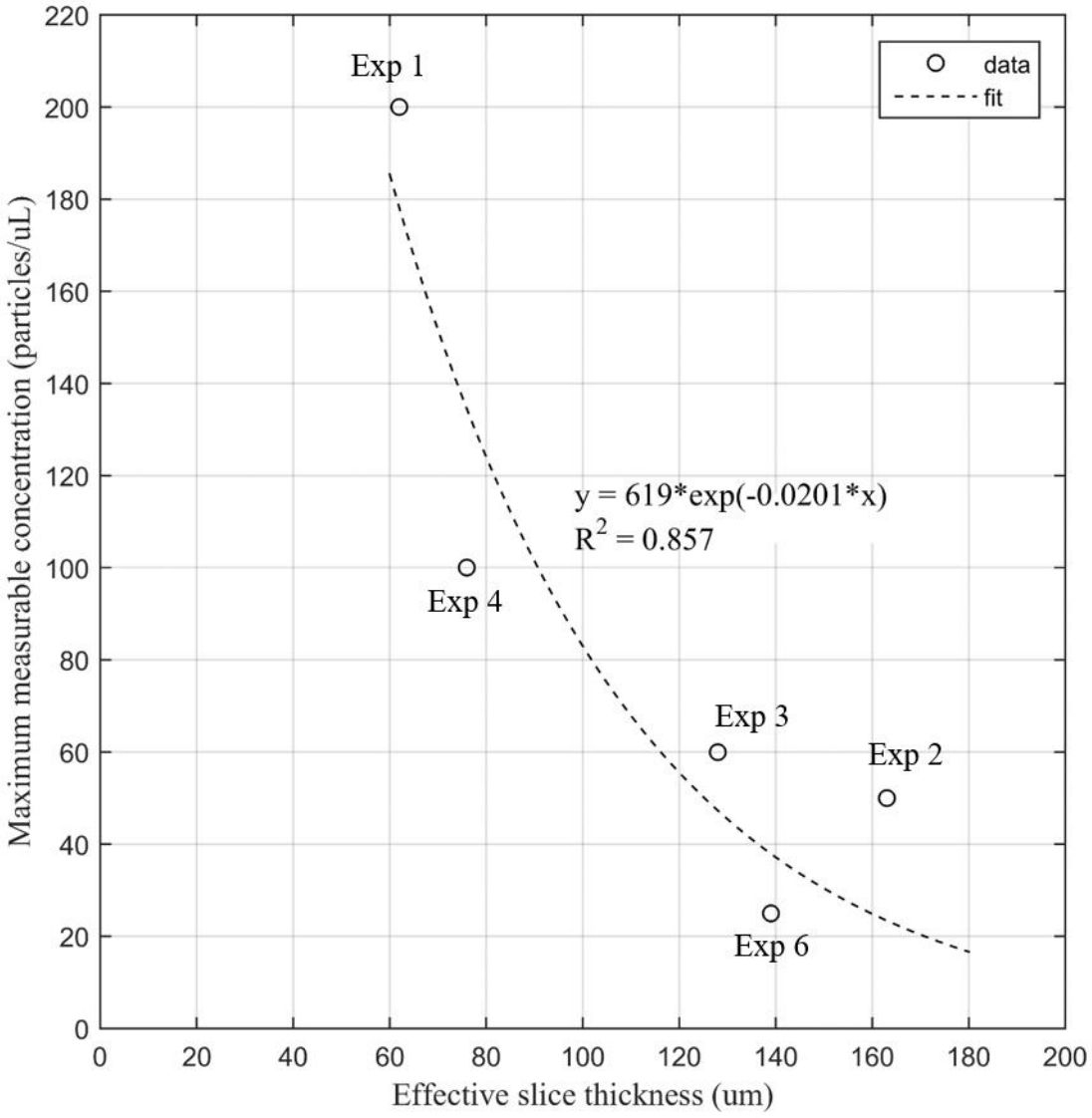

Figure 5-2. Plot of maximum measurable concentration vs. effective slice thickness for experiments 1 through 4 and 6 and the exponential fit to the data. R^2 of the fit is 0.857. The maximum measurable concentration decreases exponentially as the effective slice thickness increases.

Given the previous discussion, the second issue of increasing the maximum measurable concentration can be addressed. First, the curve shown in Figure 5-2 needs to be changed by improving the particle detection algorithm. A better detection algorithm will shift the curve up, which means that for a given effective slice thickness, the maximum measurable concentration is larger. A poorer detection algorithm will shift the curve down producing an opposite result.

Therefore, the best detection algorithm available should be used in order to shift the curve up as much as possible. However, this approach is limited because if the concentration is so high such that the echoes turn into a complete speckle pattern, individual particle detection will become impossible.

Once the best possible detection algorithm is chosen, measurements should be performed with the smallest effective slice thickness or at the left-most side of the curve. This means that, to measure the highest concentration possible, the settings of the imaging system should be such that the effective slice thickness is minimized. This will achieve the highest maximum measurable concentration. To enable this, a systematic way to adjust the effective slice thickness needs to be developed and this remains as an important area for future work.

5.3 Tradeoff between Accuracy and Number of Detections

Given that the particle detection is working correctly, the accuracy of the proposed method depends on accurate estimation of the effective slice thickness, which is derived from the characterization of the detected echoes. The detected echoes can be thought to be sampling the amplitude vs. axial position space and the lateral sigma vs. axial position space. The more detections the algorithm sees, the more confident the estimation of the spaces will be. Therefore, there is a trade-off between the measurement accuracy and the number of particle detections. Since increasing the number of detections increases the measurement time, the trade-off extends to the measurement time.

It is instructive to look at the dependence of accuracy on the number of detections. Figure 5-3 shows the measurement error and the coefficient of variation as a function of the number of detections for 10 μm PS microsphere samples measured with MS (experiment 1). The relative

measurement error ε_i for a measured concentration $C_{N=i}$ using $N = i$ echoes is defined by (14), where the result for $C_{N=10000}$ with 10,000 detected echoes is taken as the reference value.

$$\varepsilon_i = \left| \frac{C_{N=i} - C_{N=10000}}{C_{N=10000}} \right| \tag{14}$$

As seen in Figure 5-3, the measurement error as well as the uncertainty decrease as the number of detections increases. The mean deviation is below 5% and the coefficient of variation is below 15% when the number of detections is 500.

Due to the dependence of measurement accuracy on the number of detections, for a given measurement, the number of detections should be decided based on the target measurement accuracy. This means that a lower concentration sample will require a longer measurement time compared to a higher concentration one given that everything else is the same. This trade-off can be improved if the effective slice thickness can be modified as discussed previously. For samples with lower concentration, increasing the effective slice thickness by appropriately setting the parameters of the imaging system will allow increasing the number of detections per image, thereby decreasing the measurement time. Having the capability to adjust the effective slice thickness would provide an important flexibility to decrease the measurement time for low concentration samples and increase the maximum measurable concentration for high concentration samples.

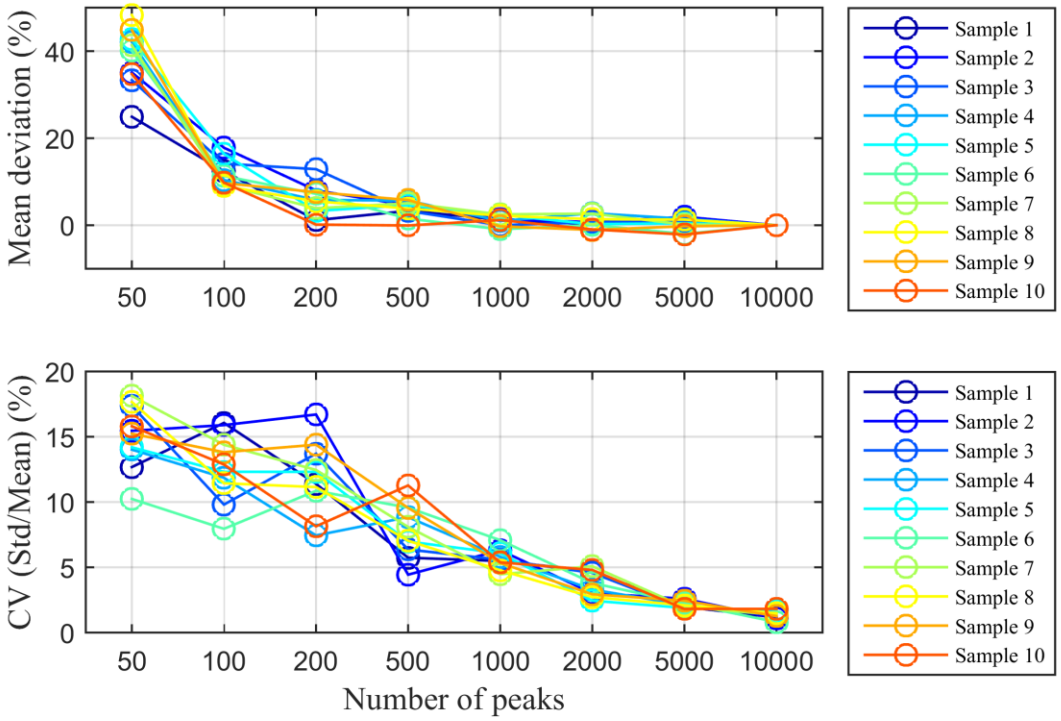

Figure 5-3. Mean deviation and coefficient of variation for 10 µm PS microsphere samples for varying numbers of detections used in particle concentration calculation. Mean deviation is calculated in reference to the measurement that uses 10,000 detections.

6. Contributions and Future Work

In this chapter, the contributions of this work is first summarized in Section 6.1 followed by the discussion of potential future work in Sections 6.2 – 6.9. In Section 6.2, potential ways to improve particle detection algorithm are discussed. In Section 6.3, the idea of using the transducer model as an a priori estimate in order to reduce the measurement time and improve the accuracy is discussed. Sections 6.4 discusses the limitation of the proposed method to spherical particles and suggests an approach to working with non-spherical particles. Section 6.5 discusses the challenges of analyzing cells and the aspects of the methods that can be improved to analyze cells more robustly. Along the line of cell analysis, Section 6.6 discusses the idea of creating a library of BSCs that can be used for classification of different types of cells as well as other particles. In Sections 6.7, 6.8, and 6.9, key potential applications of the proposed method are discussed. In Section 6.7, a pilot clinical study for investigating the application of the method to neonatal meningitis is discussed. In Section 6.8, an *in vitro* application as a potentially lower cost and lower complexity cytometry instrument is discussed. Finally, in Section 6.9, the idea of using a previously characterized sample to model a transducer is discussed.

6.1 Contributions

In this work, we have proposed a method for measuring the concentration of particle suspensions using high frequency B-mode ultrasound images of the sample. The method is based on individual detection of the particles from the image and characterization of their scatterer spreading to estimate the effective slice thickness. By using a completely image-based approach, the method does not require prior knowledge of the sample. Individual particle detection also enables the measurement of BSC for the individual echoes, which is used to classify the particle types and quantify the type-specific concentrations. The method has been demonstrated using

monodispersed and polydispersed samples of microspheres imaged with both mechanically scanned single element imaging system and VisualSonics Vevo 2100. Results from human T cell measurements have also been presented to demonstrate the capability of the method to work with non-ideal biological samples. The proposed method has a wide range of exciting potential applications, including a clinical one for infants where cell concentrations in bodily fluids such as CSF can be measured noninvasively using high frequency B-mode transfontanel imaging.

6.2 Particle Detection Algorithm

In this work, a simple spatial filter-based particle detection algorithm is used. While particle detection is an active area of research and there are many sophisticated algorithms available, it is not the main focus of this work. For this reason, a simple and straightforward algorithm has been chosen that allows us to focus on the main topic of this work, which is the estimation of the effective slice thickness of B-mode ultrasound images.

However, there are many potential improvements that can be made in regards to particle detection in the context of this work. First, while there are various particle detection algorithms that are applicable to optical microscopy, there is limited work specifically targeting particle detection in ultrasound images. Due to the substantially different imaging issues between ultrasound and optical microscopy, the nature of the resulting shape of the particle is significantly different when the image is acquired with ultrasound. Therefore, a particle detection algorithm that is specifically designed with an understanding of ultrasound imaging could drastically improve the accuracy and robustness.

Another way to improve particle detection is to employ particle tracking using adjacent frames. Particle tracking or cell tracking is not a new idea, and has been used widely in other

fields such as computational biology. It can be similarly applied to ultrasound images by taking advantage of the motion of the particles, which can be created by an inherent flow in the sample or by the acoustic streaming and acoustic radiation force produced by the ultrasound beam. By tracking the echoes in the image, it may be possible to reduce the number of erroneous detections and achieve more accurate detection even at low SNR.

6.3 Transducer Model Based Estimation

As discussed in Section 5.3, the measurement accuracy depends on having a high enough number of detections to accurately characterize the range of echo amplitude vs. axial position and lateral sigma vs. axial position. Since lateral spreading varies only by a small amount at a given axial position, the measurement accuracy mainly depends on accurately characterizing the amplitude vs. axial position space.

In the current implementation of the proposed method, the characterization of the echo amplitude space is done entirely based on the detected echoes. Except for the parameter R_e used to relate the elevational SSF to the lateral SSF, knowledge about the beam profile is not utilized. One way to improve the trade-off between the measurement accuracy and measurement time might be to use a beam profile model, whether analytical or from simulation, as a starting point in characterizing the echo amplitude space. Using the model as an a priori estimate, each of the detected echoes can be used to update the model. This way, with fewer detections a comparable or even a better result may be achieved. This approach would be especially advantageous for low concentration samples since it takes a longer measurement time to acquire the desired number of detections. Such speed enhancements would be especially useful in *in vivo* applications where measurement time is a key criteria.

6.4 Non-spherical Particles

One of the important requirements for the proposed method is that the particle can be modeled as a sphere. In the case where this is not true, as it is for many types of cells, the current implementation of the method may fail because the echo from a particle depends on its angular position. This leads to larger variation in the observed echo amplitude as well as scatterer spreading. However, due to the randomness in the angular position of the particles, there will be an inherent averaging process that takes place during measurement, which could allow modeling the particle as a sphere with an effective diameter and effective acoustic properties. This could be an important extension to the proposed method, especially in the context of cell analysis because of the non-ideal shape of the cells as well as the large inherent variability in their shape and size.

6.5 Variability in Cell Size and Shape

We showed that the proposed method is able to measure non-ideal particle samples such as human T cell suspensions, where the particle shapes and sizes are not as tightly controlled as in the case of microspheres. While the method is able to accurately estimate the concentration of the T cell samples, there are expected challenges in characterizing the echoes from biological samples due to the inherent variability in their shape and size, even when the sample consists of a single cell type. Variability in the echoes due to the variation in the shape and size of the cells could result in errors in volume estimation and type classification, which, in turn, could lead to errors in concentration measurement. Potential extensions to this work include analyzing a wider range of cell lines, and developing more robust methodologies for echo characterization that take into account the inherent variability within a cell type to improve accuracy of volume estimation and classification.

6.6 Library of BSCs

Clustering of particles based on the BSC is a powerful technique because it enable particle type differential and type-specific concentration measurement. However, in order to enable classification beyond simply clustering and attempt to identify a specific particle or cell type, a library of pre-measured BSCs of different particles is needed. Having a library of BSCs would enable employing machine learning techniques to predict the type of particles in the sample based on the labeled BSCs. A library of BSCs of non-biological particles such as polystyrene, polyethylene, and silica microspheres will be useful in industrial applications as well as in the life science applications. A library of BSCs of different cell types could enable identifying the cell types in *in vitro* as well as *in vivo* applications. This creation of such a library would ideally be an inter-laboratory effort where different research laboratories could measure BSCs of different particle types and add to a central database that can be used by the community of researchers. There has been significant effort in inter-laboratory validation of BSC measurements [19], [53], which have shown good agreement between different transducers, operators, and experimental setup. Extensions of such effort toward BSC library creation would be useful.

6.7 Application: Clinical Study for Neonatal Meningitis

As discussed in Chapter 0, a key potential application for the proposed method is in screening and monitoring neonatal meningitis. The current clinical protocol requires acquiring CSF through an LP, which is analyzed for WBC concentration, glucose and protein level, and culture. Infants younger than one year old have an openings in their skull called the fontanel. In this region, CSF is directly below a relatively thin skin layer, providing an acoustic window that can be used for ultrasound imaging. Applying the proposed method to the high frequency

ultrasound images acquired through the anterior fontanel has the potential to provide absolute WBC concentration without having to perform an LP.

While this work has shown that the proposed method can measure absolute concentration of biological particles such as human cells *in vitro*, application of the method to the *in vivo* setting has a number of potential challenges that must be carefully examined and resolved. First and foremost, the most critical issue is the attenuation from the skin layer. The backscattered energy from the cells that is already low is further reduced by the skin. As discussed previously, this has the effect of reducing the effective volume of the image and if the attenuation is too high, detection becomes impossible. The high frequency required to image the micrometer-scale sized cells make the attenuation even more severe because attenuation is typically exponentially related to the frequency. For this reason, the feasibility of applying the proposed method to *in vivo* application relies on characterizing the attenuation of the skin layer and choosing the appropriate frequency.

A pilot clinical study was planned to be carried out at Massachusetts General Hospital (MGH), Boston, MA in 2015. The study was planning to recruit ten pediatric patients who were to undergo an LP for suspected CSF cellularity (not limited to BM) and ten control patients. The study was to be performed with a Vevo with MS250S, a linear array probe with 21 MHz center frequency. The goal of the study was to determine if WBC in CSF can be detected when imaged through the anterior fontanel and if so, estimate the absolute concentration and compare it to the cell count from the LP. The study would have provided some initial knowledge about the attenuation of the skin over the anterior fontanel region and assess the possibility of *in vivo* absolute cell concentration measurement.

Unfortunately, the study did not happen due to concerns raised by the Internal Review Board (IRB) at MGH over the potential risk of applying high frequency ultrasound on developing neonatal brain. Despite the Vevo being the only commercially available array-based high frequency imaging system and its being used widely in research labs as well as for clinical studies, it has not yet been approved by the United States Food and Drug Administration (FDA). VisualSonics is currently in the process of getting FDA approval for their new model, the Vevo MD [54]. For the work on neonatal meningitis to continue, it is critical that a preliminary clinical study be done as soon as possible to characterize the attenuation through the anterior fontanel.

6.8 Application: *In vitro* Cell Analysis

There are a number of interesting *in vitro* applications of the proposed method in the context of cell analysis. Due to the nondestructive and noncontact nature of ultrasound imaging, it is especially attractive for *in vitro* analysis of cells where the sample can be analyzed without being taken out of the collection vial. Since the sample does not have to be discarded after the analysis, it allows a much larger volume of the sample to be analyzed, thus increasing the accuracy of the analysis. A potential analysis that fits the proposed method well is measuring the absolute or relative concentration of different cell types in suspension, which is analogous to experiment 5 in this work. This is a procedure that can be performed by using a flow cytometer where a fluorescent beads are used to tag different types of cells. The optical scattering produced by the fluorescent beads under a laser is used for differentiating. Although flow cytometers work well, they are typically bulky and expensive, making it difficult to be widely available.

The proposed method has the potential to perform the same procedure at reduced cost and complexity. The particle type differential based on BSC has already been demonstrated in this work in experiment 5 using microspheres of different sizes. However, whether this technique can

work with different cell types is not yet certain. Different cell types may not have enough difference in their size, shape, or acoustic properties to produce differences in their BSCs that can be detected. A similar technique as in flow cytometry may be adopted where cells are tagged with beads in order to produce BSCs that can be differentiated from cells that are untagged. While the range of functionality of such a device will certainly be less than a flow cytometer, it can be much lower in cost and more compact, even making a table-top device a possibility. Figure 6-1 shows a conceptual diagram of an ultrasound-based cytometry instrument.

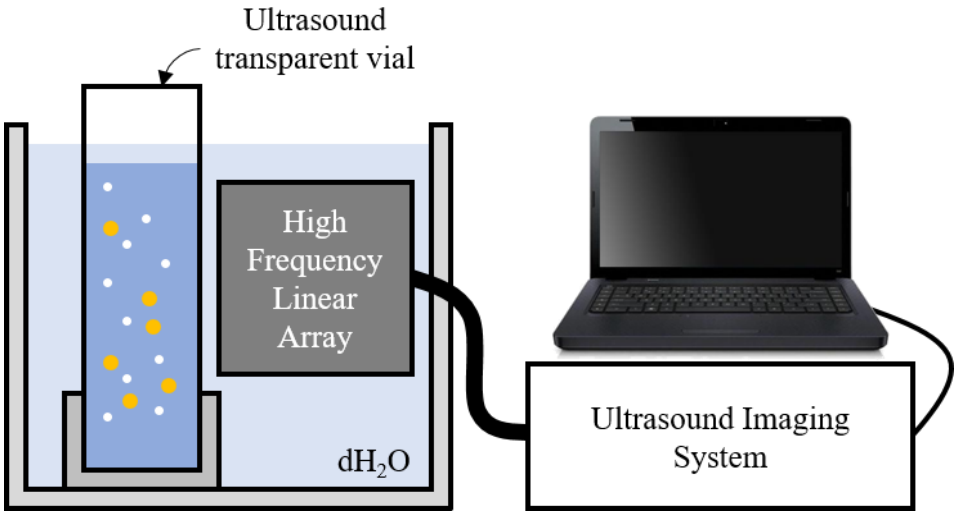

Figure 6-1. Ultrasound-based cytometry. The fluid sample under analysis is contained in an ultrasound transparent vial. The sample vial is inserted into a water bath. A high frequency ultrasound transducer images the sample through the water. The images are processed to perform type differential and type-specific concentration measurement.

6.9 Application: Transducer Characterization

As shown in this work, the characteristics of the detected echoes are determined by the characteristics of both the imaging system and the sample. This work utilize this dependency in order to characterize the sample. An interesting idea that stems from this is to use this dependency, in an inverse fashion, to characterize the transducer instead of the sample.

The idea is to characterize a transducer using a monodispersed sample that has been well-characterized, such that its particle concentration, the acoustic properties of the particles as well as the suspension media are all known. It is likely that it will be difficult to do a complete characterization of the transducer with this approach since there are limited parameters that can be extracted from the echoes. However, starting from a well-informed model it could be possible to fit the model using this approach.

A possible characterization process is depicted in Figure 6-2. The transducer being characterized is placed in a scanning system. A characterization fluid sample consisting of monodispersed particles of known size and concentration is chosen based on the expected frequency of the transducer. Images are acquired by linearly scanning the transducer, and echoes are detected and analyzed as described in this work to produce similar plots as in Figure 2-5. The detection results are used to fit the parameters of transducer model.

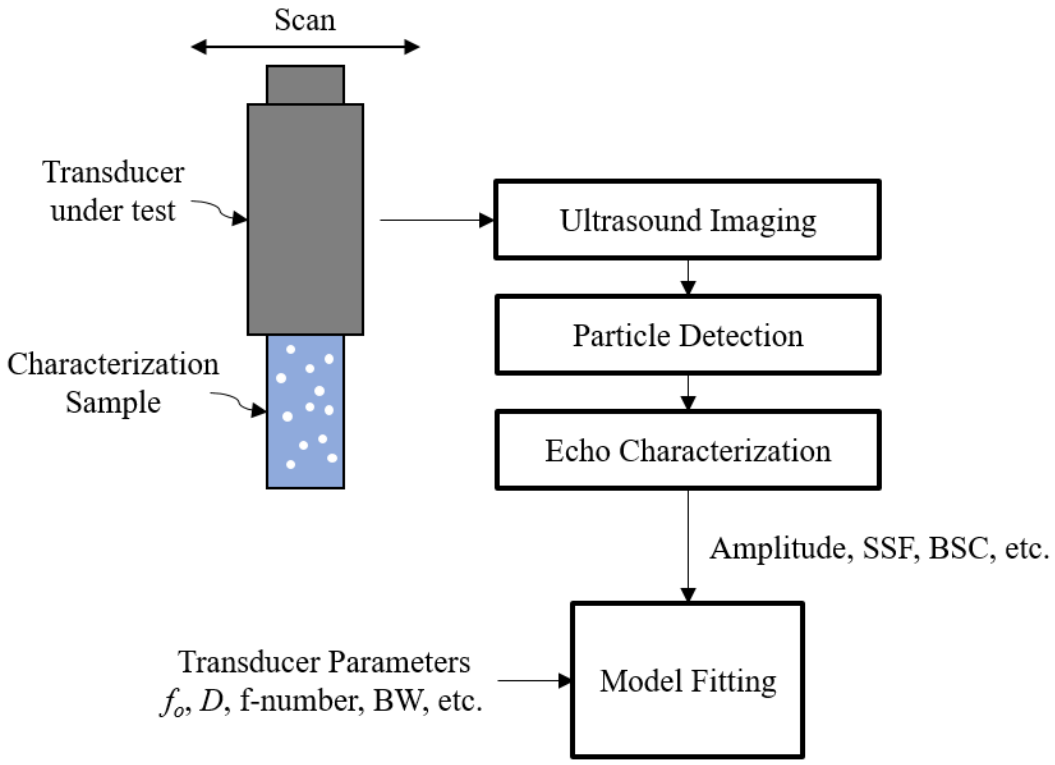

Figure 6-2. Transducer characterization method based on particle suspension measurement.

This idea is even more interesting for high frequency transducers because they are generally more difficult to characterize using a conventional method, since such characterization requires measurement instruments also working at higher frequency with higher spatial resolution.

Bibliography

[1] W. H. Coulter, “High speed automatic blood cell counter and cell size analyzer,” in *Proceedings of the National Electronics Conference*, vol. 12, pp. 1034–1040, 1956.

[2] M. D. Graham, “The Coulter Principle: Foundation of an Industry,” *J. Assoc. Lab. Autom.*, vol. 8, no. 6, pp. 72–81, Dec. 2003.

[3] W. J. Richar and E. S. Breakell, “Evaluation of an electronic particle counter for the counting of white blood cells,” *Am. J. Clin. Pathol.*, vol. 31, no. 5, pp. 384–393, May 1959.

[4] J. K. Nicholson, D. Stein, T. Mui, R. Mack, M. Hubbard, and T. Denny, “Evaluation of a method for counting absolute numbers of cells with a flow cytometer,” *Clin. Diagn. Lab. Immunol.*, vol. 4, no. 3, pp. 309–313, May 1997.

[5] M. W. Aune, J. L. Becker, C. Brugnara, W. Canfield, D. M. Dorfman, W. Fiehn, G. Fischer, P. Fitzpatrick, T. H. Flaming, H.-K. Henriksen, J. E. Kunicka, K. J. Lackner, E. Minchello, P. A. Mullenix, M. Myers, A. Petersen, W. Ternstrom, and S. J. Wilson, “Automated flow cytometric analysis of blood cells in cerebrospinal fluid: analytic performance,” *Am. J. Clin. Pathol.*, vol. 121, no. 5, pp. 690–700, May 2004.

[6] D. Bremell, N. Mattsson, F. Wallin, J. Henriksson, M. Wall, K. Blennow, H. Zetterberg, and L. Hagberg, “Automated cerebrospinal fluid cell count — New reference ranges and evaluation of its clinical use in central nervous system infections,” *Clin. Biochem.*, vol. 47, no. 1–2, pp. 25–30, Jan. 2014.

[7] L. Glasser, C. A. Murphy, and J. T. Machan, “The clinical reliability of automated cerebrospinal fluid cell counts on the Beckman-Coulter LH750 and Iris iQ200,” *Am. J. Clin. Pathol.*, vol. 131, no. 1, pp. 58–63, Jan. 2009.

[8] M. T. de Graaf, A. H. C. de Jongste, J. Kraan, J. G. Boonstra, P. A. E. Sillevis Smitt, and J. W. Gratama, “Flow cytometric characterization of cerebrospinal fluid cells,” *Cytometry B Clin. Cytom.*, vol. 80, no. 5, pp. 271–281, Sep. 2011.

[9] R. E. Apfel and C. K. Holland, “Gauging the likelihood of cavitation from short-pulse, low-duty cycle diagnostic ultrasound,” *Ultrasound Med. Biol.*, vol. 17, no. 2, pp. 179–185, Jan. 1991.

[10] A. Haake, A. Neild, D.-H. Kim, J.-E. Ihm, Y. Sun, J. Dual, and B.-K. Ju, “Manipulation of cells using an ultrasonic pressure field,” *Ultrasound Med. Biol.*, vol. 31, no. 6, pp. 857–864, Jun. 2005.

[11] T. L. Szabo, *Diagnostic Ultrasound Imaging: Inside Out*, 1st Edition. Academic Press, 2004.

[12] F. L. Lizzi, M. Greenebaum, E. J. Feleppa, M. Elbaum, and D. J. Coleman, “Theoretical framework for spectrum analysis in ultrasonic tissue characterization,” *J. Acoust. Soc. Am.*, vol. 73, no. 4, pp. 1366–1373, Apr. 1983.

[13] F. L. Lizzi, M. Ostromogilsky, E. J. Feleppa, M. C. Rorke, and M. M. Yaremko, “Relationship of Ultrasonic Spectral Parameters to Features of Tissue Microstructure,” *IEEE Trans. Ultrason. Ferroelectr. Freq. Control*, vol. 34, no. 3, pp. 319–329, May 1987.

[14] M. F. Insana, R. F. Wagner, D. G. Brown, and T. J. Hall, "Describing small-scale structure in random media using pulse-echo ultrasound," *J. Acoust. Soc. Am.*, vol. 87, no. 1, pp. 179–192, Jan. 1990.

[15] J. J. J. Faran, "Sound Scattering by Solid Cylinders and Spheres," *J. Acoust. Soc. Am.*, vol. 23, no. 4, pp. 405–418, Jul. 1951.

[16] R. E. Baddour, M. D. Sherar, G. J. Czarnota, J. W. Hunt, L. Taggart, A. Giles, N. R. Farnoud, and M. C. Kolios, "High frequency ultrasound imaging of changes in cell structure including apoptosis," in *2002 IEEE Ultrasonics Symposium, 2002. Proceedings*, vol. 2, pp. 1639–1644, 2002.

[17] F. T. H. Yu and G. Cloutier, "Experimental ultrasound characterization of red blood cell aggregation using the structure factor size estimator," *J. Acoust. Soc. Am.*, vol. 122, no. 1, pp. 645–656, Jul. 2007.

[18] E. Franceschini, B. Metzger, and G. Cloutier, "Forward problem study of an effective medium model for ultrasound blood characterization," *IEEE Trans. Ultrason. Ferroelectr. Freq. Control*, vol. 58, no. 12, pp. 2668–2679, Dec. 2011.

[19] J. J. Anderson, M.-T. Herd, M. R. King, A. Haak, Z. T. Hafez, J. Song, M. L. Oelze, E. L. Madsen, J. A. Zagzebski, W. D. O'Brien, and T. J. Hall, "Interlaboratory Comparison of Backscatter Coefficient Estimates for Tissue-Mimicking Phantoms," *Ultrason. Imaging*, vol. 32, no. 1, pp. 48–64, Jan. 2010.

[20] A. S. Tunis, R. E. Baddour, G. J. Czarnota, A. Giles, A. E. Worthington, M. D. Sherar, and M. C. Kolios, "Using high frequency ultrasound envelope statistics to determine scatterer number density in dilute cell solutions," in *2005 IEEE Ultrasonics Symposium*, vol. 2, pp. 878–881, 2005.

[21] S. M. Leithem, R. J. Lavarello, W. D. O. Jr, and M. L. Oelze, "Estimating concentration of ultrasound contrast agents with backscatter coefficients: Experimental and theoretical aspects," *J. Acoust. Soc. Am.*, vol. 131, no. 3, pp. 2295–2305, Mar. 2012.

[22] K. Levenberg, "A method for the solution of certain non-linear problems in least squares," *Q. Appl. Math.*, vol. 2, pp. 164–168, Jan. 1944.

[23] D. Marquardt, "An Algorithm for Least-Squares Estimation of Nonlinear Parameters," *SIAM J. Appl. Math.*, vol. 11, no. 2, pp. 431–441, 1963.

[24] K. P. Mercado, M. Helguera, D. C. Hocking, and D. Dalecki, "Estimating Cell Concentration in Three-Dimensional Engineered Tissues Using High Frequency Quantitative Ultrasound," *Ann. Biomed. Eng.*, vol. 42, no. 6, pp. 1292–1304, Mar. 2014.

[25] L. Elvira, P. Vera, F. J. Cañadas, S. K. Shukla, and F. Montero, "Concentration measurement of yeast suspensions using high frequency ultrasound backscattering," *Ultrasonics*, vol. 64, pp. 151–161, Jan. 2016.

[26] X. Jimenez, S. K. Shukla, I. Ortega, F. J. Illana, C. Castro-González, B. Marti-Fuster, I. Butterworth, M. Arroyo, B. Anthony, and L. Elvira, "Quantification of Very Low Concentrations of Leukocyte Suspensions In Vitro by High-Frequency Ultrasound," *Ultrasound Med. Biol.*, in press.

[27] M. C. Kolios, G. J. Czarnota, A. Worthington, A. Giles, A. S. Tunis, and M. D. Sherar, "Towards understanding the nature of high frequency backscatter from cells and tissues: an investigation of backscatter power spectra from different concentrations of cells of different sizes," in *2004 IEEE Ultrasonics Symposium*, vol. 1, pp. 606–609 Vol.1, 2004.

[28] R. E. Baddour, M. D. Sherar, J. W. Hunt, G. J. Czarnota, and M. C. Kolios, "High-frequency ultrasound scattering from microspheres and single cells," *J. Acoust. Soc. Am.*, vol. 117, no. 2, pp. 934–943, Feb. 2005.

[29] J. H. Lee, J. Jiménez, X. Zhang, D. S. Boning, and B. W. Anthony, "Ultrasound image-based absolute concentration measurement technique for materials with low scatterer concentration," in *International Ultrasonics Symposium* (IUS), 2015 © IEEE. doi: 10.1109/ULTSYM.2015.0208

[30] Y.-N. Chao, N.-C. Chiu, and F.-Y. Huang, "Clinical features and prognostic factors in childhood pneumococcal meningitis," *J. Microbiol. Immunol. Infect. Wei Mian Yu Gan Ran Za Zhi*, vol. 41, no. 1, pp. 48–53, Feb. 2008.

[31] K. L. Carstairs, D. A. Tanen, A. S. Johnson, S. B. Kailes, and R. H. Riffenburgh, "Pneumococcal bacteremia in febrile infants presenting to the emergency department before and after the introduction of the heptavalent pneumococcal vaccine," *Ann. Emerg. Med.*, vol. 49, no. 6, pp. 772–777, Jun. 2007.

[32] D. Grandgirard and S. L. Leib, "Meningitis in Neonates: Bench to Bedside," *Clin. Perinatol.*, vol. 37, no. 3, pp. 655–676, Sep. 2010.

[33] P. T. Heath and I. O. Okike, "Neonatal bacterial meningitis: an update," *Paediatr. Child Health*, vol. 20, no. 11, pp. 526–530, Nov. 2010.

[34] P. Ishimine, "Fever without source in children 0 to 36 months of age," *Pediatr. Clin. North Am.*, vol. 53, no. 2, pp. 167–194, Apr. 2006.

[35] X. Sáez-Llorens and G. H. McCracken Jr, "Bacterial meningitis in children," *The Lancet*, vol. 361, no. 9375, pp. 2139–2148, Jun. 2003.

[36] L. J. Baraff, "Management of infants and young children with fever without source," *Pediatr. Ann.*, vol. 37, no. 10, pp. 673–679, Oct. 2008.

[37] H.-L. Zhang and J. Wu, "Cerebrospinal fluid viscosity: can it be used as a novel diagnostic measure for acute meningitis?," *South. Med. J.*, vol. 104, no. 2, pp. 155–156; author reply 156, Feb. 2011.

[38] D. A. Seehusen, M. M. Reeves, and D. A. Fomin, "Cerebrospinal fluid analysis," *Am. Fam. Physician*, vol. 68, no. 6, pp. 1103–1108, Sep. 2003.

[39] H. P. Garges, M. A. Moody, C. M. Cotten, P. B. Smith, K. F. Tiffany, R. Lenfestey, J. S. Li, V. G. Fowler, and D. K. Benjamin, "Neonatal Meningitis: What Is the Correlation Among Cerebrospinal Fluid Cultures, Blood Cultures, and Cerebrospinal Fluid Parameters?," *Pediatrics*, vol. 117, no. 4, pp. 1094–1100, Apr. 2006.

[40] R. Hickling, "Analysis of Echoes from a Solid Elastic Sphere in Water," *J. Acoust. Soc. Am.*, vol. 34, no. 10, pp. 1582–1592, Oct. 1962.

[41] J. A. Jensen, “Field: A Program for Simulating Ultrasound Systems,” in *Medical & Biological Engineering & Computing*, vol. 34, pp. 351–353, 1996.

[42] J. A. Jensen and N. B. Svendsen, “Calculation of pressure fields from arbitrarily shaped, apodized, and excited ultrasound transducers,” *IEEE Trans. Ultrason. Ferroelectr. Freq. Control*, vol. 39, no. 2, pp. 262–267, Mar. 1992.

[43] “ShapeOko 2 - ShapeOko.” [Online]. Available: http://www.shapeoko.com/wiki/index.php/ShapeOko_2. [Accessed: 22-Apr-2016].

[44] “Production-Ready FPGA Integration Modules,” *Opal Kelly Incorporated*. [Online]. Available: https://www.opalkelly.com/products/xem3010/. [Accessed: 22-Apr-2016].

[45] “Vevo® 2100 System | Leading the way in ultra high frequency, high resolution ultrasound and photoacoustic imaging technologies.” [Online]. Available: http://www.visualsonics.com/products/vevo-2100. [Accessed: 21-Apr-2016].

[46] C. M. Moran, S. D. Pye, W. Ellis, A. Janeczko, K. D. Morris, A. S. McNeilly, and H. M. Fraser, “A Comparison of the Imaging Performance of High Resolution Ultrasound Scanners for Preclinical Imaging,” *Ultrasound Med. Biol.*, vol. 37, no. 3–2, pp. 493–501, Mar. 2011.

[47] “NIST traceable silica size standards nanospheres and microspheres.” [Online]. Available: http://www.microspheres-nanospheres.com/Microspheres/Size%20standards/Silica%20size%20standards.htm. [Accessed: 26-Apr-2016].

[48] H. Yamanishi, N. Imai, E. Suehisa, Y. Kanakura, and Y. Iwatani, “Determination of leukocyte counts in cerebrospinal fluid with a disposable plastic hemocytometer,” *J. Clin. Lab. Anal.*, vol. 21, no. 5, pp. 282–285, 2007.

[49] R. A. McPherson and M. R. Pincus, *Henry’s Clinical Diagnosis and Management by Laboratory Methods*, 22nd ed. Philadelphia, PA: Elsevier Saunders, 2011.

[50] M. Absher, “Hemocytometer counting,” in *Tissue Culture: Methods and Applications*, New York: Academic Press, pp. 395–397, 1973.

[51] R. Biggs and R. L. Macmillan, “The Error of the Red Cell Count,” *J. Clin. Pathol.*, vol. 1, no. 5, pp. 288–291, Nov. 1948.

[52] L. Nielson, G. Smyth, and P. Greenfield, “Hemacytometer Cell Count Distributions: Implications of Non-Poisson Behavior,” *Biotechnol. Prog.*, vol. 7, no. 6, pp. 560–563, Nov. 1991.

[53] E. L. Madsen, F. Dong, G. R. Frank, B. S. Garra, K. A. Wear, T. Wilson, J. A. Zagzebski, H. L. Miller, K. K. Shung, S. H. Wang, E. J. Feleppa, T. Liu, W. D. O’Brien, K. A. Topp, N. T. Sanghvi, A. V. Zaitsev, T. J. Hall, J. B. Fowlkes, O. D. Kripfgans, and J. G. Miller, “Interlaboratory comparison of ultrasonic backscatter, attenuation, and speed measurements,” *J. Ultrasound Med. Off. J. Am. Inst. Ultrasound Med.*, vol. 18, no. 9, pp. 615–631, Sep. 1999.

[54] “FUJIFILM Visualsonics – Vevo MD.” [Online]. Available: http://vevomd.com/. [Accessed: 21-Apr-2016].